Photo-Realistic Rendering of Fiber Assemblies

Dissertation

zur

Erlangung des Doktorgrades (Dr. rer. nat.)

der

Mathematisch-Naturwissenschaftlichen Fakultät

der Rheinischen Friedrich-Wilhelms-Universität Bonn

vorgelegt von

Dipl.-Inform. Arno Zinke

Bonn, 3. August 2007

Universität Bonn
Institut für Informatik II
Römerstraße 164, D-53117 Bonn

Angefertigt mit Genehmigung der Mathematisch-Naturwissenschaftlichen Fakultät der Rheinischen Friedrich-Wilhelms Universität Bonn

1. Referent: Prof. Dr. Andreas Weber
2. Referent: Prof. Dr. Reinhard Klein
3. Referent: Prof. Dr.-Ing. Marcus Magnor

Tag der Promotion: 9. Januar 2008

Diese Dissertation ist auf dem Hochschulschriftenserver der ULB Bonn http://hss.ulb.uni-bonn.de/diss_online elektronisch publiziert.

Erscheinungsjahr: 2008

ABSTRACT

In this thesis we introduce a novel uniform formalism for light scattering from filaments, the Bidirectional Fiber Scattering Distribution Function (BFSDF). Similar to the role of the Bidirectional Surface Scattering Reflectance Distribution Function (BSSRDF) for surfaces, the BFSDF can be seen as a general approach for describing light scattering from filaments. Based on this theoretical foundation, approximations for various levels of abstraction are derived allowing for efficient and accurate rendering of fiber assemblies, such as hair or fur. In this context novel rendering techniques accounting for all prominent effects of local and global illumination are presented. Moreover, physically-based analytical BFSDF models for human hair and other kinds of fibers are derived. Finally, using the model for human hair we make a first step towards image-based BFSDF reconstruction, where optical properties of a single strand are estimated from ”synthetic photographs” (renderings) a full hairstyle.

CONTENTS

1. INTRODUCTION

Modeling of fiber assemblies is essential to computer graphics for a variety of applications. A very prominent example is the modeling of hair and fur for virtual characters. In this context diverse problems have to be solved to create believable photo-realistic characters. This includes the generation of convincing hair-styles, the simulation of hair dynamics as well as hair rendering [62, 14, 55].

All these problems draw their complexity mainly from the huge number of interacting individual hair strands. Another issue is the long but comparatively thin structure of a strand combined with its highly nonlinear deformation under external load. This makes a modeling very sensitive to the choice of computation techniques and may cause sampling and stability artifacts. Finally, light scattering from hair fibers is highly anisotropic and inter-reflections play an important role for the right visual perception of the color. Hence, not only local but also global scattering effects have to be taken into account.

Besides of its application to virtual characters, accurate optical simulations of hair are gaining relevance also in the cosmetic industry. Here, the interest focuses mainly on the prediction of the hair color under different illuminations and for different hairstyles.

Another active area of research which is closely related to the modeling of fiber assemblies is the simulation of woven tissue and knitwear [6, 9]. However, in contrast to hair modeling the possible deformation of a tissue is highly restricted due to the constraints caused by the regular structure of the weaving pattern. Therefore the approaches used to model the dynamics of tissue and knitwear substantially differ from hair.

This thesis focuses on efficient and physically accurate visualization of large fiber assemblies, mainly in the context of hair rendering. Based on a novel framework for light scattering from a single fiber efficient rendering techniques for vari-

ous levels of abstraction are presented and other aspects of hair and fiber rendering are discussed.

1.1 Organization

In chapter 2, we will give a brief overview over optically relevant properties of fibers in general. In this context we will also discuss light scattering from human hair fibers including the influence of water. Chapter 3 describes a novel scattering formalism for light scattering from filaments. Based on this framework new rendering techniques are presented in chapter 4. Finally, an approach for image-based reconstruction of hair scattering functions is sketched in chapter 5. We close the thesis with a conclusion and proposals for future research activities.

2. OPTICAL PROPERTIES OF FIBERS

2.1 Filaments and Fibers

In the following the terms fiber and filament will be used interchangeably. They always stand for a class of materials that are either continuous thin structures or discrete elongated pieces, such as: hair or fur fibers, yarns, wires ropes or grass (Fig. 2.1). To analyze scattering from fibers their structure and the impact on scattering has to be analyzed. In this context it is often useful to decouple local from global properties. For example the way a fiber is bent or warped can be separated from the local geometry of its cross section.

A fiber may be a composite material like yarns and human hair or can consist of only one matter as in the case of optical fibers or metal wires. In principle it is possible to estimate scattering from a fiber from its geometric shape and the optical properties of its components. However, this requires a deep understanding of structural and optical interrelationships. In the next section only a brief overview over some of the relevant optical properties is given. For further reading on scattering in matter we refer to the book written by van de Hulst [60].

2.1.1 Optical Material Properties of Fibers

There is a variety of optical properties describing light scattering in matter. However, often only four wavelength dependant properties are needed to estimate the scattering distribution: the *scattering coefficient*, the *phase function*, the *index of refraction* (or refractive index) and the *absorption coefficient*.

The scattering coefficient is a factor that expresses the attenuation of radiant energy per unit length caused by scattering during its passage through a medium. Depending on the medium the scattering of light may be either isotropic

or anisotropic. In this context the phase function is a probability density function describing the angular distribution of volumetric light scattering.

For dielectric and conducting media the dimensionless index of refraction plays an important role. It is closely related to the phase velocity of light in matter and affects the scattering paths of light as well as the transmittance and the reflectance of a material (see also App. 7.1.2, App. 7.1.3). Note that reflection or refraction can in principle change the polarization of light. However, if not stated differently unpolarized light is assumed for all further considerations.

If light enters a dielectric it gets attenuated. The attenuation per unit length is given by another optical property, which is called the absorption coefficient.

By simulating light transport at a fiber, it is basically possible to render photorealistic images of fiber based geometries for arbitrary lighting.

Since a very relevant application of fiber rendering is hair rendering, the next section will explain phenomenological effects dominating the appearance of human hair. Moreover, a simple physically-based scattering model accounting for these effects is introduced.

Fig. 2.1: Examples of fiber based geometries and materials. **Top left:** red silk fabric (`http://www.echinatex.net/images/upload/product_200661111835.jpg`), **Top right:** cotton grass (`http://www.naturschutzstation.de/bilder/pflanzen/wollgrass_steff.jpg`), **Bottom left:** human hair, **Bottom right:** a cable drum (`http://www.optocore.com/pics/products/Optocable800.jpg`).

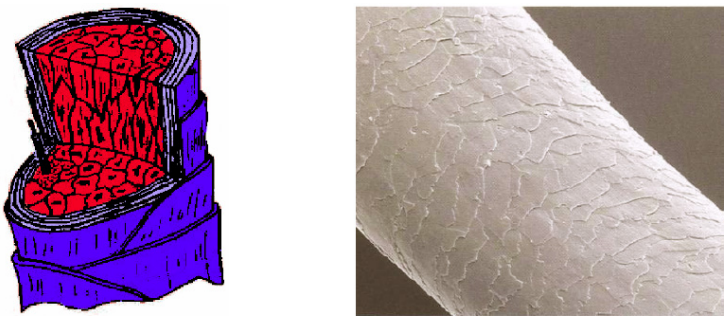

Fig. 2.2: Hair structure: **Left:** cortex (red) and cuticle (blue), **Right:** a hair under an electron microscope (`http://www.pg.com/science/haircare/hair_twh_11/image002.jpg`).

2.1.2 Human Head Hair

The average human head has about 100,000 hair strands. Each strand consists of layered keratin structures which can be roughly classified as either *cuticle* or *cortex* (see Fig. 2.2). The inner of the hair is called the cortex. It contains of a bunch of cell strings and determines most optical properties of a hair strand. Pigment granules that are distributed throughout the hair cortex and which are concentrated in its core (the *medulla*) give the hair its distinctive coloring. However, the overall hair color may exhibit extreme variations with respect to viewing direction, illumination and the entire hairstyle.

The hair cortex is covered by several layers composed of flat, overlapping cells. This scaly structure is called the cuticle. Due to the overlapped arrangement the surface of the scales exhibit a systematic deviation from the normal of a smooth fiber.

The overall thickness of a human hair is generally between $50 - 100\mu m$ in the European population, but it can average $120\mu m$ in some Asian populations. However, not only the width of a hair fiber may vary, but also the cross section geometry. Asian hair tends to have a nearly circular cross section, whereas African hair exhibits a substantial ellipticity [56]. For optical properties of human hair, such as absorption coefficients and refractive index, we refer to table 3.1 in section 3.10.2.

Fig. 2.3: Blond hair: **Left:** A photograph of blond hair. **Right:** A close-up of the photograph shown left. Note the refractions indicating that light scattering from a hair strand is quite similar to scattering from a dielectric cylinder.

According to Marschner et al. [37] the morphology of the hair provides an adequate explanation for all prominent features of scattering from a single hair strand. Substantial measurements indicated that human hair fibers can be approximated very well by transparent dielectric cylinders with a colored interior and a surface composed of rough, tilted scales. An example, which supports this assumption is shown in Fig. 2.3.

Marschner et al. showed that all relevant features observed during measurements can be explained by the first three orders of scattering from a smooth dielectric cylinder, which contain the biggest fraction of scattered power (see Fig. 2.4). These scattering components are denoted R-, TT- and TRT-component, respectively. The R-component is the direct surface reflection and since no absorption takes place light gets attenuated only by Fresnel reflection (App. 7.1.3). For the two other components light covers some distance inside the fiber, leading to two colored highlights, a strong forward scattering highlight (TT—two times transmitted) which is visible when hair is lit from behind and a backward scattering lobe (TRT—two times transmitted and internally reflected). Some photographs illustrating the appearance of these highlights are shown in Fig. 2.5.

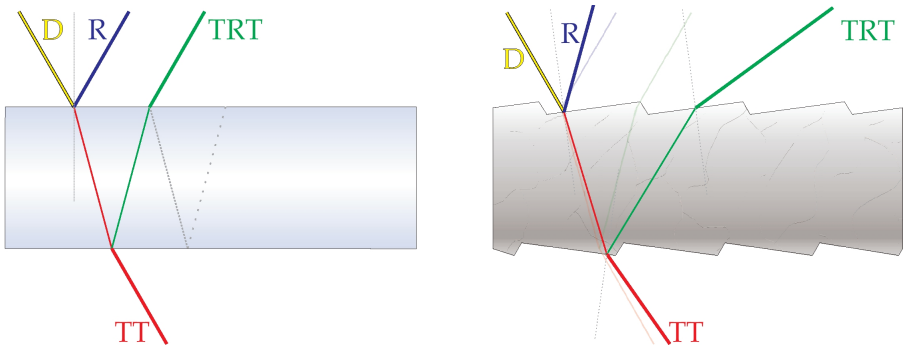

Fig. 2.4: Modeling light scattering from a hair strand based on a dielectric cylinder. **Left:** The first three scattering modes (R,TT,TRT) of a smooth dielectric cylinder. **Right:** Scattering from a hair fiber. Due to the tiled surface scales the highlights are shifted with respect to the perfect specular direction.

Another effect which can be explained by using the cylinder model are ”glints”. This phenomenon (commonly seen in people of European and African descent, less so in Asians) causes the hair to behave similar to a lens, focusing light in certain directions. As it is shown in Fig. 2.5 (rightmost image) they are an important part of the appearance, and they lend a distinctive texture to the hair.

Generally, human hair fibers can not be treated as perfect-smooth cylinders. Since the hair surface is tiled, the scattering differs from a smooth cylinder: The R mode is displaced towards the root, TT and TRT towards the tip. Moreover spatial and angular blurring occurs (scattering coefficients> 0) and the cross section may vary in shape. Also structural variations, such as local variation of the pigment density, influence scattering . However, in the following it is assumed that such effects can be handled by slight modifications of the original dielectric cylinder model. For a detailed description of this model as well as a more formal discussion of scattering from dielectric fibers in general, we refer to sections 3.6, 3.9.2 and 3.10.2.

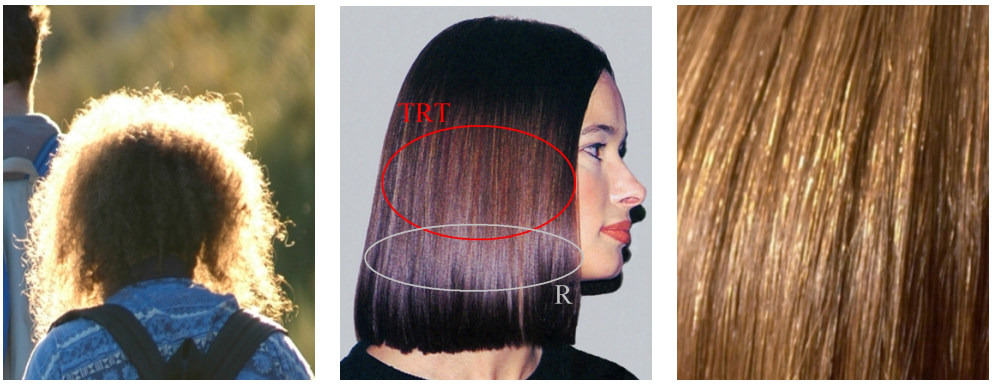

Fig. 2.5: Highlights. **Left:** Hair is lit from behind: colored TT-component. **Middle:** A single front light: white R-component, colored TRT-component. **Right:** Texture due to glints (from [37]).

2.1.3 Wet Hair

Fig. 2.6: Comparison of a brown hairstyle (images from [63]) before (left) and after treatment with water (right). Note the darkening of the overall hair color and the shinier appearance of the wet hair.

When hair is treated with water its appearance changes. Although several publications are addressing this phenomenon the proposed scattering models are purely phenomenological guesses without any further qualitative or quantitative analysis [63, 64, 14]. After discussing the effects occurring for wet hair we will show that they can be modeled by using a simple physically-based approach.
As illustrated in figure 2.6 and figure 2.7 the geometry changes (agglutination) and the hair looks more shinier and darker if hair is treated with water. The increase in reflectivity happens mainly because the dry surface exhibits substantial surface roughness, whereas a liquid layer around the hair leads to a nearly smooth surface. Generally, more roughness gives a wider specular lobe (R-component), thus less prominent intensity peaks. Moreover, the water layer causes additional highlights (denoted R',R'',...) due to inter reflections between the air-liquid and liquid-hair interfaces, further increasing the overall reflectivity (see Fig. 2.8 Left).

The darkening is a combination of several effects. First of all the agglutination of hair strands locally increases the hair density, strengthening the effective attenuation in the hair volume. Moreover— according to [63]— water is absorbed

Fig. 2.7: Close-ups of a blond hairstyle (fixed camera and light source) with increasing humidity penetration (from left to right). If the hair is wet agglutination and substantial darkening occurs.

into the hair fiber further increasing the opacity of a strand. However, also the water layer has a substantial impact on the appearance. It induces stronger internal reflections reducing the intensity of scattering components, since more energy gets absorbed inside the fiber. Because the absorption coefficient is usually a wave length dependant property this also changes the overall coloring of the internally scattered highlights. Moreover, stronger multiple internal scattering is spreading the energy over area and solid angle. Due to this effect, colored highlights get blurred and become less prominent.

The fiber based effects of darkening and increased shininess can be qualitatively simulated and validated using a rather simple physically based model: A dielectric cylinder with an index of refraction matching the effective index of hair (which is 1.55, c.f. [57]) surrounded by a thin water layer (index of refraction is 1.33). We implemented a particle tracer to estimate the spatial variation of the radiant flux at the surface of the fiber according to Fig. 2.8 Right. Some results illustrating the influence of the water layer are shown in Fig. 2.9 and Fig. 2.10. Note in particular the darkening of the TRT-lobe and the additional highlights. Varying the thickness of the water layer did not qualitatively change these effects.

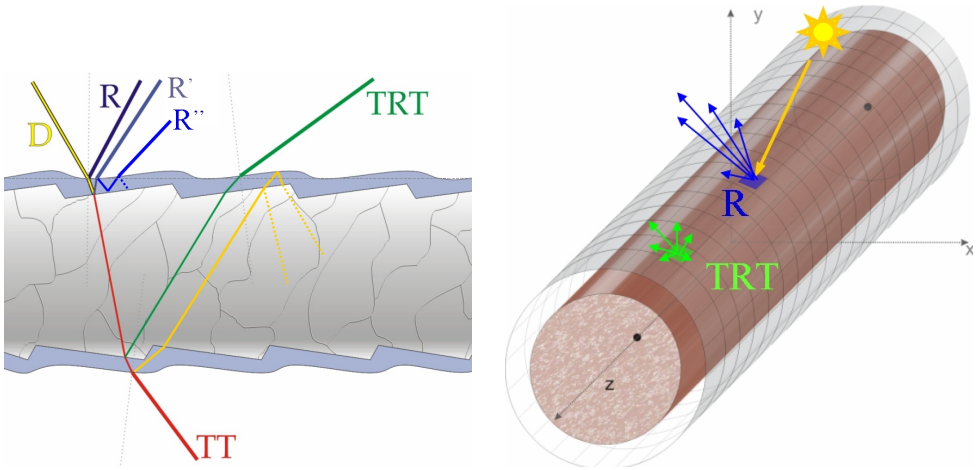

Fig. 2.8: **Left:** Illustration of a wet hair strand. The reflectivity increases due to multiple reflection highlights (R,R,R″...). Moreover—due to stronger internal reflections— more energy ”stays” inside the fiber, causing darkening of the colored highlights. **Right:** Virtual flux measurements using a particle tracing approach for an accurate simulation of scattering from a single fiber (see also Sec. 4.6). A cylindrical collector which is wraped around the fiber is used to estimate the exitant flux through the surface of the fiber, if a finite surface patch is illuminated from a fixed light direction. The local flux is exemplary sketched for the R- and the TRT-component.

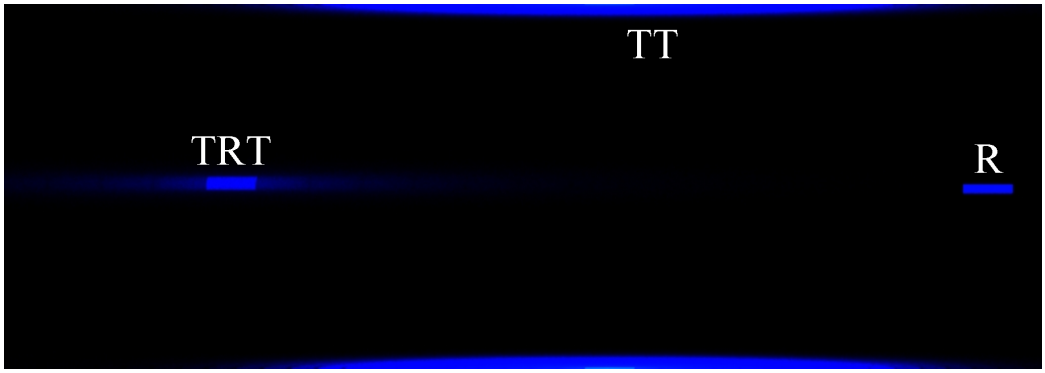

Fig. 2.9: Virtual flux measurement at a dry dielectric fiber with a circular cross section. The fiber consists of dielectric material (absorption: $10cm^{-1}$, index of refraction: 1.55) and exhibits surface and volumetric roughness leading to spatial and angular blurring of the first three scattering components (R,TT,TRT). A single surface patch of the fiber is illuminated by directional light (angle of incidence is 30° "from the right"). The flux is estimated as illustrated in Fig. 2.8 and the image shows the total flux at the (unwraped) cylindrical collector.

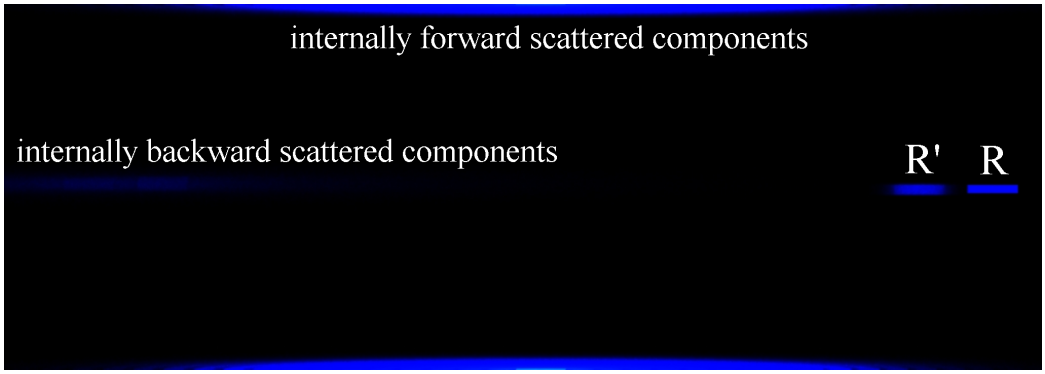

Fig. 2.10: Virtual flux measurement at a dielectric fiber (cf. Fig. 2.9) surrounded by a water layer (thickness of the water layer is 10% of the fiber diameter). Note the additional white highlights (compared to Fig. 2.9) and the overall darkening and blurring of the internally scattered components.

3. LIGHT SCATTERING FROM FILAMENTS

3.1 Introduction

Light scattering from a single filament is the basis of physically accurate rendering of fiber assemblies. As long as the light transport mechanisms for light scattering are understood and if the internal structure of a filament is perfectly known, rendering a single filament is usually not very challenging. In this case the filament could be basically modeled geometrically by structures having certain optical properties like index of refraction or absorption coefficient. However, for the frequent case of a scene consisting of a huge number of individual fibers (like hair, fur or woven knitwear) this explicit approach becomes impracticable due to its space and time complexity. It is also not clear a priori, how to deal with very complex or unknown scattering mechanisms or how efficient visualizations of fibers based on measurement data could be implemented.

In this section we introduce a novel concept similar to Bidirectional Scattering-Surface Reflectance Distribution Functions (BSSRDF) and Bidirectional Scattering Distribution Functions (BSDF) for surfaces in order to describe the light scattering from a filament. The basic idea is to locally approximate the scattering distribution by a function parameterized at the minimum enclosing cylinder of a straight infinite fiber, which is a first order approximation with respect to the curvature of the filament. We call this approximation a Bidirectional Fiber Scattering Distribution Function (BFSDF) (see section 3.5).

Based on the BFSDF we then derive further less complex scattering functions for different levels of geometric abstraction and for special lighting conditions, cf. Fig. 3.1. With the help of such scattering functions efficient physically based visualizations—adapted to a desired rendering technique or quality—become possible. Furthermore the BFSDF allows for systematic comparisons and classifica-

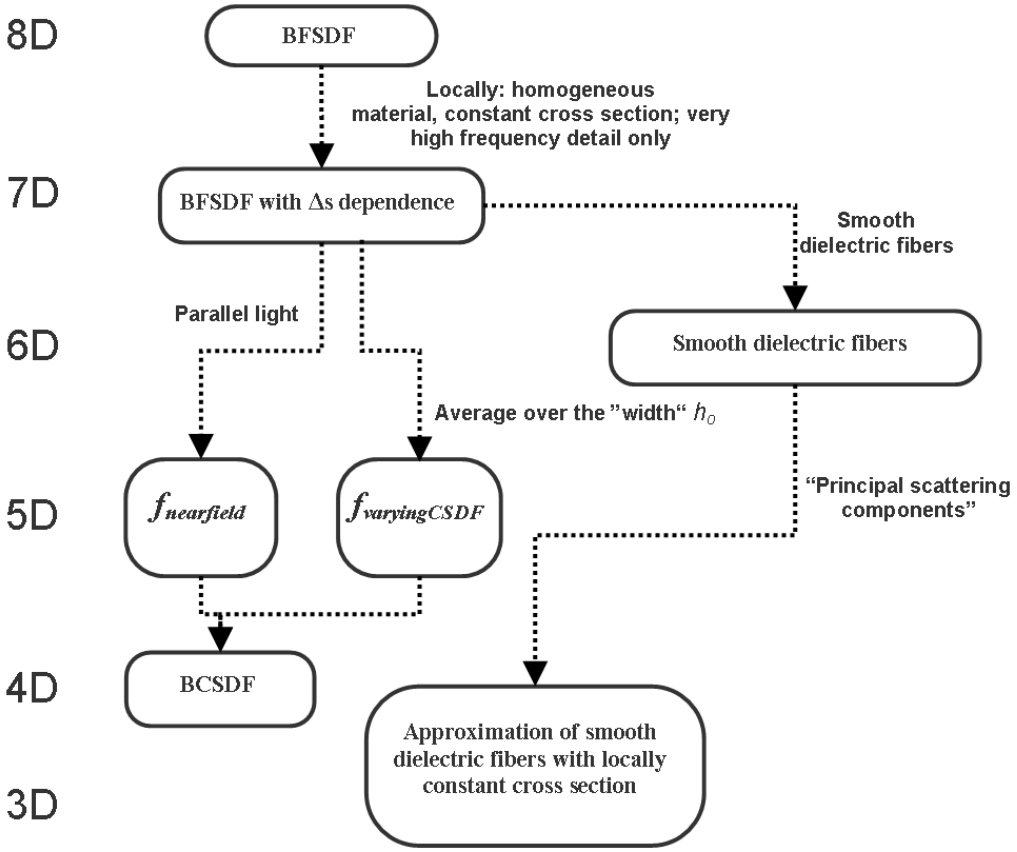

Fig. 3.1: Overview of the BFSDF and its special cases. The effective dimensions of the scattering functions are indicated on the left.

tions of fibers with respect to their scattering distributions, since it provides a uniform and shape independent radiance parameterization for filaments (see sections 3.6, 3.7 and 3.8). Moreover, we show that the existing models developed for hair rendering [25, 37] can be integrated in our framework, which also gives a basis to discuss their physical plausibility (section 3.9). We furthermore address some special cases where analytical solutions or approximations are available.

3.2 Related Work

Although progress has been made in rendering particular fibers with particular lighting settings no general formulation has been found. As a result some simplistic ad-hoc models were developed, especially in the realm of hair rendering [25, 12, 27]. All these models have no strong physical background and need substantial user interaction to yield physically plausible results. If the viewing or lighting conditions change such models may fail or have to be adopted.

Basically fibers could be modeled by conventional geometrical primitives (e.g. cylinders). Hence, in principal light scattering from filaments could be computed using existing scattering functions for surfaces and participating media. For surfaces the Bidirectional Scattering Distribution Function (BSDF) relates the incoming irradiance at an infinitesimal surface patch to the outgoing radiance from this patch [47]. It is an abstract optical material property which decouples microscopic features influencing the scattering behavior from the macroscopic shape of a surface and implies a constant wave length, a light transport taking zero time and being temporally invariant as well. With the BSDF of a certain material, the local surface normal and the incoming radiance, the outgoing radiance can be reconstructed. This BSDF concept works well for a wide range of materials but has one major drawback: Incoming irradiance contributes only to the outgoing radiance from a patch, if it directly illuminates this patch. Therefore it has to be generalized to take into account light transport inside the material. This generalization is called a Bidirectional Surface Scattering Distribution Function—BSSRDF [47]. Several papers have addressed some special cases mainly in the context of subsurface scattering [23, 41].

Further scattering models like the BTF or even more generalized radiance transfer functions have been introduced to account for self-shadowing and other mesoscopic and macroscopic effects [10]. For rendering of participating media commonly phase functions are used. Phase functions are very similar to the BSDF and describe volumetric scattering at a point in space.

In the realm of physically based fiber rendering Marschner et al. [37] presented an approach specialized in rendering human hair strands. They very briefly introduce a curve scattering function defined with respect to curve intensity (intensity

scattered per unit length of the curve) and curve irradiance (incoming power per unit length). Unfortunately no hint about how it can be derived for other types of fibers than hair is given. Another major restriction of the scattering model is that it describes far-field scattering only. This means that both observer (virtual camera) and light sources have to be distant to the hair fiber. If one of these two assumptions is violated it is very likely that the model introduces substantial bias. In particular for inter-reflections between neighboring fibers near-field effects play a prominent role. Therefore this approach is critical for rendering multiple fiber scattering, which is essential for light colored hair. A further issue is close-ups, since fine scattering detail across the width of a fiber can not be resolved (Fig.3.2).

Another field of application of fiber rendering is the visualization of woven cloth, where optical properties of a single yarn have to be taken into account. A ray-tracing based method for estimating the BSDF for a certain weaving pattern and cylindric fibers was sketched by Volevich et al. [61]. However, since all fibers are modeled explicitly the approach is very computationally costly. Gröller et al. proposed a volumetric approach for modeling knitwear [13]. They first measure the statistical density distribution of the cross section of a single yarn with respect to the arrangement of individual yarn fibers and then translate it along a three dimensional curve to form the entire filament. The results are looking quite impressive, but the question as to deal with yarns with more complex scattering properties is not addressed. A similar idea was presented by [67]. Here all computations base on a structure called lumislice, a light field of a yarn-cross-section. However, the authors do not discuss the problem of computing a physically based light field according to the properties of a single fiber of the yarn. Adabala et al. [1] describe another method for visualizing woven cloth. Due to the limitations of the underlying BRDF (Cook-Torance microfacet BRDF) realistic renderings of yarns with more complex scattering properties are impossible.

In the realm of applied optics, light scattering from straight smooth dielectric fibers with constant and mainly circular or elliptical cross sections were analyzed in a number of publications [3, 2, 4, 44, 39]. Schuh et al. [52] also introduced an approximation which is capable of predicting scattering of electro-magnetic waves from curved fibers. All these approaches are of very high quality, but are either more specialized in predicting the maxima positions of the scattering distri-

bution or rather impractical for rendering purposes because of their high numerical complexity.

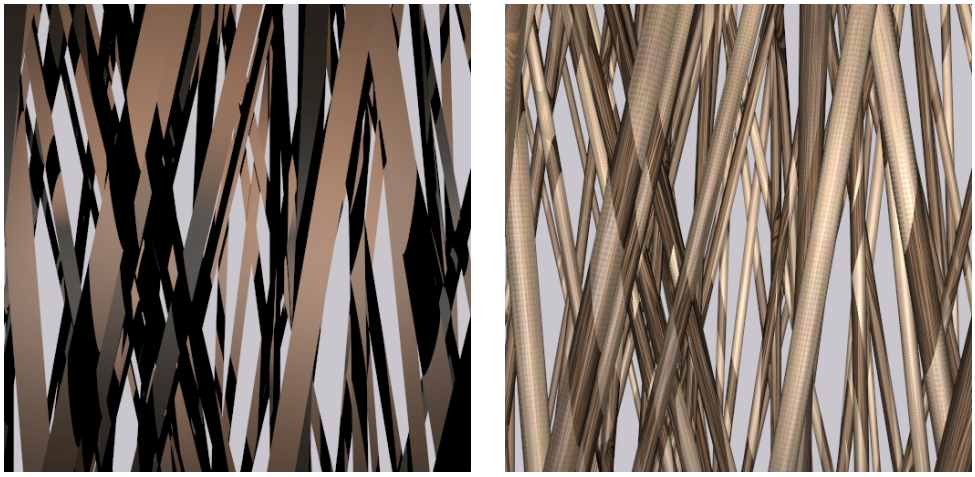

Fig. 3.2: A close-up rendered using a **Left:** far-field scattering and **Right:** a near-field scattering approach. Note the missing detail in the far-field result.

3.3 Motivation and General Assumptions

Over the last two decades it turned out that the BRDF/BSDF and the BSSRDF are very successful concepts to describe light scattering from surfaces. Our goal is to find similar approaches for fibers by adopting the basic ideas for surfaces to the realm of fiber optics. The general problem is very similar: How much radiance $\mathrm{d}L_o$ scattered from a single fiber one would observe from an infinitesimal surface patch $\mathrm{d}A_o$ in direction ω_o, if a surface patch $\mathrm{d}A_i$ is illuminated by an irradiance E_i from direction ω_i.

This interrelationship could be basically described by a BSSRDF at the surface of the fiber (Fig. 3.3 Left). Such a BSSRDF would in general depend on macroscopic deformations of the fiber, how the fiber is oriented and warped. As a consequence local (microscopic) fiber properties could not be separated from its global macroscopic geometry. Furthermore, all radiometric quantities must be parameterized with respect to the actual surface of the filament, which may not be well defined—e.g. in the case of a fluffy wool yarn.

Therefore we define a BSSRDF on the local infinite minimum enclosing cylinder rather than on the actual surface of the fiber in order to make the parameterization independent of the fiber's geometry (Fig. 3.3 Right). Thus the radiance transfer at the fiber is locally approximated by a scattering function on the minimum enclosing cylinder of a straight infinite fiber, which means a first order approximation with respect to the curvature. We call this function a *Bidirectional Fiber Scattering Distribution Function* (BFSDF). This approximation is accurate, if the influence of curvature to the scattering distribution can be neglected. This is the case if e.g.

- the filament's curvature is small compared to the radius of its local minimum enclosing cylinder or
- most of the incoming radiance only locally contributes to outgoing radiance.

The latter condition is satisfied for instance by opaque wires, since only reflection occurs and therefore no internal light transport inside the filament takes place. Hence, the scattering is a purely local phenomenon and the curvature of the fiber plays no role at all. The former condition for instance holds for hair and fur. In this case substantial internal light transport takes place, but since the curvature is small compared to the radius and since the light gets attenuated inside the fiber, the differences compared to a straight infinite fiber may be neglected. The higher the curvature and the more internal light transport takes place, the bigger the potential error that is introduced by a BFSDF.

3.4 Notations

Before technically defining the BFSDF we will give an overview of our notations. The local filament axis (tangent) is denoted $\vec{u}$ and we refer to the planes perpendicular to $\vec{u}$ as normal planes. All local surface normals lie within the local normal plane. All incoming and outgoing radiance is parameterized with respect to the local minimum enclosing cylinder of radius r oriented along $\vec{u}$ and is therefore independent of the actual cross section geometry of the filament (Fig. 3.4 Left). In the following we will consider a ray with direction $\vec{\omega}$ which is intersecting the

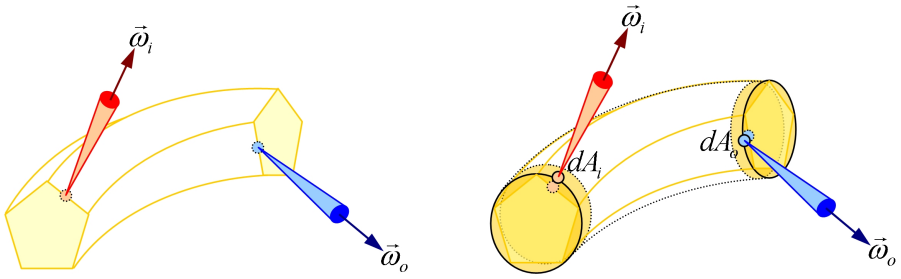

Fig. 3.3: Description of scattering at a fiber with a pentagonal cross section by: **Left:** a BSSRDF at the actual surface of the fiber. **Right:** a BFSDF at the local minimum enclosing cylinder.

minimum enclosing cylinder at a point $\vec{X}$. The infinitesimal surface patch centered around $\vec{X}$ will be denoted dA.

We introduce two sets of variables, which are suitable for certain measurement or lighting settings. The first parameter set describes $\vec{X}$ by its tangential position s along the tangent and its azimuthal position ξ within the normal plane (cylindrical coordinates). The direction $\vec{\omega}$ of a ray intersecting the cylinder is then given by two spherical angles α and β which span a hemisphere at $\vec{X}$ oriented along the local surface normal of the enclosing cylinder (Fig. 3.4 Right, Fig. 3.5 Right).

Typically this very intuitive way to parameterize both directions and positions is not very well suited to actual problems. In particular, this is the case for data acquisition and many "real world" lighting conditions. Hence, we introduce a second set of variables according to [37]. This set can be split into two groups, one parameterizing all azimuthal features within the normal plane (h, φ) and another parameterizing all longitudinal features along the tangent (s, θ). The angle θ denotes the inclination of $\vec{\omega}$ with respect to the normal plane, φ its azimuthal angle with respect to a fixed axis $\vec{v}$ and h an offset position of $\vec{X}$ at the minimum enclosing cylinder, measured within the normal plane. The variable s is the same as introduced before and always means the position along the axis of the minimum enclosing cylinder (Fig. 3.5).

We will now derive some useful transformation formulae for variables of both sets. The projection of the angle of incidence at the enclosing cylinder onto the

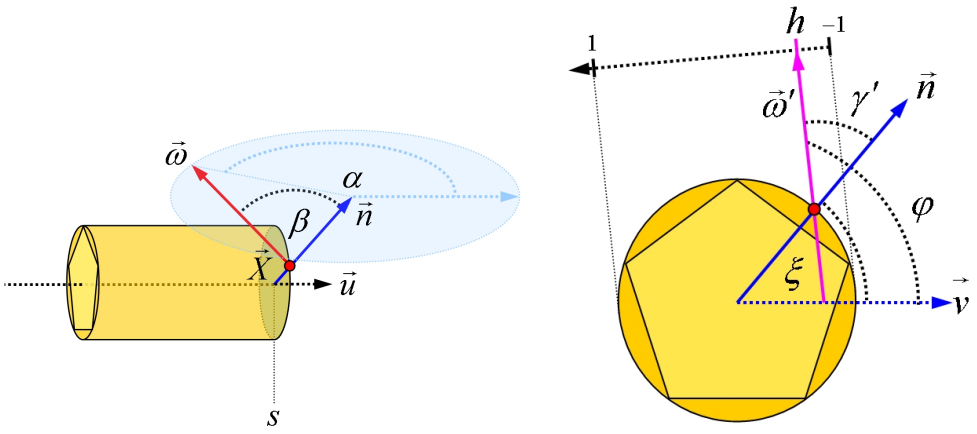

Fig. 3.4: **Left:** An "intuitive" variable set for parameterizing incoming and outgoing radiance at the minimum enclosing cylinder. The vector $\vec{u}$ denotes the local tangent (axis), s the position along this axis. The angles α and β span a hemisphere over the the surface patch at $\vec{X}$, with α being measured with respect to $\vec{u}$ within the tangent plane and β with respect to the local surface normal $\vec{n}$. **Right:** Azimuthal variables of the first and the second parameter set. The parameter h is an offset position at the perimeter. Note that parallel rays have same φ (measured counterclockwise with respect to $\vec{u}$) but different h.

normal plane γ' is given by the following two equations:

$$\cos\gamma' = \frac{\cos\beta}{\cos\theta} \tag{3.1}$$

$$\gamma' = |\arcsin h| \tag{3.2}$$

Thus for the spherical angle β we have:

$$\beta = \arccos\left(\cos\theta\sqrt{1-h^2}\right). \tag{3.3}$$

The following relation holds between ξ, φ and h, cf. Fig. 3.4 Right:

$$\xi = \begin{cases} \varphi + \arcsin h & 0 \le \varphi + \arcsin h < 2\pi \\ 2\pi + \varphi + \arcsin h & \varphi + \arcsin h < 0 \\ \varphi + \arcsin h - 2\pi & \varphi + \arcsin h \ge 2\pi \end{cases} \tag{3.4}$$

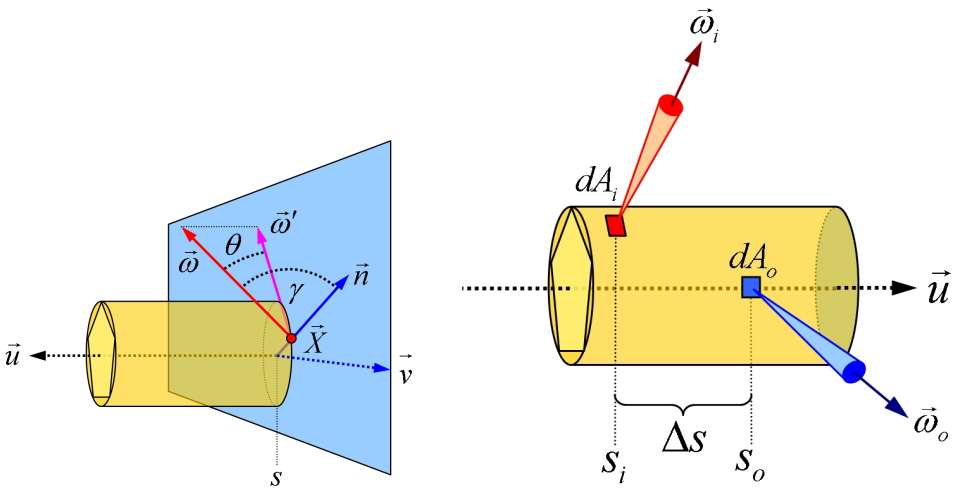

Fig. 3.5: **Left:** Parameterization with respect to the normal plane and filament axis (tangent) $\vec{u}$. The vector $\vec{\omega}'$ denotes the projection of a direction $\vec{\omega}$ onto the normal plane. The angle θ ranges from $-\pi/2$ to $\pi/2$, with $\theta = \pi/2$ if $\vec{u}$ and $\vec{\omega}$ are pointing in the same direction. **Right:** Parameterization of the BFSDF.

The spherical coordinate α equals the angle between the projection of $\vec{\omega}$ onto the local tangent plane and $\vec{v}$. Since the angle between $\vec{\omega}$ and $\vec{v}$ is given by $\pi/2-\theta$ and the inclination of $\vec{D}$ with respect to the tangent plane is $\pi/2-\beta$ one obtains:

$$\begin{aligned} \cos\alpha &= \cos(\pi/2-\theta)/\cos(\pi/2-\beta) \\ &= \sin\theta/\sin\beta \\ &= \frac{\sin\theta}{\sqrt{1-(1-h^2)\cos^2\theta}}. \end{aligned} \tag{3.5}$$

Furthermore, the actual angle depends on the sign of h:

$$\alpha = \begin{cases} \arccos\left(\frac{\sin\theta}{\sqrt{1-(1-h^2)\cos^2\theta}}\right), & h \leq 0, \\ 2\pi - \arccos\left(\frac{\sin\theta}{\sqrt{1-(1-h^2)\cos^2\theta}}\right), & h > 0. \end{cases} \tag{3.6}$$

3.5 Bidirectional Fiber Scattering Distribution Function — BFSDF

We now technically define the **B**idirectional **F**iber **S**cattering **D**istribution **F**unction (BFSDF) of a fiber. Please note that for further considerations all radiometric quantities at the minimum enclosing cylinder are implicitly transformed by a transformation that unwraps the cylinder to a plane. By applying such a transformation the local surface normals of the cylinder become equally aligned. As a consequence the angles α and β can be expressed with respect to a global coordinate system.

The BFSDF relates incident flux Φ_i at an infinitesimal surface patch $\mathrm{d}A_i$ to the outgoing radiance L_o at another position on the minimum enclosing cylinder:

$$f_{\mathrm{BFSDF}}(s_i,\xi_i,\alpha_i,\beta_i,s_o,\xi_o,\alpha_o,\beta_o) := \frac{\mathrm{d}L_o(s_i,\xi_i,\alpha_i,\beta_i,s_o,\xi_o,\alpha_o,\beta_o)}{\mathrm{d}\Phi_i(s_i,\xi_i,\alpha_i,\beta_i)}. \tag{3.7}$$

Using the BFSDF the local orientation of a fiber and the incoming radiance L_i, the total outgoing radiance of a particular position can be calculated by integrating the irradiance over all surface patches and all incoming directions as follows:

$$\begin{aligned} L_o(s_o,\xi_o,\alpha_o,\beta_o) \;=\; & \int_{-\infty}^{+\infty}\int_{0}^{2\pi}\int_{0}^{2\pi}\int_{0}^{\pi/2} f_{\mathrm{BFSDF}}(s_i,\xi_i,\alpha_i,\beta_i,s_o,\xi_o,\alpha_o,\beta_o)\, L_i(s_i,\xi_i,\alpha_i,\beta_i) \\ & \sin\beta_i\cos\beta_i \mathrm{d}\beta_i\,\mathrm{d}\alpha_i\,\mathrm{d}\xi_i\,\mathrm{d}s_i. \end{aligned} \tag{3.8}$$

For a physically based BFSDFs the energy is conserved, thus all light entering the enclosing cylinder is either absorbed or scattered. In case of perfectly circular symmetric filaments the BFSDF in addition satisfies the Helmholtz Reciprocity:

$$f_{\mathrm{BFSDF}}(s_i,\xi_i,\alpha_i,\beta_i,s_o,\xi_o,\alpha_o,\beta_o) = f_{\mathrm{BFSDF}}(s_o,\xi_o,\alpha_o,\beta_o,s_i,\xi_i,\alpha_i,\beta_i). \tag{3.9}$$

If the optical properties of a fiber are constant along s, then the BFSDF does not depend on s_i and s_o but on the difference $\Delta s := s_o - s_i$. Thus the dimension of

the BFSDF function decreases by one and the scattering integral reduces to the following equation:

$$L_o(s_o,\xi_o,\alpha_o,\beta_o) = \int_{-\infty}^{+\infty}\int_0^{2\pi}\int_0^{2\pi}\int_0^{\pi/2} f_{\mathrm{BFSDF}}(\Delta s,\xi_i,\alpha_i,\beta_i,\xi_o,\alpha_o,\beta_o)\, L_i(s_i,\xi_i,\alpha_i,\beta_i) \sin\beta_i\cos\beta_i\,\mathrm{d}\beta_i\,\mathrm{d}\alpha_i\,\mathrm{d}\xi_i\,\mathrm{d}\Delta s. \tag{3.10}$$

This special case is also an appropriate approximation for the general case if the following condition is satisfied:

- The cross section shape and material properties vary slowly along s or
- have only very high frequency detail on a scale which does not has to be resolved by the BFSDF.

Good examples for high frequency detail are cuticula tiles of hair fibers or surface roughness due to the microstructure of a filament. Since this assumption is at least locally valid for a wide range of different fibers, we will restrict ourselves to this case in the following.

The BFSDF and its corresponding rendering integral was introduced with respect to the "intuitive variable set" first. We now derive a formulation for the second variable set. Reparameterizing the scattering integral yields:

$$L_o(s_o,h_o,\varphi_o,\theta_o) = \int_{-\infty}^{+\infty}\int_{-1}^{1}\int_0^{2\pi}\int_{-\pi/2}^{\pi/2} \left|\frac{\partial(\xi_i,\alpha_i,\beta_i)}{\partial(h_i,\varphi_i,\theta_i)}\right| f_{\mathrm{BFSDF}}(\Delta s,h_i,\varphi_i,\theta_i,h_o,\varphi_o,\theta_o) L_i(s_i,h_i,\varphi_i,\theta_i)\sqrt{1-\cos^2\theta_i\left(1-h_i^2\right)}\sqrt{1-h_i^2}\cos\theta_i \mathrm{d}\theta_i\,\mathrm{d}\varphi_i\,\mathrm{d}h_i\,\mathrm{d}\Delta s. \tag{3.11}$$

The above equation can be finally simplified to the following equation (see also App. 7.3):

$$L_o(s_o,h_o,\varphi_o,\theta_o) = \int_{-\infty}^{+\infty}\int_{-1}^{1}\int_{0}^{2\pi}\int_{-\pi/2}^{\pi/2} f_{\mathrm{BFSDF}}(\Delta s,h_i,\varphi_i,\theta_i,h_o,\varphi_o,\theta_o) \cos^2\theta_i L_i(s_i,h_i,\varphi_i,\theta_i)\,\mathrm{d}\theta_i\,\mathrm{d}\varphi_i\,\mathrm{d}h_i\,\mathrm{d}\Delta s. \quad (3.12)$$

This form of the scattering integral is especially suitable when having distant lights, i.e. parallel illumination, since parallel rays of light have same φ_i and θ_i but different h_i. Consider for example directional lighting, which can be expressed by the radiance distribution $L(\varphi_i',\theta_i',\varphi_i,\theta_i) = E_\perp(\varphi_i',\theta_i')\delta(\varphi_i-\varphi_i')\delta(\theta_i-\theta_i')/\cos\theta_i$ with normal irradiance $E_\perp(\varphi_i',\theta_i')$. Substituting the radiance in the scattering integral by this distribution yields the following special case:

$$L_o(h_o,\varphi_o,\theta_o) = E_\perp(\varphi_i',\theta_i')\cos\theta_i' \int_{-\infty}^{+\infty}\int_{-1}^{1} f_{\mathrm{BFSDF}}\left(\Delta s,h_i,\varphi_i',\theta_i',h_o,\varphi_o,\theta_o\right)\mathrm{d}h_i\mathrm{d}\Delta s. \quad (3.13)$$

All formulae derived in this section hold for a single filament only. But a typical scene consists of a substantial number of densely packed fibers. Since incoming and outgoing radiance was parameterized with respect to the minimum enclosing cylinder, those cylinders must not intersect. Otherwise it can not be guaranteed that the results are still valid (Fig. 3.6 Left). If a cross section shape closely matches the enclosing cylinder the maximum overlap is very small. Hence, computing the light transport at a projection of the overlapping regions onto the enclosing cylinder can be seen as a good approximation of the actual scattering.

3.6 Dielectric Fibers

Since most filaments consist of dielectric material it is very instructive to analyze the scattering from dielectric fibers. For perfectly smooth dielectric filaments with arbitrary but constant cross section the dimension of the BFSDF reduces from seven to six. This is a direct consequence of the fact that light entering at a certain

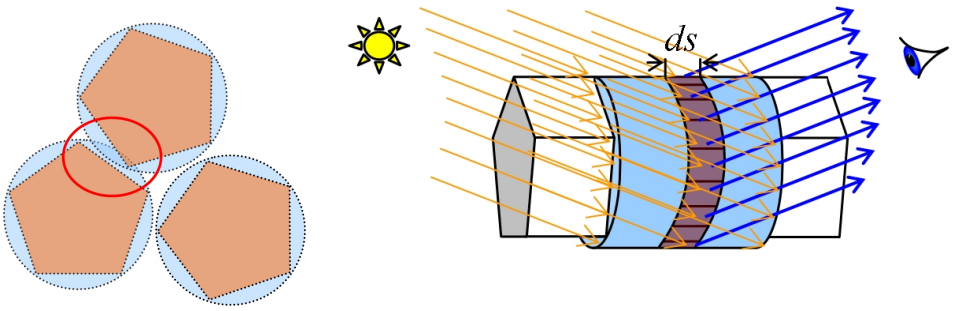

Fig. 3.6: **Left:** Cross section of three very densely packed fibers. The problematic intersection of two enclosing cylinders is marked by an ellipse. **Right:** A slice at the minimum enclosing cylinder illuminated by parallel light and viewed by a distant observer.

inclination will always exit at the same inclination (according to absolute value), regardless of the sequence of refractions and reflections it undergoes. Thus—neglecting longitudinal positions s—all scattered light lies on a cone.

The incident light is reflected or refracted several times before it leaves the fiber. The amount of light being reflected resp. refracted is given by Fresnel's Law. At each surface interaction step the scattered intensity of a ray decreases—except in case of total reflection. If absorption inside the fiber takes place, then loss of energy is even more prominent. Since an incoming ray of light does not exhibit spatial or angular blurring, the BFSDF is characterized by discrete peaks. Therefore, it makes sense to analyze only those scattering components with respect to their geometry and attenuation which:

- can be measured outside the fiber and
- have an intensity bigger than a certain given threshold.

As a result, the BFSDF can be approximated very well by the distribution of its strongest peaks. Then the effective complexity further reduces to three dimensions, since all scattering paths and thereby all scattering components are fully determined by h_i, φ_i and θ_i which are needed to compute the attenuation.

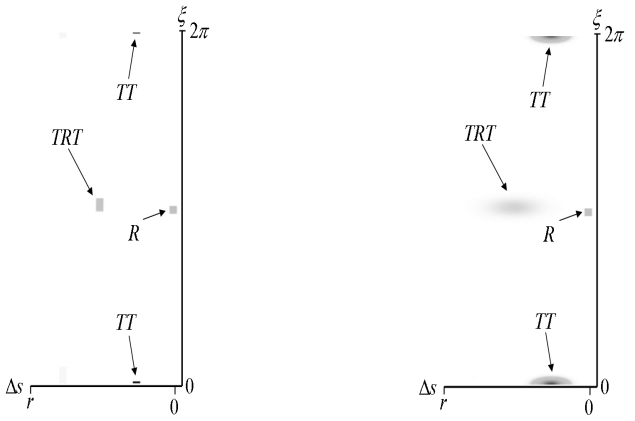

Fig. 3.7: The left diagram shows the distribution of scattered light at a perfect smooth dielectric circular cylinder obtained with Monte Carlo particle tracing. The intensity of the scattered light is computed with respect to ξ and Δs at the cylindric shell: the darker the grey, the higher the outgoing flux through the surface. A single light source is illuminating a small rectangular surface patch at $s = 0$ from direction $\varphi = \pi$ and $\theta = 0.2$. The direct surface reflection component (R), the forward scattered component (TT) and the first order caustic (TRT) are clearly and sharply visible. The right image shows the same scene but a dielectric cylinder with volumetric scattering. As a consequence both TT and TRT components are blurred. Note that the structure of the scattering distribution (i.e. the position of the peaks and their relative intensities) does not change.

Having n such components the BFSDF may be factorized:

$$\begin{aligned} f_{\mathrm{BFSDF}}(\Delta s, h_i, \varphi_i, \theta_i, h_o, \varphi_o, \theta_o) &\approx \sum_{j=1}^{n} f^j_{\mathrm{BFSDF}}(\Delta s, h_i, \varphi_i, \theta_i, h_o, \varphi_o, \theta_o) \\ &= \frac{\delta_\theta(\theta_i + \theta_o)}{\cos^2\theta_i} \sum_{j=1}^{n} \delta^j_s(\Delta s - \lambda^j_s(h_o, \varphi_o, \theta_o)) \\ &\quad \delta^j_\varphi(\varphi_i - \lambda^j_\varphi(h_o, \varphi_o, \theta_o))\delta^j_h(h_i - \lambda^j_h(h_o, \varphi_o, \theta_o)) \\ &\quad a^j(h_o, \varphi_o, \theta_o). \end{aligned} \tag{3.14}$$

The first factor δ_θ says that intensity can only be measured, if $\theta_o = -\theta_i$. Since no blurring of the scattered ray of light occurs, all other factors describing the scattering geometry can be formalized by Dirac delta distributions, too. Because rays

entering the enclosing cylinder at s_i propagate into longitudinal direction, they usually exit the enclosing cylinder at another longitudinal position s. The functions λ_s^j account for this relationship between s_i and s and the two functions λ_φ^j and λ_h^j characterize the actual scattering geometry (the paths of the projection of the ray paths onto the normal plane). The factor a^j is the attenuation for the j-th component. These attenuation factors include Fresnel factors as well as absorption. Due to Bravais Law (App. 7.2) all λ^j and a^j can be directly derived from the 2D analysis of the optics at the cross section of a fiber within the normal plane together with a modified index of refraction (depending on the incoming inclination θ_i, see next section).

Note that the factor $(\cos\theta_i)^{-2}$ in front of (3.14) compensates for:

- the integration measure with respect to θ_i,h_i and φ_i which contributes a factor of $(\cos\theta_i)^{-1}$ and

- the cosine of the angle of incidence which gives another $(\cos\theta_i)^{-1}$.

Even though this kind of BFSDF is for smooth dielectric materials with absorption and locally constant cross section only, its basic structure is very instructive for a lot of other types of fibers, too. For example internal volumetric scattering or surface scattering—due to surface roughness—do not change this basic structure in most cases but result in spatial and angular blurring, cf. Fig. 3.7. By replacing the δ-distributions in the BFSDF for smooth dielectric cylinders—cf.(3.15)—with normalized lobes (like Gaussians) centered over the peak similar effects can be simulated easily.

The presence of sharp peaks in the scattering distribution is not only a characteristic of dielectric fibers with constant cross section, but of most other types of (even not dielectric) fibers with locally varying cross section shape, too. If the variation is periodic and of a very high frequency these peaks are typically shifted or blurred in longitudinal directions, compared to a fiber without this high frequency detail. Nevertheless Bravais Law only holds for constant cross sections. Hence (3.14) has to be adopted to other cases. At least it can be seen as a basis for efficient compression schemes and a starting point for analytical BFSDFs.

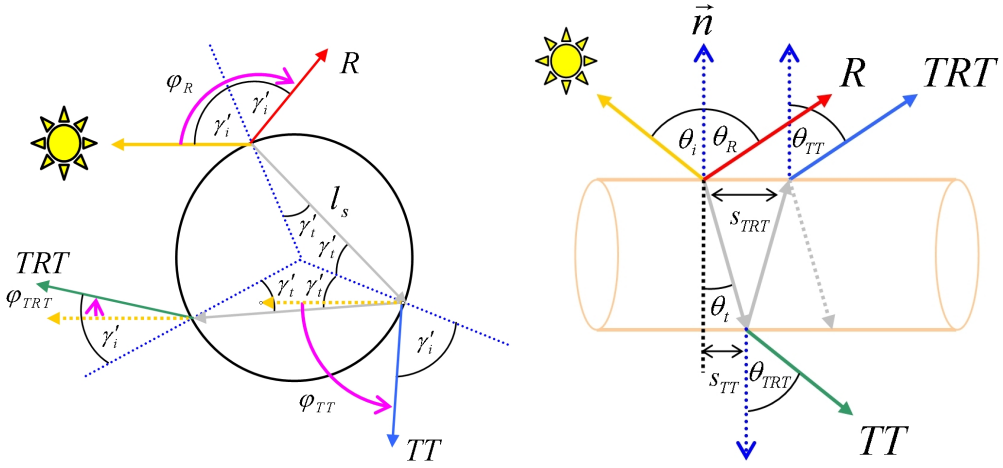

Fig. 3.8: **Left:** Azimuthal scattering geometry of the first three scattering modes (R,TT,TRT) within the normal plane for a fiber with circular cross section. The relative azimuths are denoted ϕ_R, ϕ_{TT} and ϕ_{TRT}. Here the projection of the angle of incidence onto the normal plane is γ_i' and the angle of refraction γ_r' respectively. Note that the outgoing ray leaves the fiber always at $-h_i$. **Right:** Longitudinal scattering geometry of the first three scattering modes (R,TT,TRT) at a dielectric fiber. Note that the outgoing inclinations θ_R,θ_{TT} and θ_{TRT} always equal $-\theta_i$. The difference of the longitudinal outgoing positions with respect to incoming position s_i are denoted s_{R}, s_{TT} and s_{TRT}.

3.6.1 Dielectric Cylinder

In section 2.1.2 it was shown that all important features of light scattering from human hair fibers can be basically explained by a glass cylinder model. Moreover, this model is an adequate approximation for many other kinds of fibers. Hence, it is very instructive to analyze the scattering from a cylindric fiber made of colored dielectric material, which was already partially discussed in [3], [52] and [37].

Consider a solid dielectric cylindric fiber of radius r. We restrict ourselves to the first three scattering components (Fig. 4.22), dominating the visual appearance and denote them according to section 2.1.2:

- The first backward scattering component, a direct (white) surface reflection (R-component)

- The first forward scattering component, light that is two times transmitted through the cylinder (TT-component)
- The second backward scattering component, light which enters the cylinder and gets internally reflected (TRT-component)

Hence, according to (3.14), the resulting BFSDF is a superposition of three independent scattering functions, each accounting for one of the three modes:

$$f_{\text{BFSDF}}^{\text{cylinder}} \approx \frac{\delta_\theta}{\cos^2\theta_i}(\delta_s^{\text{R}}\delta_\varphi^{\text{R}}\delta_h^{\text{R}}a^{\text{R}} + \delta_s^{\text{TT}}\delta_\varphi^{\text{TT}}\delta_h^{\text{TT}}a^{\text{TT}} + \delta_s^{\text{TRT}}\delta_\varphi^{\text{TRT}}\delta_h^{\text{TRT}}a^{\text{TRT}}). \tag{3.15}$$

Neglecting the attenuation factors a^{R}, a^{TT}, and a^{TRT} this BFSDF can be derived by tracing the projections of rays within the normal plane (Fig. 4.22 Left). Rays entering the cylinder at an offset h_i always exit at $-h_i$. Furthermore intensity can only be measured, if the relative azimuth $\phi = M[\varphi_o - \varphi_i]$ equals φ_R for the R-component, φ_{TT} for the TT-component or φ_{TRT} for the TRT-component. Here, the operator M maps the difference angle $\varphi_o - \varphi_i$ to an interval $(-\pi, \pi]$:

$$M[\alpha] = \begin{cases} \alpha, & -\pi < \alpha \leq \pi \\ \alpha - 2\pi, & \pi < \alpha \leq 2\pi \\ \alpha + 2\pi, & -2\pi \leq \alpha \leq -\pi \end{cases} \tag{3.16}$$

For the relative azimuths the following equations hold, cf. Fig. 4.22 Left:

$$\varphi_{\text{R}} = 2\gamma_i' \tag{3.17}$$

$$\varphi_{\text{TT}} = M\left[\pi + 2\gamma_i' - 2\gamma_t'\right] \tag{3.18}$$

$$\varphi_{\text{TRT}} = 2\gamma_i' - 4\gamma_t' \tag{3.19}$$

Due to Bravais Law all azimuths are calculated from 2D-scattering within the normal plane with help of a modified index of refraction

$$n' = \frac{\sqrt{n^2 - \sin^2\theta_i}}{\cos\theta_i}$$

(instead of the relative refractive index n) and Snell's Law (App. 7.2,7.1.2). The projected (signed) angle of incidence light is denoted γ_i' and equals $\arcsin h_i$. Its corresponding (signed) angle of refraction is $\gamma_t' = \arcsin(h_i/n')$.

Because rays entering the cylinder at a position s_i propagate into longitudinal s-direction, they leave the fiber at another positions s_{TT} and s_{TRT}, respectively. In case of direct surface reflection (R-mode) the light is reflected at the incoming position s_i. The two positions s_{TT} and s_{TRT} are directly related to the length covered by the ray inside the cylinder. For the TT component this length l can be calculated from its projection onto the normal plane l_s, and the longitudinal angle of refraction θ_t (see Fig. 4.22):

$$l = \frac{l_s}{\cos\theta_t} = \frac{2r\cos\gamma_t'}{\cos\theta_t} \tag{3.20}$$

with $\theta_t = -\operatorname{sgn}(\theta_i)\arccos((n'/n)\cos\theta_i)$ (see also App. 7.2). This length doubles for rays of the TRT-mode.

Therefore for the positions s_{TT} and s_{TRT} the following holds:

$$s_{\mathrm{TT}} = -\operatorname{sgn}\theta_i\sqrt{l^2 - l_s^2} = l_s\tan\theta_t \tag{3.21}$$

$$s_{\mathrm{TRT}} = 2l_s\tan\theta_t \tag{3.22}$$

Putting all geometric analysis together the geometry terms λ introduced in the previous section are:

$$\begin{aligned}
&\lambda_s^{\mathrm{R}} = 0; \lambda_s^{\mathrm{TT}} = s_{\mathrm{TT}}; \lambda_s^{\mathrm{TRT}} = s_{\mathrm{TRT}}\\
&\lambda_h^{\mathrm{R}} = \lambda_h^{\mathrm{TT}} = \lambda_h^{\mathrm{TRT}} = -h_o\\
&\lambda_\varphi^{\mathrm{R}} = \varphi_o + 2\arcsin h_o\\
&\lambda_\varphi^{\mathrm{TT}} = \varphi_o + M\left[\pi + 2\arcsin(h_o) - 2\arcsin(h_o/n')\right]\\
&\lambda_\varphi^{\mathrm{TRT}} = \varphi_o - 4\arcsin(h_o/n') + 2\arcsin h_o
\end{aligned} \tag{3.23}$$

For smooth dielectric cylinders the R component gets attenuated by Fresnel reflectance (see App 7.1.3) only:

$$a^R = \mathrm{Fresnel}_{\mathrm{R}}$$

$$= \mathrm{F}(n', \tilde{n}', \gamma_t'). \tag{3.24}$$

According to [37] the index n' is used to calculate the reflectance for perpendicular polarized light, whereas another index of refraction $\tilde{n}' = n^2/n'$ is used for parallel polarized light.

For the two other modes (TT, TRT) a ray gets attenuated at each reflection rsp. refraction event. Hence for the corresponding Fresnel factors $\mathrm{Fresnel}_{\mathrm{TT}}$ and $\mathrm{Fresnel}_{\mathrm{TRT}}$ the following equations hold:

$$\mathrm{Fresnel}_{\mathrm{TT}} = (1 - a^R)(1 - \mathrm{F}(1/n', 1/\tilde{n}', \gamma_t')) \tag{3.25}$$

$$\mathrm{Fresnel}_{\mathrm{TRT}} = \mathrm{Fresnel}_{\mathrm{TT}}\mathrm{F}(1/n', 1/\tilde{n}'', \gamma_t') \tag{3.26}$$

If a ray enters the cylinder, as is the case for both the TT and TRT modes, absorption takes place. For homogenous materials the attenuation only depends on the length of the internal path—i.e. the absorption length—and the absorption coefficient σ. For the TT component the absorption length equals l and a ray of the TRT mode covers twice this distance inside the cylinder. Note that the absorption length given in [37] (which was $l = (2 + 2\cos\gamma_t')/\cos\theta_t$) is wrong and should be replaced by (3.20).

Hence the total attenuation factors with absorption are

$$a^{\mathrm{TT}} = \mathrm{Fresnel}_{\mathrm{TT}}\, e^{-\sigma l}, \tag{3.27}$$

$$a^{\mathrm{TRT}} = \mathrm{Fresnel}_{\mathrm{TRT}}\, e^{-2\sigma l}. \tag{3.28}$$

Note that higher order scattering can be analyzed in a straight forward way, since analytical solutions for the corresponding geometry terms λ are available.

3.7 Far-Field Approximation and BCSDF

"Real world" filaments are typically very thin and long structures. Hence, compared to its effective diameter both viewing and lighting distances are typically

Fig. 3.9: Close-up of an oval made of bluish plastic. **Left:** BFSDF rendering, **Right:** BCSDF approximation of the BFSDF rendering. Here the exitant radiance is averaged over the width. Note the scattering details of the BFSDF version which are missing in the BCSDF rendering.

very large. Therefore all surface patches along the normal plane have equal (φ_o, θ_o) and the fibers cross section is locally illuminated by parallel light (of constant radiance) from a fixed direction (φ_i, θ_i). Furthermore adjacent surface patches of the local minimum enclosing cylinder have nearly the same distance to both light source and observer.

When rendering such a scene the screen space width of a filament is less or in the order of magnitude of a single pixel. In this case fibers can be well approximated by curves having a cross section proportional to the diameter of the minimum enclosing cylinder D.

That allows us to introduce a simpler scattering formalism to further reduce rendering complexity which we call *far-field* approximation.

Using similar quantities as Marschner et al. [37]—curve radiance and curve irradiance—we show how an appropriate scattering function can be derived right from the BFSDF. The *curve radiance* $\mathrm{d}\bar{L}_o$ is the averaged outgoing radiance along the width of the fibers minimum enclosing cylinder times its effective diameter (Fig. 3.6 Right).

Assuming parallel light from direction (φ_i, θ_i) being constant across the width of a fiber this curve radiance can be computed by averaging the outgoing radiance across the width:

$$\begin{aligned} \mathrm{d}\bar{L}_o(\varphi_i, \theta_i, \varphi_o, \theta_o) &:= \frac{D}{\pi} \int_{\varphi_o-\pi/2}^{\varphi_o+\pi/2} \cos(\xi_o - \varphi_o) \\ &\quad \mathrm{d}L_o(\varphi_i, \theta_i, \xi_o, \alpha_o(\theta_o, h_o(\xi_o, \varphi_o)), \beta_o(\theta_o, h_o(\xi_o, \varphi_o)))\mathrm{d}\xi_o. \end{aligned} \tag{3.29}$$

Here a factor of $\cos(\xi_o - \varphi_o)$ accounts for the projected width of the minimum enclosing cylinder. Notice that for the integration with respect to ξ_o one has to take into account its transition of from zero to 2π properly. Using the other set of variables this can be transformed to:

$$\mathrm{d}\bar{L}_o(\varphi_i, \theta_i, \varphi_o, \theta_o) = \frac{D}{2} \int_{-1}^{1} \mathrm{d}L_o(h_o, \varphi_i, \theta_i, \varphi_o, \theta_o)\, \mathrm{d}h_o. \tag{3.30}$$

Since we assume constant incident radiance $L_i(\varphi_i, \theta_i)$, $\mathrm{d}L_o$ may be substituted by:

$$\begin{aligned} \mathrm{d}L_o(\varphi_i, \theta_i, h_o, \varphi_o, \theta_o) &= \cos^2\theta_i L_i(\varphi_i, \theta_i)\mathrm{d}\varphi_i \mathrm{d}\theta_i \mathrm{d}h_o \int_{-1}^{1} \int_{-\infty}^{\infty} \\ &\quad f_{\mathrm{BFSDF}}(\Delta s, h_i, \varphi_i, \theta_i, h_o, \varphi_o, \theta_o)\, \mathrm{d}\Delta s\, \mathrm{d}h_i \end{aligned} \tag{3.31}$$

which yields:

$$\begin{aligned} \mathrm{d}\bar{L}_o(\varphi_i, \theta_i, \varphi_o, \theta_o) &= \frac{D}{2} L_i(\varphi_i, \theta_i) \cos^2\theta_i \mathrm{d}\varphi_i \mathrm{d}\theta_i \int_{-1}^{1} \int_{-1}^{1} \int_{-\infty}^{\infty} \\ &\quad f_{\mathrm{BFSDF}}(\Delta s, h_i, \varphi_i, \theta_i, h_o, \varphi_o, \theta_o)\, \mathrm{d}\Delta s\, \mathrm{d}h_i \mathrm{d}h_o \end{aligned} \tag{3.32}$$

This scattered radiance $\mathrm{d}\bar{L}_o$ is proportional to the incoming *curve irradiance* $\mathrm{d}\bar{E}_i$:

$$\mathrm{d}\bar{E}_i(\varphi_i,\theta_i) := DL_i(\varphi_i,\theta_i)\cos^2\theta_i \mathrm{d}\varphi_i \mathrm{d}\theta_i. \tag{3.33}$$

Thus, a new bidirectional far-field scattering distribution function for curves f_{BCSDF} that assumes distant observer and distant light sources can be defined. It relates the incoming curve irradiance to the averaged outgoing radiance across the width (curve radiance). We will call this far-field approximation the **B**idirectional **C**urve **S**cattering **D**istribution **F**unction (BCSDF).

$$f_{\mathrm{BCSDF}}(\varphi_i,\theta_i,\varphi_o,\theta_o) := \frac{\mathrm{d}\bar{L}_o(\varphi_i,\theta_i,\varphi_o,\theta_o)}{\mathrm{d}\bar{E}_i(\varphi_i,\theta_i)}. \tag{3.34}$$

With (3.32) and (3.33) we obtain:

$$f_{\mathrm{BCSDF}}(\varphi_i,\theta_i,\varphi_o,\theta_o) = \frac{1}{2}\int_{-1}^{1}\int_{-1}^{1}\int_{-\infty}^{\infty} f_{\mathrm{BFSDF}}(\Delta s,h_i,\varphi_i,\theta_i,h_o,\varphi_o,\theta_o)\,\mathrm{d}\Delta s\,\mathrm{d}h_i\,\mathrm{d}h_o. \tag{3.35}$$

Finally, in order to compute the total outgoing curve radiance one has to integrate all incoming light over a sphere with respect to φ_i and θ_i:

$$\bar{L}_o(\varphi_o,\theta_o) = D\int_{0}^{2\pi}\int_{-\pi/2}^{\pi/2} f_{\mathrm{BCSDF}}(\varphi_i,\theta_i,\varphi_o,\theta_o)L_i(\varphi_i,\theta_i)\cos^2\theta_i \mathrm{d}\theta_i\,\mathrm{d}\varphi_i. \tag{3.36}$$

This equation matches the rendering integral given in [37, equation 1] in the specific context of hair rendering. Thus the BCSDF is identical to the fiber scattering function very briefly introduced in [37]. In contrast to [37] our derivation shows the close connection between the BFSDF and the BCSDF. In our formalism the

BCSDF is just one specific approximation of the BFSDF and can be computed directly from (3.55).

Besides of the advantage of being less complex than the BFSDF the BCSDF can help to drastically reduce sampling artifacts which would be introduced by subtle BFSDF detail like very narrow scattering lobes. Nevertheless there are some drawbacks. First of all local scattering effects are neglected which restricts the possible fields of application of the BCSDF in case of close-ups (Fig. 3.9). Furthermore, since the fiber properties are averaged over the width, the entire width—at least in the statistical average—has to be visible. Otherwise undesired artifacts may occur. Finally the BCSDF is not adequate for computing indirect illumination due to multiple fiber scattering in dense fiber clusters, since the far-field assumption is violated in such a case.

3.8 Further Special Cases

Although a distant observer and distant light sources are commonly assumed for rendering, there may be cases where only one of these two assumptions is fulfilled. For these cases further approximations of the BFSDF are straight forward and can be derived similarly to the BCSDF. In particular we now discuss the following two special cases:

- a close observer and locally constant incident lighting: near field scattering with constant incident lighting
- a distant observer with locally varying incident lighting: curve scattering with locally varying incident lighting

Other special cases arise in the context of low frequency lighting. Suppose for example an incident illumination given by a spherical harmonics representation [54]. In this case it is useful to pre-compute scattering with respect to the spherical harmonics basis functions. Based on such pre-computed scattering functions the exitant radiance can be estimated very quickly according to the linear combination of incident lighting.

3.8.1 Near-Field Scattering with Constant Incident Lighting

A BCSDF may be a good approximation for distant observers, but it fails when it comes to close-ups. Since the outgoing radiance is averaged across the width of a filament local scattering details can not be resolved. However, if incident illumination can be assumed locally constant (like in the case of distant light sources) the outgoing radiance $\mathrm{d}L(\varphi_i, \theta_i, h_o, \varphi_o, \theta_o)$ can be computed from (3.31). Integration with respect to incident direction (φ_i,θ_i) yields:

$$L_o(h_o, \varphi_o, \theta_o) = \int_0^{2\pi} \int_{-\pi/2}^{\pi/2} f_{\text{nearfield}} L_i \cos^2\theta_i \mathrm{d}\theta_i \mathrm{d}\varphi_i. \tag{3.37}$$

with

$$f_{\text{nearfield}}(\varphi_i, \theta_i, h_o, \varphi_o, \theta_o) = \int_{-1}^{1} \int_{-\infty}^{\infty} f_{\text{BFSDF}}(\Delta s, h_i, \varphi_i, \theta_i, h_o, \varphi_o, \theta_o)\, \mathrm{d}\Delta s \mathrm{d}h_i. \tag{3.38}$$

A practical example of a near-field scattering function for dielectric fibers is given in section 3.10.2.

3.8.2 Curve Scattering with Locally Varying Incident Lighting

Although locally constant incident lighting may be assumed in most cases of direct illumination, this situation may change in case of indirect illumination. For the sake of completeness we give the result for curve scattering with varying lighting, too. For the rendering integral one obtains:

$$\bar{L}_o(\varphi_o, \theta_o) = D \int_{-\infty}^{\infty} \int_{-1}^{1} \int_{0}^{2\pi} \int_{-\pi/2}^{\pi/2} f_{\text{varyingCSDF}} L_i \cos^2\theta_i \mathrm{d}\theta_i \mathrm{d}\varphi_i \mathrm{d}h_i \mathrm{d}\Delta s \tag{3.39}$$

with

$$f_{\text{varyingCSDF}}(\Delta s, h_i, \varphi_i, \theta_i, \varphi_o, \theta_o) = \frac{1}{2}\int_{-1}^{1} f_{\text{BFSDF}}(\Delta s, h_i, \varphi_i, \theta_i, h_o, \varphi_o, \theta_o)\,\mathrm{d}h_o. \tag{3.40}$$

3.9 Previous Fiber Scattering Models

Especially in the context of hair rendering several models for light scattering from fibers have been proposed. We now show, how they can be expressed in our notation which for instance allows systematic derivations of further scattering functions basing on the corresponding BFSDF and BCSDF. Furthermore we discuss their physical plausibility.

3.9.1 Kajiya & Kay's Model

One of the first simple approaches to render hair, which is still very commonly used, was presented by Kajiya & Kay [25]. It assumes a distant observer, since the outgoing radiance is constant over the width of a fiber and basically accounts for two scattering components: a scaled specular ad-hoc Phong reflection at the surface of the fiber, centered over the specular cone and an additional colored diffuse component. The diffuse coefficient K_{diffuse} is obtained from averaging the outgoing radiance of a diffuse BRDF over the illuminated width of the fiber, which produces significantly different results compared to the actual solution derived in section 3.10.1 (cf. Fig. 3.17). Moreover, the phenomenological Phong reflection fails to predict the correct intensities due to Fresnel reflectance (cf. section 3.10.1).

Kajiya & Kay's model can be represented by a BCSDF as follows:

$$f_{\text{BCSDF}}^{\text{Kajiya\&Kay}} = K_{\text{Phong}}\frac{\cos^n\left(\frac{\theta_o+\theta_i}{2}\right)}{\cos\theta_i} + K_{\text{diffuse}}. \tag{3.41}$$

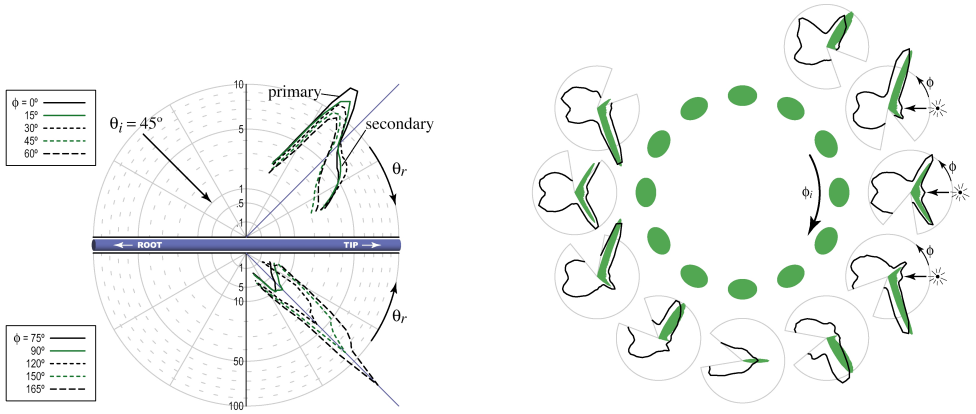

Fig. 3.10: Intensity measurements of [37]. **Left:** Keeping the light source fixed ($\theta_i = 45°$) and measuring the scattering lobes along the tangent for different relative azimuths ϕ. Note the presence of the three highlights: the primary R-highlight, the secondary TRT-highlight and the TT-highlight. **Right:** Sweeping around the specular cone while keeping the light source fixed. Due to the elliptical cross section of the fiber the glints (strong intensity peaks) depend on the orientation of the cross section.

3.9.2 The Model of Marschner et al. (2003)

A much more sophisticated far-field model for light scattering from hair fibers was proposed by Marschner et al. [37]. It bases on significant measurements (see also Fig. 3.10) of light scattering from single hair filaments and implies again a distant observer and distant light sources. In [37] it is shown that all important features of light scattering from hairs can be basically explained by scattering from cylindrical dielectric fibers made of colored glass accounting for the first three scattering components (R, TT, TRT) already introduced in section 3.6. However, the derivation of the model presented by Marschner et al. is rather awkward and omits interesting details.

In the following we will take advantage of our unified scattering formalism. The BCSDF representing the basic model of Marschner et al. (without smoothing the caustic in the TRT component) can be directly derived from its underlying

BFSDF, which is given by:

$$
\begin{aligned}
f_{\mathrm{BFSDF}}^{\mathrm{generatorMarschner}} \quad = \quad & \frac{\delta(h_o+h_i)}{\cos^2\theta_d} \\
& (g(\theta_o+\theta_i-\Delta\theta_{\mathrm{R}}, w_{\mathrm{R}}^{\theta})a^{\mathrm{R}}(\theta_d,h_i)\delta(\Delta s)\delta(\varphi_i-{\lambda_{\varphi}}^{\mathrm{R}}) \\
& +g(\theta_o+\theta_i-\Delta\theta_{\mathrm{TT}}, w_{\mathrm{TT}}^{\theta})a^{\mathrm{TT}}(\theta_d,h_i)\delta\left(\Delta s-\lambda_s^{\mathrm{TT}}\right) \\
& \delta(\varphi_i-{\lambda_{\varphi}}^{\mathrm{TT}}) \\
& +g(\theta_o+\theta_i-\Delta\theta_{\mathrm{TRT}}, w_{\mathrm{TRT}}^{\theta})a^{\mathrm{TRT}}(\theta_d,h_i)\delta(\Delta s-\lambda_s^{\mathrm{TRT}}) \\
& \delta(\varphi_i-\lambda_{\varphi}^{\mathrm{TRT}})).
\end{aligned}
\tag{3.42}
$$

This BFSDF can be seen as a generator for the basic model proposed in [37]. Note that it matches the BFSDF for a cylindric dielectric fiber with normalized Gaussians $g(x,w) := 1/(\sqrt{2\pi}w)\exp(-x/(2w^2))$ replacing the delta distributions δ_θ. This accounts for the fact that no fiber is perfectly smooth, and the light is scattered to a finite lobe around the perfect specular cone. Additional shifts $\Delta\theta_{\mathrm{R,TT,TRT}}$ account for the tiled surface structure of hair fibers, which lead to shifted specular cones compared to a perfect dielectric fiber. For a better phenomenological match in [37] it is furthermore proposed to replace θ_i with $\theta_d = (\theta_o-\theta_i)/2$. Hence this BFSDF is just a variation of (3.15) and the complex derivation of the basic model for a smooth fiber given in [37] can be reduced to the following general recipe:

- Build a BFSDF by writing the scattering geometry in terms of products of delta functions with geometry terms λ_φ and adding an additional attenuation factor.

- Derive the corresponding BCSDF according to (3.55). All ray density factors given in [37] as well as multiple scattering paths for the TRT-component are a direct consequence of the λ_φ-terms within the δ-functions.

Note that for performing the integration of $f_{\mathrm{BFSDF}}^{\mathrm{generatorMarschner}}$ in (3.55) symbolically, the following rule has to be applied:

$$I_h^G := \int_{-1}^{1} f^G(h_o)\delta(\varphi_i - \lambda_\varphi^G(h_o))\mathrm{d}h_o = \sum_{i=0}^{n-1} \frac{f^G(h_o^i)}{|\frac{\mathrm{d}\lambda_\varphi^G}{\mathrm{d}h_o}(h_o^i)|} \tag{3.43}$$

with $G \in \{\mathrm{R}, \mathrm{TT}, \mathrm{TRT}\}$. Here the expression $f^G(h_o)$ subsumes all factors depending on h_o (except the δ-function itself) and h_o^i denotes the i-th root of the expression $\varphi_i - \lambda_\varphi^G(h_o)$. For both the R and the TT component there exists always exactly one root. For the TRT component one needs a case differentiation, since it exhibits either one or three roots. This exactly matches the observation of [37] that one or three different paths for rays of the TRT component occur. Since the function $\phi(h_o) := \varphi_i - \lambda_\varphi^{TRT}(h_o)$ is smooth, the transition from one to three roots represents a fold in $\phi(h_o)$. This fold occurs when $\frac{\mathrm{d}\phi}{\mathrm{d}h_o} = \frac{\mathrm{d}\lambda_\varphi^{TRT}(h_o)}{\mathrm{d}h_o} = 0$, hence if $h_o^{1,2} = \pm\sqrt{4 - n'^2_2/3}$. However, this causes symmetric singularities of I_h^{TRT} which reflects the fact that at $h_o^{1,2}$ the ray density goes to infinity. This pair of caustics is responsible for the glints in human hair, which were already phenomenologically introduced in section 2.1.2.

Although it is basically possible to compute the roots h_o^i for all components directly, it is—for the sake of efficiency—useful to apply the approximation given by [37, equation 10].

As an example we now have a look at the direct surface reflection component (R-component). According to (3.42) one has:

$$f_{\mathrm{BFSDF}}^{\mathrm{R}} = \frac{a^{\mathrm{R}}(\theta_d, h_i)}{\cos^2\theta_d}\delta(h_o + h_i)g(\theta_o + \theta_i - \Delta\theta_{\mathrm{R}}, w_{\mathrm{R}}^\theta)\delta(\Delta s)\delta(\varphi_i - \lambda_\varphi{}^{\mathrm{R}})$$

Inserting this BFSDF into (3.55) for the corresponding BCSDF yields:

$$f_{\mathrm{BCSDF}}^{\mathrm{R}} = \frac{a^{\mathrm{R}}(\theta_d, \frac{\phi}{2})\cos(\frac{\phi}{2})g(\theta_o + \theta_i - \Delta\theta_{\mathrm{R}}, w_{\mathrm{R}}^\theta)}{4\cos^2\theta_d}. \tag{3.44}$$

This equation matches the formula given in [37, equation 8] (for $p = 0$, with $\phi =$

$M[\varphi_o - \varphi_i]$ and inserting the ray density and attenuation factors). A more detailed derivation of all scattering components is given in the appendix (App. 7.4).

In [37] the basic BCSDF is extended to account for elliptic fibers and to smooth singularities in a post processing step. Since the BCSDF is computed for a perfect smooth cylinder, there are azimuthal angles ϕ_c, for which the intensities of the TRT-components go to infinity. These singularities (caustics) are unrealistic and have to be smoothed out for real world fibers. The method used in [37] is to first remove the caustics from the scattering distribution and to replace them by Gaussians representing roughly the same portion of energy and centered over the caustics positions. Four different parameters are needed to control this caustic removal process.

Note that this rather awkward caustic handling for the TRT component performed in [37] as well as a problematic singularity in the ray density factor of the TT-component for an index of refraction approaching the limit of one can be avoided, if another BFSDF for non-smooth dielectric fibers is used, cf. section 3.10.2.

Usually hair has not a circular but has an elliptic cross section geometry. Since even mild eccentricities e especially influence the azimuthal appearance of the TRT component, this fact must not be neglected. In [37] the following simple approximation is proposed: Substitute an index n^* for the original refractive index n depending on $\varphi_h = (\varphi_i + \varphi_o)/2$ for the TRT-component as follows:

$$n^*(\varphi_h) = \frac{1}{2}\left((n_1 + n_2) + \cos(2\varphi_h)(n_1 - n_2)\right)$$

where

$$\begin{aligned} n_1 &= 2(n-1)e^2 - n + 2 \\ n_2 &= 2(n-1)e^{-2} - n + 2. \end{aligned}$$

3.10 Examples of Further Analytic Solutions and Approximations

In general it cannot be expected that for complex BFSDF/BCSDF there are analytical solutions—a situation that is similar to the one for BSSRDF/BSDF. However, in the following we derive analytical solutions or at least analytical approximations for some interesting special cases.

3.10.1 Opaque Circular Symmetric Fibers

Perfectly opaque fibers with a circular cross section like wires can be modeled by a generalized cylinder together with a BRDF characterizing its surface reflectance. For this common case we now show, how both BFSDF and BCSDF can be derived. Since no internal light transport takes place, light is only reflected from a surface patch, if it is directly illuminated. Thus the BFSDF simply writes as a product of the BRDF of the surface and two additional delta distributions limiting the reflectance to a single surface patch:

$$f_{\mathrm{BFSDF}} = f_{\mathrm{BRDF}}\delta(\xi_o - \xi_i)\delta(\Delta s) \tag{3.45}$$

or with respect to the other set of variables:

$$f_{\mathrm{BFSDF}} = f_{\mathrm{BRDF}}\delta(\phi + \arcsin h_o - \arcsin h_i)\delta(\Delta s) \tag{3.46}$$

with $\phi = M[\varphi_o - \varphi_i]$ being the relative azimuth. To derive the BCSDF the term $\delta(\phi + \arcsin h_o - \arcsin h_i)$ has to be transformed into a form suitable for integration with respect to h_i first. Applying the properties of Dirac distributions one obtains

$$f_{\mathrm{BFSDF}} = f_{\mathrm{BRDF}}|\cos(\phi + \arcsin h_o)|\delta(h_i - \sin(\phi + \arcsin h_o))\delta(\Delta s). \tag{3.47}$$

According to (3.55) for the BCSDF of a circular fiber mapped with an arbitrary BRDF the following holds:

$$\begin{aligned} f_{\mathrm{BCSDF}} &= \frac{1}{2}\int_{-1}^{1}\int_{-1}^{1}\int_{-\infty}^{\infty} f_{\mathrm{BRDF}}|\cos(\phi + \arcsin h_o)|\delta(h_i - \sin(\phi + \arcsin h_o))\delta(\Delta s) \\ &\quad \mathrm{d}\Delta s\mathrm{d}h_i\mathrm{d}h_o \\ &= \frac{1}{2}\int_{-1}^{\cos\phi} f_{\mathrm{BRDF}}\,|_{h_i=\sin(\phi+\arcsin h_o)}\,|\cos(\phi + \arcsin h_o)|\mathrm{d}h_o \end{aligned} \tag{3.48}$$

Some exemplary results are shown in figure 3.17.

Lambertian Reflectance

Many analytical BRDFs include a diffuse term accounting for Lambertian reflectance. The BCSDF approximation for such a Lambertian BRDF ($f_{\mathrm{BRDF}}^{\mathrm{Lambertian}} = k_d$) component can be directly calculated from (3.48):

$$f_{\mathrm{BCSDF}}^{\mathrm{Lambertian}} = \frac{k_d}{2} \int_{-1}^{\cos\phi} |\cos(\phi + \arcsin h_o)| \mathrm{d}h_o \tag{3.49}$$

with k_d denoting the diffuse reflectance coefficient. To solve this integral we replace the integrand by the absolute value of its Taylor series expansion about $h_o = 0$ up to an order of two:

$$f_{\mathrm{BCSDF}}^{\mathrm{Lambertian}} \approx \frac{k_d}{2} \int_{-1}^{\cos\phi} |\cos\phi - h_o \sin\phi - \frac{h_o^2 \cos\phi}{2}| \mathrm{d}h_o. \tag{3.50}$$

For the resulting approximative BCSDF, which has a relative error of less than five percent compared to the original, the following equations holds:

$$f_{\mathrm{BCSDF}}^{\mathrm{Lambertian}} \approx \frac{k_d}{2} |\frac{5}{6}\cos\phi + \cos^2\phi - \frac{1}{6}\cos^4\phi + \frac{1}{2}\sin\phi - \frac{1}{2}\sin\phi\cos^2\phi|. \tag{3.51}$$

Fresnel Reflectance

A second very important feature of opaque fibers like metal wires or coated plastics is Fresnel reflectance. We analyzed such a surface reflectance in the context of scattering from dielectric fibers in section 3.6.1 (R-component) and the corresponding BCSDF was already derived in section 3.9.2, cf.(7.36). In fact the BRDF

is averaged over the width of a fiber, the BCSDF of a fiber with a narrow normalized reflection lobe BRDF (instead of a dirac delta distribution) can be very well approximated by this BCSDF for smooth fibers. Some exemplary scenes rendered with a combination of a Lambertian and a Fresnel BRDF can be seen in Fig. 3.17. The BCSDF approximation produces very similar results compared to the precise BRDF (BFSDF) solution, but required roughly 16 times less rendering time.

3.10.2 A Practical Parametric Near-Field Shading Model for Dielectric Fibers with Elliptical Cross Section

In the following we derive a flexible and efficient near-field shading model for dielectric fibers according to section 3.8.1. This model accurately reproduces the scattering pattern for close ups but can be computed much more efficiently than particle tracing (or an equivalent) that was typically used to capture the scattering pattern correctly.

As a basis, we take the three component BFSDF given by (3.42) that was also used to derive the BCSDF corresponding to the basic model proposed in [37], cf. section 3.9.2. Due to surface roughness and inhomogeneities inside the fiber the scattering distribution gets blurred (spatial and angular blurring), cf. Fig. 3.7. In order to account for this effect we replace all δ-distributions with special normalized Gaussians $g(I,x,w) := N(I,w)\exp(-x^2/(2w^2))$ with a normalization factor of $N(I,w) := 1/\int_{-I}^{I}\exp(-x^2/(2w^2))\mathrm{d}x$. The widths w of these Gaussians control the "strength of blurriness". Furthermore, we add a diffuse component approximating higher order scattering.

With these modifications we obtain the following more general BFSDF for non-smooth dielectric fibers:

$$
\begin{aligned}
f_{\mathrm{BFSDF}}^{\mathrm{dielectric}} \quad = \quad & \frac{g(1,h_o+h_i,w_h)}{\cos^2\theta_d} \\
& (g(\frac{\pi}{2},\theta_o+\theta_i-\Delta\theta_{\mathrm{R}},w_{\mathrm{R}}^{\theta})a^{\mathrm{R}}(\theta_d,h_i) \\
& g(\infty,\Delta s,w_s)g(\pi,\varphi_i-{\lambda_{\varphi}}^{\mathrm{R}},w_{\varphi}^{\mathrm{R}}) \\
& +g(\frac{\pi}{2},\theta_o+\theta_i-\Delta\theta_{\mathrm{TT}},w_{\mathrm{TT}}^{\theta})a^{\mathrm{TT}}(\theta_d,h_i)
\end{aligned}
$$

$$
\begin{aligned}
& g\left(\infty, \Delta s - \lambda_s^{\mathrm{TT}}, w_s\right) g(\pi, \varphi_i - \lambda_\varphi{}^{\mathrm{TT}}, w_\varphi^{\mathrm{TT}}) \\
& + g(\frac{\pi}{2}, \theta_o + \theta_i - \Delta\theta_{\mathrm{TRT}}, w_{\mathrm{TRT}}^{\theta}) a^{\mathrm{TRT}}(\theta_d, h_i) \\
& g(\infty, \Delta s - \lambda_s^{\mathrm{TRT}}, w_s) g(\pi, \varphi_i - \lambda_\varphi^{\mathrm{TRT}}, w_\varphi^{\mathrm{TRT}})) \\
& + k_d \delta(\Delta s)
\end{aligned} \tag{3.52}
$$

Note that the awkward caustic handling done in [37] can be avoided by calculating the corresponding BCSDF ($f_{\mathrm{BCSDF}}^{\mathrm{dielectric}}$) out of $f_{\mathrm{BFSDF}}^{\mathrm{dielectric}}$, cf. section 3.9.2. In this case the appearance of the caustics is fully determined by the azimuthal blurring width $w_{\mathrm{TRT}}^{\varphi}$. The more narrow this width is, the closer the caustic pattern matches the one of a smooth fiber, thus the stronger the glints. All azimuthal scattering of such a BCSDF can be derived efficiently by numerical integration in a preprocessing pass. The result is a two dimensional lookup table with respect to θ_d and φ which is then used for rendering and which replaces the complex computations proposed in 3.9.2. Some exemplary comparisons between BFSDF and BCSDF-renderings are presented in Fig. 3.16.

Assuming locally constant illumination a near-field scattering function $f_{\mathrm{nearfield}}^{\mathrm{dielectric}}$ can be derived from the BFSDF by solving eqn. 3.38 in section 3.8.1 for $f_{\mathrm{BFSDF}}^{\mathrm{dielectric}}$. Assuming a narrow width w_h, i.e. a small spatial blurring, this approximately yields:

$$
\begin{aligned}
f_{\mathrm{nearfield}}^{\mathrm{dielectric}} \quad = \quad & 2k_d + \frac{1}{\cos^2\theta_d} \\
& (g(\frac{\pi}{2}, \theta_o + \theta_i - \Delta\theta_{\mathrm{R}}, w_{\mathrm{R}}^{\theta}) a^{\mathrm{R}}(\theta_d, h_o) \\
& g(\pi, \phi + 2\arcsin h_o, w_\varphi^{\mathrm{R}}) \\
& + g(\frac{\pi}{2}, \theta_o + \theta_i - \Delta\theta_{\mathrm{TT}}, w_{\mathrm{TT}}^{\theta}) a^{\mathrm{TT}}(\theta_d, h_o) \\
& g(\pi, \phi + M\left[\pi + 2\arcsin h_o - 2\arcsin\left(h_o/n'\right)\right], w_\varphi^{\mathrm{TT}}) \\
& + g(\frac{\pi}{2}, \theta_o + \theta_i - \Delta\theta_{\mathrm{TRT}}, w_{\mathrm{TRT}}^{\theta}) a^{\mathrm{TRT}}(\theta_d, h_o) \\
& g(\pi, \phi + 4\arcsin\left(h_o/n'\right) - 2\arcsin h_o, w_\varphi^{\mathrm{TRT}})).
\end{aligned} \tag{3.53}
$$

This result can be directly used for shading of fibers with a circular cross sec-

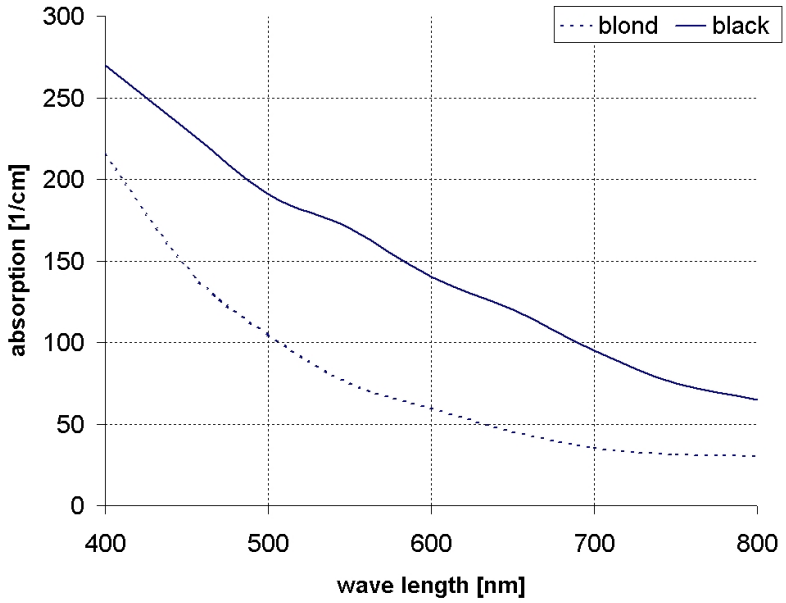

Fig. 3.11: Absorption for two different "hair colors" (blond and black) according to `http://www.solarlaser.com/doc/photoepilation\_1\_en.htm`.

tion. Although elliptic fibers could be modeled by calculating the corresponding λ_φ expressions, we propose to use the following more efficient approximation instead: Change the diameter of the primitive used for rendering—a half cylinder or a flat polygon—according to the projected diameter and apply the first order approximation for mild eccentricities proposed in [37] (cf. section 3.9.2).

Results obtained with this model are given in the results section (Fig. 3.13, 3.14, 3.15, 3.18, 3.19). Notice especially the results shown in Fig. 3.13, in which comparisons to photographs are given showing how well the scattering patterns of the renderings are matching the originals.

Interestingly, this near-field shading model is computationally less expensive than the far-field model of [37]. It can be evaluated more than twice as fast (per call) compared to an efficient reimplementation of this far-field model. Furthermore an extension of the model to all higher order scattering components is possible, since analytical expressions for corresponding geometry terms λ_φ are available.

Tab. 3.1: Summary of all parameters of the near-field shading model with plausible values for hair (see also [37],[57],Fig. 3.11)

notation	meaning	typical plausible values for human hair
$\Delta\theta_R$	longitudinal shifts of the R-lobe	-10° to -5°
$\Delta\theta_{TT}$	longitudinal shifts of the TT-lobe	$-\Delta\theta_R/2$
$\Delta\theta_{TRT}$	longitudinal shifts of the TRT-lobe	$-3\Delta\theta_R/2$
w^{θ}_R	widths for longitudinal blurring of the R-lobe	5° to 10°
w^{θ}_{TT}	widths for longitudinal blurring of the TT-lobe	w^{θ}_R
w^{θ}_{TRT}	widths for longitudinal blurring of the TRT-lobe	$2w^{\theta}_R$
w^{φ}_R	widths for azimuthal blurring of the R-lobe	0.5° to 3°
w^{φ}_R	widths for azimuthal blurring of the TT-lobe	w^{φ}_R
w^{φ}_R	widths for azimuthal blurring of the TRT-lobe	w^{φ}_R
n	index of refraction	1.55
r	strand radius	$0.0025 - 0.006cm$
σ	index of absorption in cm^{-1}	> 5
k_d	diffuse coefficient	$0.01 \cdot \exp(-3r\sigma)$
e	eccentricity	0.85 to 1

3.11 Extending the BFSDF

Although the BFSDF is a very accurate approach to describe scattering from filaments of in principle any cross section, it may be advantageous to decouple information on the cross section geometry from scattering, especially if the cross sections' convex hull strongly deviates from the perimeter (Fig. 3.12 Left). In such cases it is more likely that an overlap of minimum enclosing cylinders would introduce a substantial bias. Also the conventional parameterization might not be the best choice for analytical BFSDF models.

However, this issue can be solved by slightly modifying the original BFSDF. The idea is to parameterize all scattering with respect to the projected width of the

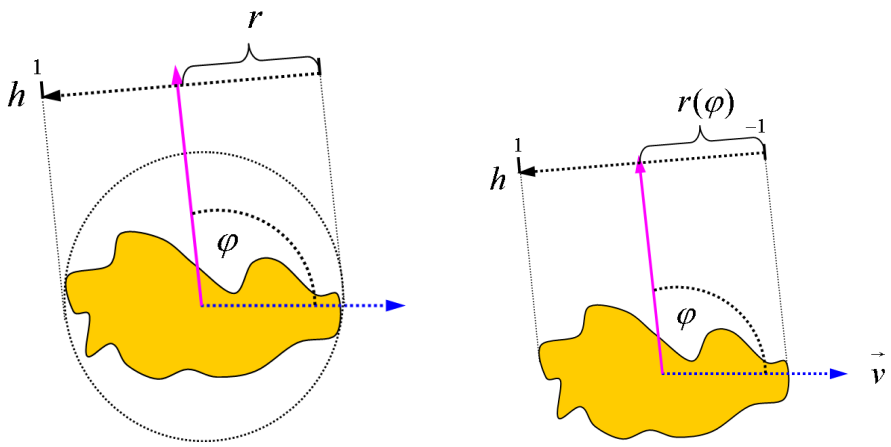

Fig. 3.12: Extending the BFSDF. **Left**: Conventional parameterization of a BFSDF at the perimeter. **Right**: A modified parameterization based on the projected width $2r(\varphi)$ of the fibers cross section. The offset h is normalized according to $r(\varphi)$.

actual cross section instead of the perimeter. For a given azimuthal angle φ this width is computed as the normal projection of the cross section with respect to φ (Fig. 3.12 Right).

Let $r(\varphi)$ denote half the projected width and assume that the offset h is now normalized accordingly. Then a modified scattering function f'_{BFSDF} may be for example defined by the following rendering integral:

$$L_o(s_o,h_o,\varphi_o,\theta_o) = \frac{1}{r(\varphi_o)} \int_{-\infty}^{+\infty}\int_{-1}^{1}\int_{0}^{2\pi}\int_{-\pi/2}^{\pi/2} r(\varphi_i) f'_{\mathrm{BFSDF}}(\Delta s,h_i,\varphi_i,\theta_i,h_o,\varphi_o,\theta_o) \cos^2\theta_i L_i(s_i,h_i,\varphi_i,\theta_i)\,\mathrm{d}\theta_i\,\mathrm{d}\varphi_i\,\mathrm{d}h_i\,\mathrm{d}\Delta s. \tag{3.54}$$

Based on this definition it is possible to derive similar far-field approximations as for the BFSDF. Assuming directional incident lighting and a distant observer one obtains the following BCSDF analogon f'_{BCSDF}:

$$f'_{\mathrm{BCSDF}}(\varphi_i,\theta_i,\varphi_o,\theta_o) = \frac{r(\varphi_i)}{2r(\varphi_o)} \int_{-1}^{1}\int_{-1}^{1}\int_{-\infty}^{\infty} f'_{\mathrm{BFSDF}}(\Delta s,h_i,\varphi_i,\theta_i,h_o,\varphi_o,\theta_o)\,\mathrm{d}\Delta s\,\mathrm{d}h_i\,\mathrm{d}h_o.$$

(3.55)

Note that for rendering one has to account for the projected widths which may depend on φ_i and φ_o. For a conventional BFSDF/BCSDF it was enough to know the diameter of the minimum enclosing cylinder.

3.12 Conclusion

In this chapter we derived a novel theoretical framework for efficiently computing light scattering from filaments. In contrast to previous approaches developed in the realm of hair rendering it is much more flexible and can handle many types of filaments and fibers like hair, fur, ropes and wires. Approximations for different levels of abstraction can be derived in a straight forward way. Furthermore, our approach provides a firm basis for comparisons and classifications of filaments with respect to their scattering properties. The basic idea was to adopt basic radiometric concepts like BSSRDF and BSDF to the realm of fiber rendering. Although the resulting radiance transfer functions are strictly speaking valid for infinite fibers only, they can be seen as suitable local approximations.

However, the theoretical analysis given in this thesis should be seen as a starting point and further work is required to investigate practical issues which arise in the case of "real world filaments". Moreover, efficient compression strategies are needed to reduce the memory costs for storing Bidirectional Fiber Scattering Distribution Functions. Also, if the BFSDF is given in a purely numerical form, the four dimensional rendering integral itself is very costly to evaluate. Therefore, the BFSDF should be approximated by series of analytical functions which can be efficiently integrated. Fortunately, many scattering distributions have very few intensity peaks which can be well approximated with existing compression schemes (e.g. Lafortune Lobes [11], Reflectance Field Polynomials [42], Linear Basis Decomposition [38], clustering and factorization [26, 33, 49]) developed in the realm of BRDF and BTF rendering.

In this chapter several aspects of light scattering from a single fiber were analyzed. However, also inter-reflections between fibers (multiple fiber scattering)

play an important role for the overall color. In the next chapter this issue will be discussed in detail. It will be shown that the BFSDF is the key to efficient physically based global illumination of fiber assemblies.

3.13 Results

Fig. 3.13: An oval made of rough plastic illuminated by one point light source. The upper row shows photographs and the second row renderings with a variant of the model presented in section 3.10.2. The parameters are set to roughly match the original photographs. Note the similarity of both positions and intensities of the highlights for different viewing angles. It took less than five seconds to render each frame with conventional ray tracing.

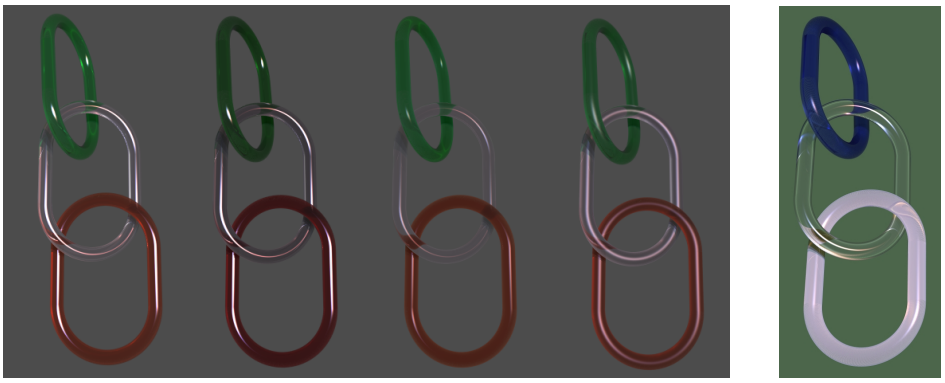

Fig. 3.14: Various BFSDF examples with a more complex illumination.

Fig. 3.15: Two different close-ups of hair rendered with a *mental ray*® implementation (cf. `http://www.mentalimages.com`) of the near-field model presented in section 3.10.2.

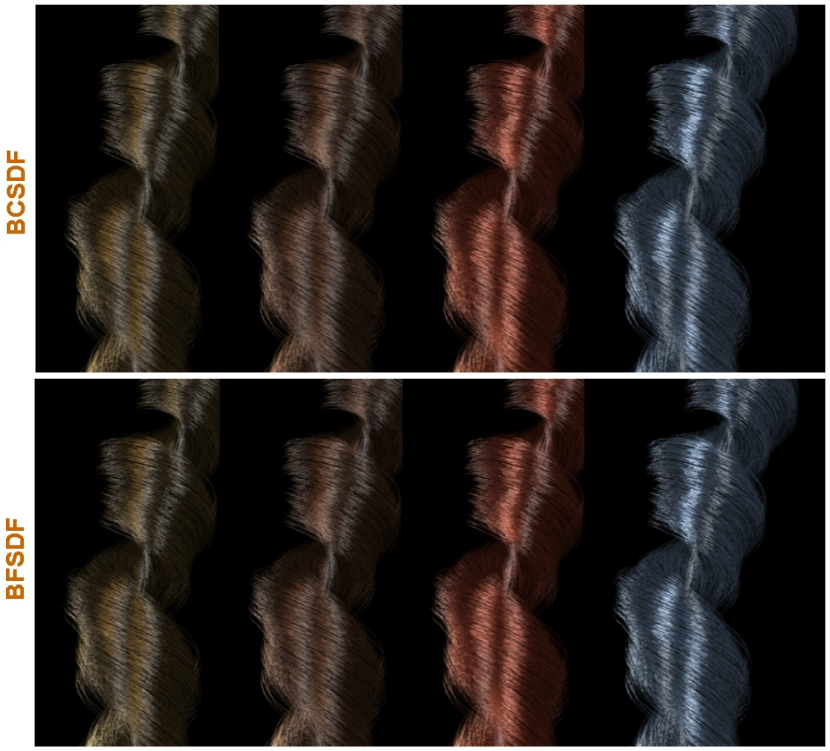

Fig. 3.16: Different strands of translucent dielectric fibers illuminated by three distant point light sources. The left two leftmost images were rendered with a hair like material and the two rightmost images show synthetic fibers. Direct illumination was computed according to section 3.10.2. The BCSDF was computed from the BFSDF for dielectric fibers (cf. section 3.10.2). Please note how well the BCSDF approximations match the original BFSDF renderings.

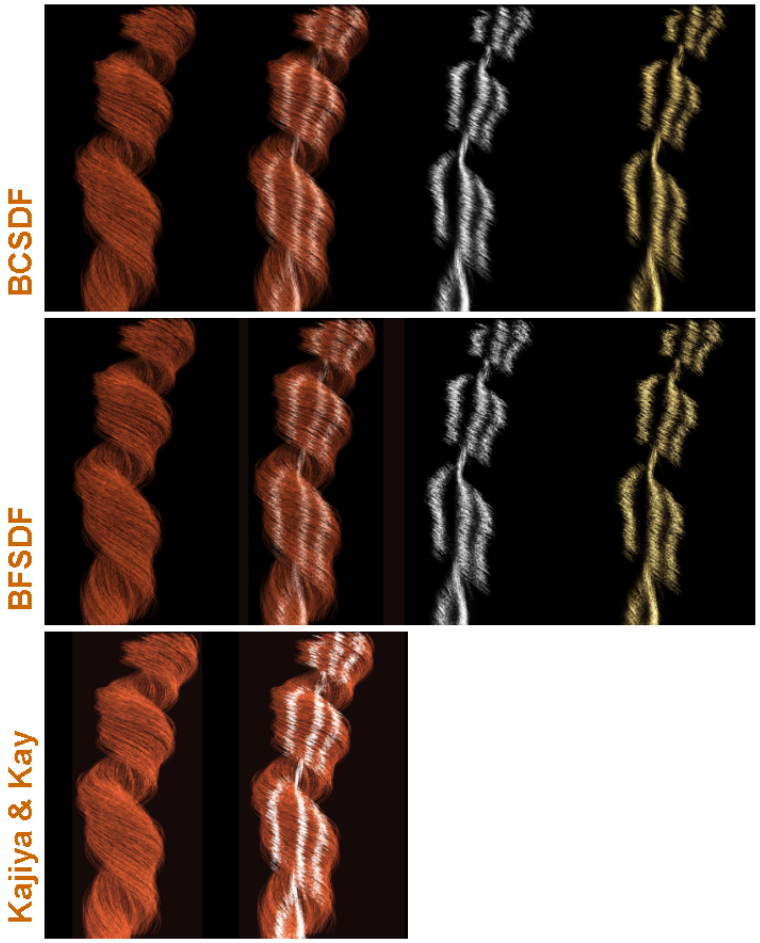

Fig. 3.17: **Top row:** Various physically based (i.e. energy conserving) BCSDF renderings of opaque fibers illuminated by three distant point light sources. The BCSDFs were generated according to from the following BRDF types: Lambertian (*left*); Fresnel $+ (1 -$ Fresnel$) \times$ Lambertian (*left middle*); Fresnel for aluminium (*right middle*); Fresnel for gold (*right*). These BCSDF examples are given in a purely analytical form, so that parameters—like index of refraction—can be easily changed on the fly, e.g. for the "gold" and "aluminium" examples, which use the same BCSDF with different material properties. **Middle row:** BFSDF renderings of the same scenes. Notice how well the BCSDF renderings match the BFSDF originals. **Bottom row:** Some exemplary renderings with the phenomenological model of Kajiya & Kay. Lighting and geometry was not changed. The diffuse component was computed according to from the diffuse coefficient of the BRDF. The width of the specular lobe (if present) as well the peak intensity was set to match the ones of the original physically based renderings setting the Fresnel factor to one. Nevertheless, the results differ substantially from the BCSDF resp. BFSDF renderings. Note that the BCSDF images were computed approximately one order of magnitude faster, since $16\times$ less eye-rays per pixel were needed to achieve a similar rendering quality.

Fig. 3.18: BFSDF renderings (based on the model presented in section 3.10.2) of a hair style consisting of about 90000 individual hair fibers (left: brown; middle: blond; right: dark red dyed) illuminated by five point light sources. The images were rendered in about 15 hours each with Monte Carlo path tracing (see section 4.7).

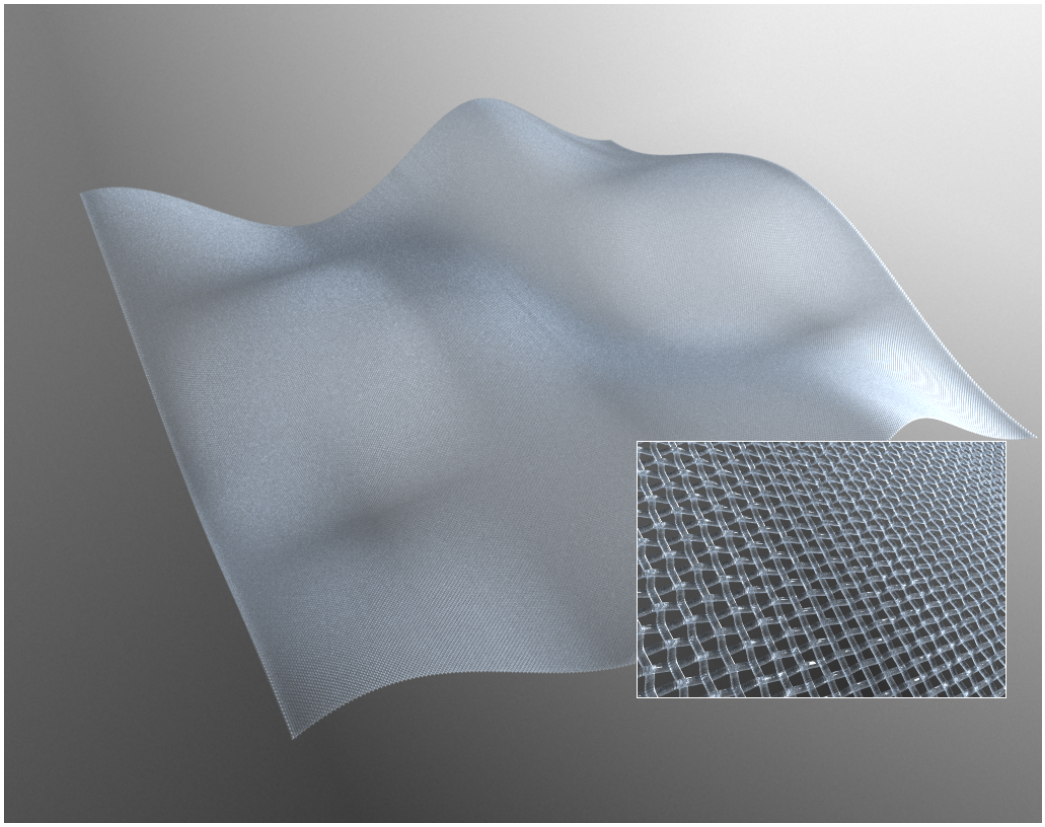

Fig. 3.19: BFSDF rendering of a fabric made of dielectric fibers using the model presented in section 3.10.2. It took eight hours to render the image with Monte Carlo path tracing (see section 4.7).

4. RENDERING OF FIBER ASSEMBLIES

4.1 Introduction

Rendering of fiber based geometries—especially of human hair—is a major challenge. Even after the geometries of thousands to hundreds of thousands of fibers are determined the scattering of light must be simulated to obtain realistic results. However, in this context not only single scattering is important but also the effects of indirect illumination due to multiple fiber scattering are essential for the overall hair color. An example illustrating the importance of multiple fiber scattering is shown in Fig.4.1. Unfortunately, accurately solving the global illumination problem requires costly rendering techniques. In addition to the challenge of physically accurate hair rendering, also efficiency is crucial. For this purpose several simplistic models have been developed in the last decade accounting for some phenomenological effects, such as self shadowing, but failing at other important issues such as multiple fiber scattering [7, 66, 15, 40, 28, 34]. In general, these approaches are not scalable for higher accuracy even by trading some of performance.

In the previous chapter light scattering from a single filament was discussed. Based on a novel frame work — the Bidirectional Fiber Scattering Distribution Function (BFSDF) — several approximations were proposed. Moreover, for the frequent case of distant light sources and a distant observer a far-field scattering model — the Bidirectional Curve Scattering Distribution Function (BCSDF) — was derived. Now that a general description for scattering from a single filament was derived, its application to rendering fiber assemblies will be discussed. However, before presenting our approaches for fiber rendering, we will address a more practical issue, the geometrical representation of fibers.

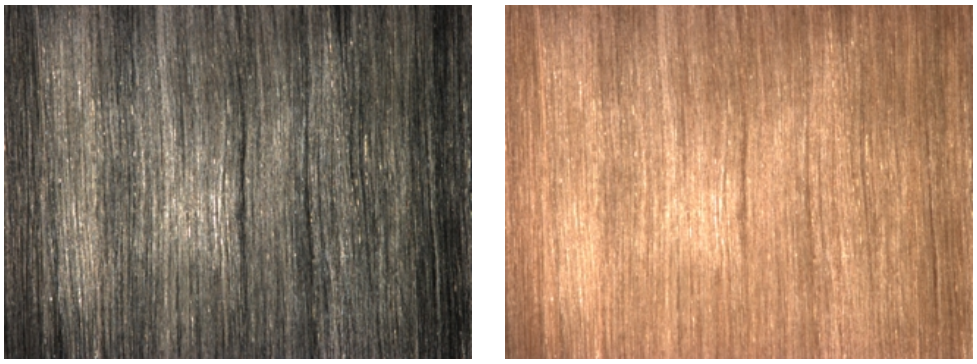

Fig. 4.1: The importance of multiple fiber scattering. Measurements of blond hair using the method of [45] (images from `http://www1.cs.columbia.edu/CAVE/projects/separation/separation_gallery.php`) **Left:** direct illumination, **Right:** direct and indirect illumination (mostly due to multiple fiber scattering). For this example multiple fiber scattering contributes much more intensity to the overall scattering distribution than direct illumination.

4.2 Geometrical Representation of a Fiber

There are several ways to represent a fiber for rendering. The minimum enclosing cylinder could be basically modeled by a generalized cylinder, a circular cross section swept along a 3d-curve [46]. However, such a representation is quite costly and requires a rather complex rendering pipeline. A much simpler approach is to model a fiber by a chain of straight, oriented segments (Fig. 4.2 Left). Note that such an implementation implies that the curvature of a fiber is small compared to its diameter. Otherwise it is very likely that annoying discontinuities occur (Fig. 4.2 Right).

For BFSDF/BCSDF based renderings we propose to approximate a fiber by segments exhibiting the same cross section as the local minimum enclosing cylinder. Since all internal scattering is already captured by the BFSDF/BCSDF there is no need to model the original shape of the fiber. Instead, half cylinders dynamically oriented with respect to a desired direction ω (e.g. the direction of an eye ray) are used (Fig. 4.3 Left). Another (slightly less accurate) alternative would be flat ribbons dynamically aligned to a given direction (Fig. 4.3 Right). Note that for the extended BFSDF concept—which was introduced in section 3.11—the

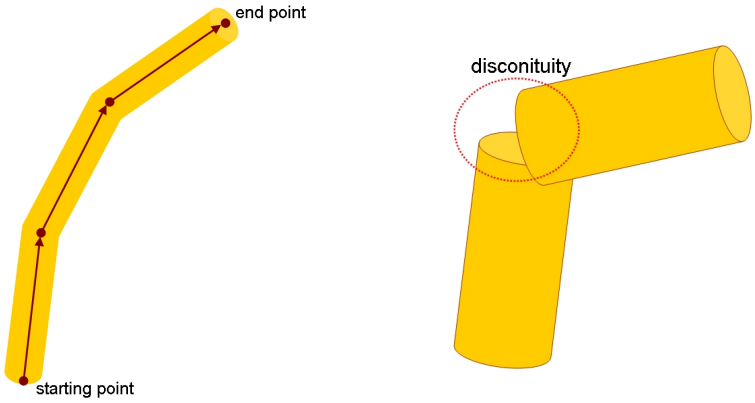

Fig. 4.2: **Left:** Representing a fiber by a chain of oriented segments. **Right:** A big curvature introduces discontinuities between segments.

cross section explicitly depends on the azimuthal angle φ_i for an incident or φ_o for an exitant direction. Hence, if using this scattering model, the cross section of a primitive has to be adapted dynamically to the projected width $2r(\varphi_i)$ or $2r(\varphi_o)$, respectively.

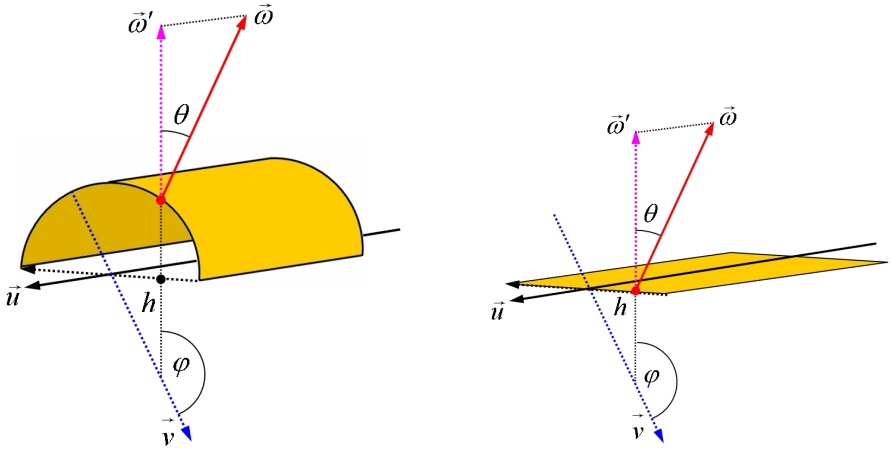

Fig. 4.3: Geometrical representation of a fiber segment. The ray direction is indicated by $\vec{\omega}$. **Left**: Half cylinder **Right**: Flat ribbon.

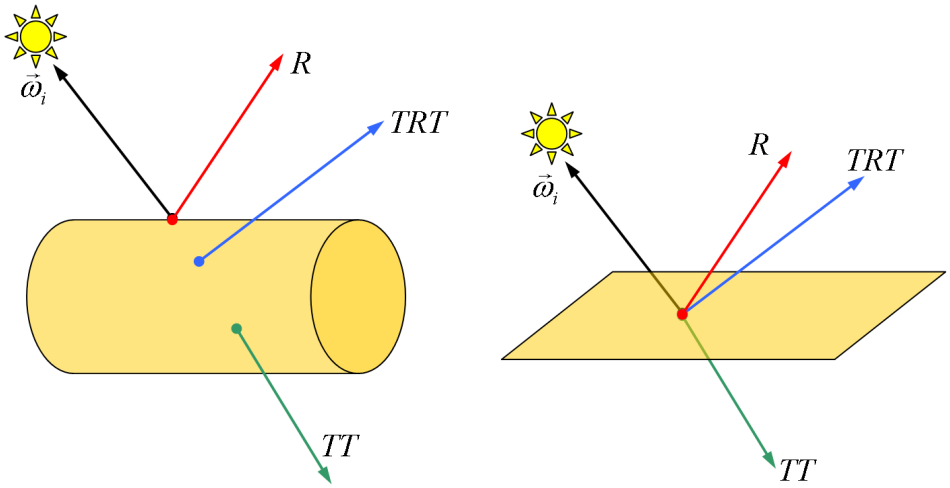

Fig. 4.4: A simple example of a spatial varying BSDF approximation for a BFSDF. **Left:** BFSDF snapshot of a perfect dielectric cylinder (R,TT,TRT). **Right:** Concentrating this BFSDF to the incident position gives a spatial varying BSDF.

4.3 BFSDF and BCSDF Rendering

The key to BFSDF and BCSDF rendering was already given in chapter 3 by the corresponding scattering integrals (7.24) and (3.36). Based on these equations the exitant radiance at the minimum enclosing cylinder can be computed with respect to incident illumination. Using the geometrical representation proposed in the previous section the rendering integrals can be basically solved with standard techniques such as Monte Carlo path tracing. However, since such an unbiased approach can lead to very long rendering times an efficient implementation is crucial.

4.3.1 Towards Efficient BFSDF and BCSDF Rendering

In the following, a BSDF approximation of the BFSDF is derived allowing an efficient rendering of fiber assemblies using conventional rendering systems which have no facility to handle Bidirectional Fiber Scattering Distribution Functions. Moreover, it is shown that a BCSDF can be directly transformed to a BSDF.

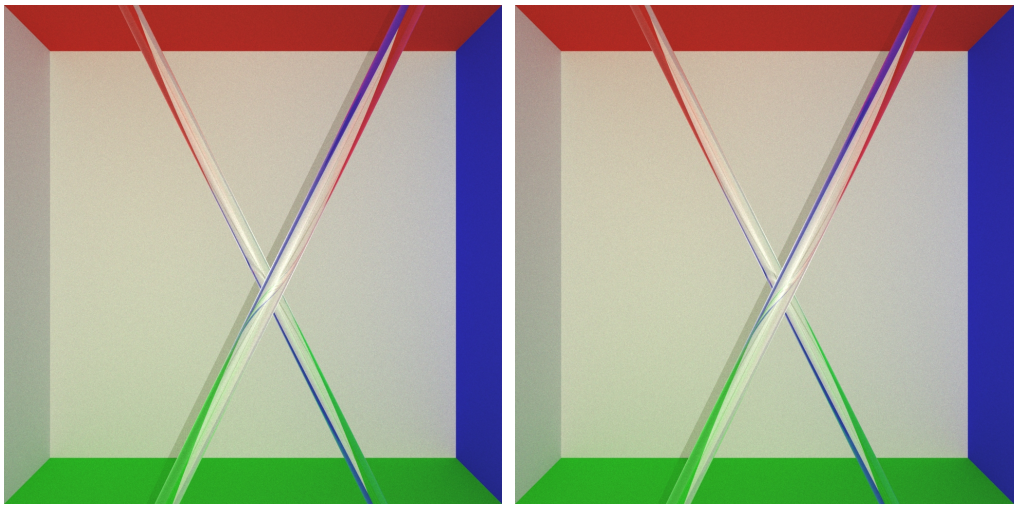

Fig. 4.5: Comparison: a spatial varying BSDF approximation of the BFSDF vs. a true BFSDF. The renderings show two perfect smooth cylinders in a Cornell box, illuminated by one point light source from the camera position. **Left:** Rendering using a true BFSDF for two perfect smooth dielectric cylinder (see also Fig.4.4 Left), **Right:** a BSDF approximation according to Fig.4.4 Right. Note the similarity of both results. Only minor differences are visible in the refraction patterns.

BSDF Approximation of the BFSDF

For many kinds of fibers internal light transport is limited to a small region around the incident position. Furthermore, the diameter of a typical fiber is very small compared to other dimensions of a scene. Hence—intuitively speaking—"concentrating" the BFSDF to the infinitesimal surface patch in which incident light penetrates the fiber while keeping the original angular scattering distribution (see Fig. 4.4 and Fig. 4.5), introduces only local bias with generally little global impact. This idea may be formalized by integrating an BFSDF with respect Δs and ξ_o:

$$f_{\mathrm{BSDF}}[h_i](\varphi_i,\theta_i,\varphi_o,\theta_o) := \int_{-\infty}^{\infty}\int_{0}^{2\pi} f_{\mathrm{BFSDF}}\mathrm{d}\xi_o\mathrm{d}\Delta s \tag{4.1}$$

The result is a special anisotropic, spatial varying BSDF $f_{\mathrm{BSDF}}[h_i](\varphi_i,\theta_i,\varphi_o,\theta_o)$

varying over the width of the fiber. Assuming that the underlying BFSDF is Helmholtz reciprocal (cf. section 3.5) the following equality holds:

$$f_{\mathrm{BSDF}}[h_o](\varphi_o, \theta_o, \varphi_i, \theta_i) = f_{\mathrm{BSDF}}[h_i](\varphi_i, \theta_i, \varphi_o, \theta_o). \tag{4.2}$$

Then the total exitant radiance with respect to an incident radiance distribution L_i can be estimated by evaluating the scattering integral:

$$L_o(h_o, \varphi_o, \theta_o) = \int_0^{2\pi} \int_{-\pi/2}^{\pi/2} f_{\mathrm{BSDF}}[h_o](\varphi_i, \theta_i, \varphi_o, \theta_o) L_i(\varphi_i, \theta_i) \cos^2\theta_i \mathrm{d}\theta_i \mathrm{d}\varphi_i. \tag{4.3}$$

Using this approximation a fiber can be modeled very well according to section section 4.2 by a primitive having the same effective cross section as the fiber.

Transforming a BCSDF to a BSDF

Transforming a BCSDF to an anisotropic BSDF is trivial, in fact virtually nothing has to be changed if the scattering integral is evaluated according to (3.55) . Only the diameter of the minimum enclosing cylinder has to be neglected if the fibers are modeled by primitives geometrically accounting for their effective cross sections.

4.4 Local and Global Illumination

In computer graphics one often distinguishes between two different classes of illumination models: Local and global illumination models. Local approaches account only for local information at a point in space (e.g. on an object) to determine illumination. However, because solutions to the rendering equation require global knowledge of a scene, a local solution omits information. In contrast a global illumination approach accounts for all possible light paths contributing to illumination.

Adding shadowing another pair of illumination models can be considered: Direct and indirect illumination. In this context direct illumination means light arriving directly from a light source, without being scattered from intermediate objects whereas indirect illumination denotes light approaching a point after scattering (e.g. inter reflections). There are a couple of reasons why such a distinction makes sense. First of all there are usually only a few light emitters in a scene which allows for an extremely efficient light sampling. Second, direct illumination is often by far more important than global (indirect) illumination, since multiple scattering (like inter-reflections) tends to decrease the radiance along a light path. Finally, indirect illumination usually has much less high frequency detail than direct illumination or exhibits other structural differences. As we will see, in particular the latter assumption allows for an efficient approximation of the global illumination for fiber assemblies.

Assuming that an incident radiance distribution L_i can be separated into a direct component L_i^{direct} and an indirect component $L_i^{indirect}$ with $L_i = L_i^{direct} + L_i^{indirect}$, any arbitrary scattering integral S can be separated into two independent parts. Since S is linear with respect to incident radiance it can be split into a sum of two integrals which can be evaluated independently:

$$S(L_i) = S(L_i^{direct}) + S(L_i^{indirect}). \tag{4.4}$$

4.5 Global Illumination for Fiber Assemblies

For fiber based geometry indirect illumination due to multiple fiber scattering has a substantial impact on the overall color. In particular for fibers with only little absorption (like blond hair) multiple fiber scattering must not be neglected. Moreover, scattering from individual fibers is often highly anisotropic which means that a directional incident radiance field tends to stay directional after scattering.

Traditional unbiased rendering techniques, such as path tracing [24] or particle tracing [5, 35], were previously applied only to surfaces and participating media. However, although existing Monte Carlo techniques for volumetric scattering in participating media [8] can cope with anisotropic, spatially varying phase

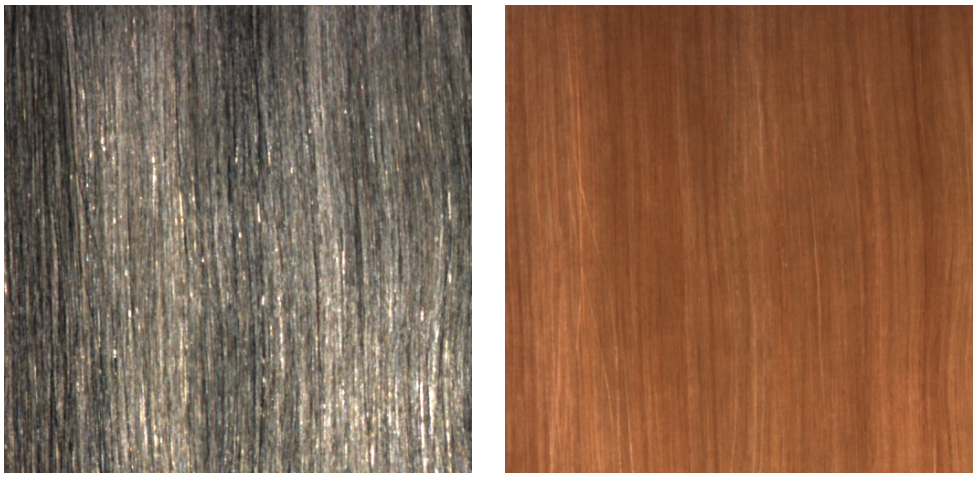

Fig. 4.6: Measurements of blond hair using the method of [45] (images from `http://www1.cs.columbia.edu/CAVE/projects/separation/separation_gallery.php`) **Left:** single scattering, **Right:** multiple fiber scattering. Note the smooth and even scattering distribution of multiple fiber scattering and the sharp azimuthal details of single scattering.

functions, an adequate volumetric representation of a fiber cluster is not known a priori. On the other hand, traditional surface based approaches imply that all fibers are explicitly modeled by geometry. Even though we used a standard Monte Carlo particle tracing approach for accurate scattering simulations (see section 4.6) such an explicit representation is too expensive for rendering of fiber assemblies.

However, although multiple fiber scattering is a very complex phenomenon it typically produces a smooth, quite predictable scattering distribution (see Fig. 4.6). As we will see this invites more efficient approaches to approximate global illumination in hair and similar geometry.

4.5.1 Related Work

Rendering of hair or other fiber based geometry is always a trade-off between physical accuracy and computational efficiency. In particular global illumination is an issue. Over the last years several simplistic approaches have been proposed to account for some global illumination effects such as self shadowing [7, 66, 16, 15, 30, 40, 28, 34]. All these ad-hoc approaches may give plausible images in some

situations but provide no general physically-based solution and fail to simulate the correct appearance of hair. Moreover, the highly anisotropic nature of scattering is completely neglected. In general there is no possibility to scale these approaches towards higher accuracy by trading some of performance.

An interesting projection based technique to approximate global illumination for fiber based geometries was presented by Yuksel [68]. However, the approach makes some simplifications, e.g. it is neglecting inter-reflections due to backward scattering, which makes it less accurate. Moreover, it is assumed that a hair can be approximated by a translucent curve. But unfortunately neither a hint is given, how the effective translucency can be computed from the scattering function of a fiber, nor the general limitations of such a transparency model are discussed.

A more complex scattering based approach for self shadowing suitable for interactive rendering was presented in [15]. But neither the Rayleigh phase function used to describe the anisotropy of scattering nor the simplistic density based approach for attenuation are adequate to render hair photo-realistically. Rayleigh scattering implies that the cross section of the scatterer is much smaller than the wave length of the visible spectrum (400 nm – 800 nm), which is not satisfied for human hair (diameter: 70000 nm – 100000 nm). In addition, multiple fiber scattering in hair is highly anisotropic with respect to the fibers' tangent. Hence, with a purely density based approach as is proposed in [15] several important phenomenological aspects cannot be handled correctly.

Photon mapping is a very general, powerful approach to approximately solve global illumination problems for surfaces and participating media [18, 22, 19]. However, all existing variants are not practicable for hair rendering. In a volumetric representation of hair, both the density and the phase function depend on position and direction, and neither is known a priori. On the other hand, the fractal meso-structure of fiber assemblies disallows conventional surface-based representations. These fundamental differences prevent these and other traditional rendering techniques from being directly applied to hair.

Recently, a novel photon map based approach for hair rendering was presented by Moon and Marschner [43]. In [43] samples of a photon map are used to estimate multiple fiber scattering. After a particle tracing pass —very similar to conventional photon mapping— light paths are sampled by "photon particles" which

are then stored in a 6D-photon map with respect to their position in space and the orientation of the corresponding path segment. The outgoing radiance due to multiple fiber scattering is computed by estimating the incoming radiance for a set of incident directions. These directions are computed according to the model presented in [37]. Although it shares some concepts with the novel approach presented in section 4.8 it differs not only on a technical level. For a more detailed comparison to our approach we refer to section 4.9.8.

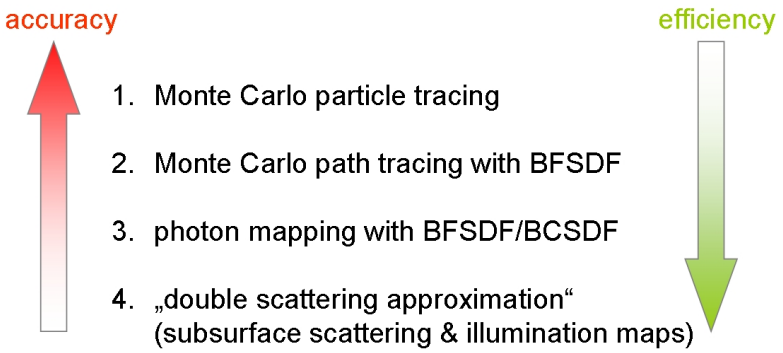

Fig. 4.7: Selected methods for fiber rendering ordered with respect to accuracy and computational efficiency.

4.5.2 Overview

Rendering fiber assemblies such as hair is always a compromise between physical accuracy and computational efficiency. However, for many applications aggressive physically-based simplifications do a rather good job. Throughout our studies several novel and existing rendering methods were implemented and tested in the context of fiber rendering. In the next sections we will focuss on the following approaches (Fig. 4.7):

- pure Monte Carlo particle tracing for extremely accurate renderings and scattering analysis,
- BFSDF Monte Carlo path tracing for accurate reference solutions,
- a novel ray-based approach for accurate but efficient rendering of fibers and

- an extremely efficient “double scattering” approximation which is suitable to be implemented on current graphics hardware.

The first two methods base on standard Monte Carlo rendering methods, whereas both the ray-based approach and the “double scattering” approximation include novel techniques. Therefore, only the two latter approaches will be described in more detail.

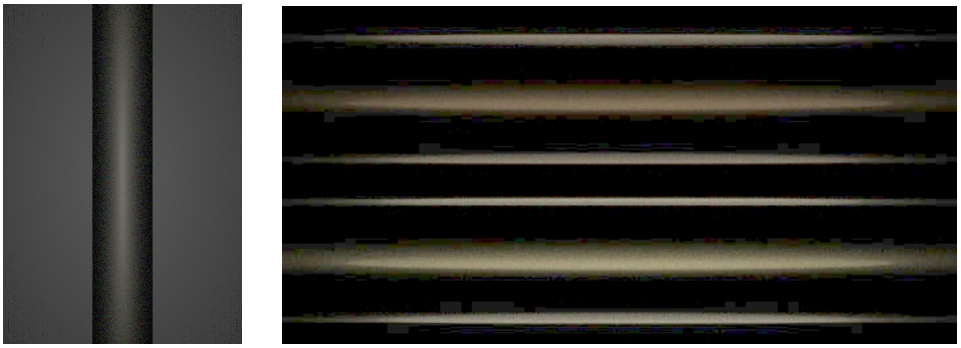

Fig. 4.8: Results obtained with Monte Carlo particle tracing using a virtual camera model. **Left:** A single dielectric fiber (without any absorption) in front of an area light source. **Right:** Two dielectric hair fibers illuminated by a point light source (from back). The top strand has absorption coefficients matching brown, the bottom matching blond hair.

4.6 Monte Carlo Particle Tracing

Particle tracing is a well established and very flexible method for scattering simulations [5, 35]. By tracing light paths using particles the distribution of illumination in a scene can be estimated. We implemented a particle tracing based framework to analyze scattering from fibers and to generate Bidirectional Fiber Scattering Distribution Functions through virtual experiments. In this context the shape of a fiber was modeled geometrically and the optical properties were set to match a desired material. Some examples rendered with this approach are given in Fig. 4.8, 3.7. Note that particle tracing was used also for analyzing scattering from wet hair (section 2.1.3). However, although this approach can produce extremely

accurate results it is not suited to be used for rendering large fiber assemblies, since this would require unacceptable long rendering times to obtain convincing results.

4.7 BFSDF Monte Carlo Path tracing

Monte Carlo path tracing is an unbiased technique which uses Monte Carlo integration to solve the rendering equation [24]. This method can also be applied to the field of fiber rendering for solving the BFSDF scattering integral (3.8). Unfortunately, it suffers from substantial rendering times. Since the convergence rate of the basic algorithm is quite slow, estimates tend to exhibit substantial variance, causing noise. Therefore it is not the algorithm of choice if rendering speed is crucial. However, due to its accuracy we used this technique for rendering reference solutions.

Our implementation bases on the BFSDF approximation presented in section 4.3.1 which converts a BFSDF to a spatially varying BSDF. Moreover, the scattering is split similar to (4.4), separating the contributions of direct and indirect illumination.

In contrast to (4.4) different scattering integrals were used for the two components. Assuming that the far-field assumptions (cf. section 3.7) hold for direct illumination the BCSDF scattering integral (3.36) was solved for the direct component, whereas for indirect illumination the BSDF was evaluated according to (4.3).

Hence, no implicit far-field assumption is made and no constant directional lighting across the width of a fiber is assumed for indirect illumination. Both integrals are evaluated using Monte Carlo Integration. In conjunction with Russian roulette and importance sampling we obtained physically accurate results in a reasonable time frame. Some results obtained with the method are shown in Fig. 3.18, Fig. 3.19 and section 4.12.

4.8 Efficient Ray-Based Global Illumination

In the following we present a novel technique to efficiently render global illumination for complex geometry. Based on this general approach, its application to fiber rendering will be discussed in section 4.9.

4.8.1 Introduction and Related Work

Photon mapping [18] is a very efficient and flexible technique to approximate indirect illumination effects for complex scenes. In the following it will be denoted as conventional photon mapping. Conventional photon mapping can be seen as a two stage process:

- a particle tracing pass and
- a density estimation (rendering) phase

During particle tracing the state of a particle—i.e. its position and energy—is stored in a so called photon map, if it interacts with a surface. In the rendering phase the light flux due to indirect illumination at a point (on a surface) is estimated from neighboring samples within a certain maximum lookup sphere of radius R from this map. The flux estimation is based on the assumption that all these neighboring samples are from the same, locally flat surface. Note that this assumption may be problematic for scenes with very detailed geometry like in case of tree leaves, grass or hair. In this case the lookup region has to be chosen very small to avoid substantial estimation bias. On the other hand, a very small lookup radius implies a huge number photon particles, to keep the variance low.

Another problematic example is a small object surrounded by a big box of high reflectance. Suppose the exitant radiance of the object has to be estimated. Since photons are stored only along the shape of an object it is very likely that substantial boundary bias occurs, since the radiance at the edges is systematically underestimated (darkening at the edges) (see Fig. 4.9). Moreover—due to its small extent—only relatively few photons are generated in the proximity of the object potentially making the radiance estimate less accurate.

Several technique have been proposed to decrease rendering bias [31, 17, 58, 59, 20, 21, 32, 51]. Good results were obtained by extending the photon mapping approach to allow flux estimation not only on flat surfaces but at points in space (which is also related to volume photon maps [22]). In the following we will focus on this extension. The key idea is to estimate the incident flux from neighboring photon paths (ray segments) rather than from neighboring photon impacts on surfaces. Lastra et al. primarily introduced this concept in the context of photon mapping. Here the incident flux at any point on a surface is estimated by density estimation, by accounting for all rays intersecting a disc in the local tangent plane centered at this location. To find the closest rays with respect to that disc an indexing structure called ray cache was proposed. Although this approach successfully reduced boundary bias, rendering times increased by roughly two orders of magnitude compared to conventional photon mapping.

Recently Havran et al. [17] presented a much more efficient data structure for representing light transport called *ray maps*. Ray maps are basically an efficient KD-tree based indexing structure: The space is subdivided by KD-voxels which hold references to all ray segments intersecting a voxel. The incident irradiance is estimated from neighboring rays through density estimation. To identify convenient neighboring rays, novel distance metrics have been proposed by Havran et al. which significantly reduced boundary and topological bias.

Even though ray maps are clearly superior to the ray cache, Havran et al. reported rendering times being up to five times longer than for conventional photon mapping. Although strategies to reduce the memory usage and computation times are proposed ray maps can be still very costly:

- Ray mapping needs to store references to rays everywhere along a ray, potentially even in empty space. This increases the memory requirements since many references are stored which will never be used for a radiance estimate (Fig. 4.10 Right).

- If the lookup radius R is much bigger than the extend of a KD-Voxel many references to a single ray may be found in a closest neighbor lookup. This very common situation leads to a significant overhead (Fig. 4.10 Left).

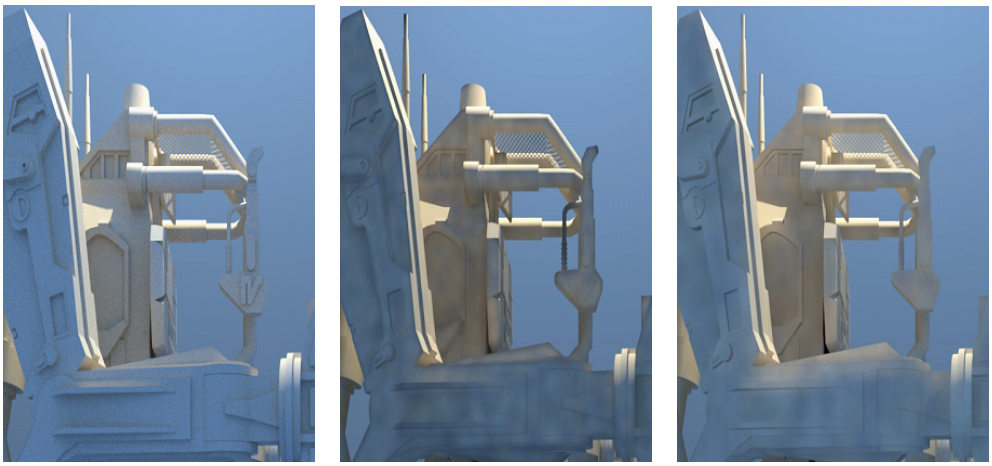

Fig. 4.9: A robot in a big, bluish box (four times the extent of the robot). Global illumination was computed with: **Left:** path tracing (reference), **Middle:** a direct visualization of the density estimation based on conventional photon mapping, **Right:** a direct visualization of the density estimation based on a ray map (Ray-based global illumination). Note the strong systematical boundary bias (underestimation at the edges) in the photon mapping rendering.

Moreover the resolution of ray maps is fully determined by the ray density, only limited by some user defined maximum KD-tree depth. Thus there is no possibility to locally adapt its resolution according to the geometry of a scene.

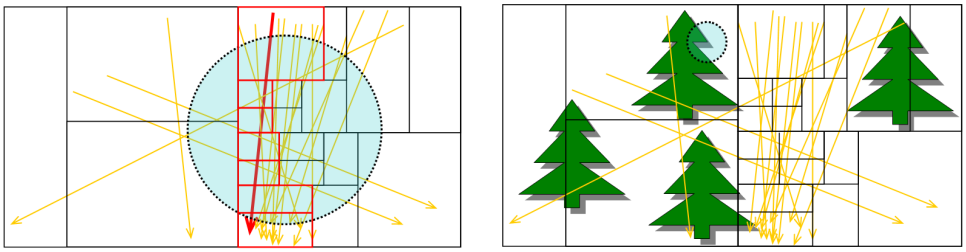

Fig. 4.10: Potential issues of ray mapping [17]. The spatial subdivision scheme of the ray map (KD-tree) is illustrated by black rectangles, the ray segments are indicated by yellow lines and the lookup region by a greenish disc. **Left:** Several redundant references are found in the lookup volume. **Right:** Useless references which will never be used for radiance estimation are stored.

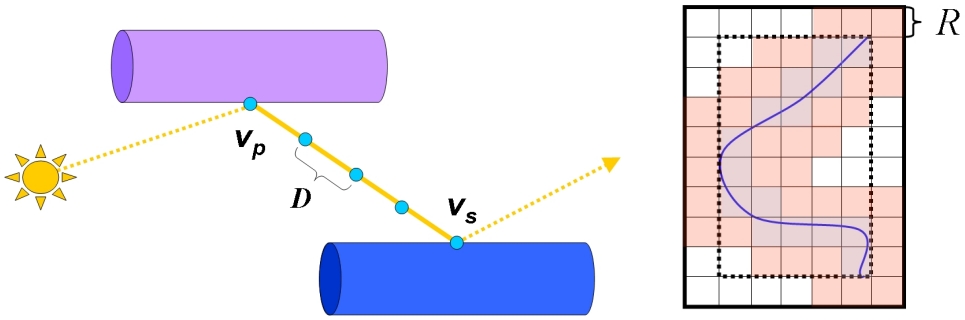

Fig. 4.11: **Left**: Sampling a light path. **Right**: Identifying relevant regions, for which references have to be stored. Based on the bounding box (dashed line) of a geometry (in this case a single fiber indicated blue line) a uniform grid is constructed (black solid line). If a voxel is intersected by visible geometry or if it has neighboring voxels intersected by visible geometry it is dyed red. References have to be stored only, if they are contained in a red colored voxel.

4.8.2 Overview

The goal of our approach is to combine the simplicity and efficiency of photon mapping with the bias reduction of the existing ray based techniques. References to rays should be adaptively distributed with respect to the geometry in the scene avoiding unnecessary references in empty space and allowing a user defined trade-off between accuracy and efficiency.

In contrast to conventional photon mapping, where radiance estimation only accounts for photons on surfaces, ray based density estimation will need to look up for the K closest ray segments (light path between two surface interactions) with respect to a given position in space. To efficiently find close rays a single ray segment is represented by several photons (particle references) in a photon map. If one of these photons is found in a nearest neighbor search, the light path is intersecting the lookup sphere. Suppose a ray segment (representing indirect illumination) with a starting position v_p and ending at another point v_s is given. Then particle (photon) references to a ray starting at v_p and being equally distributed along the ray by a certain distance D are created and stored in a photon map (cf. Fig. 4.11 Left). The main advantage of storing photons referencing a ray (over storing references to rays in ray maps) is that photon densities can be adapted to a scene, whereas for ray mapping the resolution of the ray maps is determined by the local ray density. For example no references need to be stored in empty space. Note that photon references use much less memory than conventional photons (in our implementation 8 bytes per photon). However, to enhance efficiency a photon is only stored in the map if it will be potentially contribute in a radiance estimate. This is achieved by using a binary grid to identify empty regions. If a voxel of this grid is intersected by an object it is marked as occupied and empty otherwise. The spatial resolution of a voxel is chosen to be equal to the maximum lookup radius R. Photon references are stored only in the map, if the voxel which encloses the photon is occupied or has at least one non empty neighboring voxel (cf. Fig. 4.11 Right).

In the following several aspects of the algorithm will be discussed. Since it is closely related to conventional photon mapping, only differences are described in more detail.

4.8.3 Building a Photon Map

Based on a parameter α, the density of photons referencing a ray segment is adapted to the maximum lookup radius R: $D = \alpha R$. For $\alpha \approx 1$ this simple approach successfully reduces redundant references to ray segments (Fig.4.9). On the other hand, α also controls the accuracy of sampling. For a detailed discussion of the sampling error we refer to section 4.8.5.
The basic data structure of the algorithm are photon references to ray segments, which consist of

- a reference to the corresponding ray segment, and
- a parameter t parameterizing points on the ray (with $t = 0$ for the starting point and $t = 1$ for the end point of a ray segment).

Hence, the actual position of a photon, which is needed for building the photon map, can be computed from the starting point of the referenced ray and the parameter t.

Assuming the user defined parameters α and R are given the creation of the photon map requires the following steps:

Step 1: Create a binary 'occupation' grid (according to section 4.8.2) to identify space occupied by geometry.

Step 2: Perform particle tracing and store ray segments of multiple scattered rays to a linear list.

Step 3: Create photon references for each ray segment in the list:

1: // create empty list of photon references
   refList $\leftarrow \emptyset$
2: **for** each ray $r \in$ *rayList* **do**
3: // ray direction
   $\vec{v} \leftarrow endPoint(r) - startingPoint(r)$
4: $l \leftarrow \|\vec{v}\|$
5: $n \leftarrow \lfloor l/D \rfloor$

```
6:    // spacing of photon references
      dt ← D/l
7:    t ← 1
8:    for i = 1..n do
9:       p = tv⃗ + startingPoint(r)
10:      if (checkOccuGrid(p) = true) then
11:         newRef = createRef(r,t)
12:         refList ← refList ⋃ {newRef}
13:      end if
14:      t ← t − dt
15:   end for
16: end for
```

Step 4: Store photon references in a photon map (spatial KD-tree, based on the positions of the photon references).

4.8.4 Lookup in a Photon Map

The lookup is performed very similar to conventional photon mapping. A sphere of radius R is expanded around the lookup point and the closest n neighboring rays are located from the photon map. Since multiple photons may reference to a ray segment it has to be ensured that a ray segment is counted only once. Thus, if a reference is found in a lookup, the distance to the corresponding ray is computed for the density estimate and further references to this ray are ignored.

4.8.5 Sampling Error

Since a segment of the light path is sampled by several discrete photons, a sampling error—depending on the sampling density α occurs. There are ray segments which actually intersect the lookup region but get missed in a K-nearest-neighbor search since no reference photon is found. Hence, irradiance is underestimated systematically. Assuming infinite, equally distributed rays carrying equal portions of energy the probability that a ray intersects the spherical lookup region of radius R around a point x at distance r is equally distributed with respect to r. Recalling

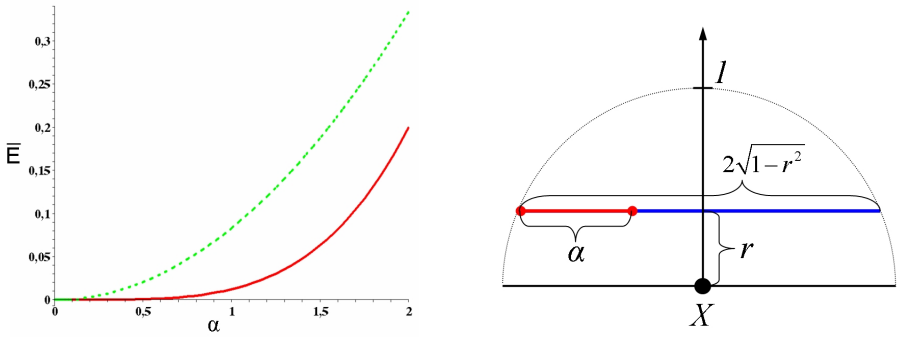

Fig. 4.12: **Left**: Average underestimation error. Solid line: Epanechnikov kernel. Dashed Line: box kernel. **Right**: For the probability p that a ray with distance r to a lookup point X is detected the following holds: $p = \min\left(1, 2\sqrt{1-r^2}/\alpha\right)$. The average probability is computed by integration with respect to r.

the definition of the sampling distance D ($D = \alpha R$) the average underestimation probability $\bar{p}(\alpha)$ is then given by (see Fig. 4.25 Right):

$$\bar{p}(\alpha) = \int_0^1 \min\left(1, \frac{2\sqrt{1-r^2}}{\alpha}\right) \mathrm{d}r. \tag{4.5}$$

Since we assumed equally distributed rays carrying equal portions of energy the flux through the lookup volume is under estimated by a factor of $1 - \bar{p}(\alpha)$.

In case of kernel based density estimation of irradiance, the contribution of a ray segments is commonly weighted by some kernel function κ. The shorter the shortest distance to the point where irradiance has to be estimated the more the ray contributes to the total incident irradiance. Hence, distant rays are less relevant for density estimation. Then for the average underestimation error $\bar{E}(\alpha)$ yields:

$$\bar{E}(\alpha) = 1 - \int_0^1 \kappa(r) \min\left(1, \frac{2\sqrt{1-r^2}}{\alpha}\right) \mathrm{d}r. \tag{4.6}$$

Here κ denotes an arbitrary kernel function. For the widely utilized Epanechnikov kernel (cf. [53]) and for $\alpha = 1$ this error is below 1.5 percent. Hence, sampling a

ray introduces only very little inaccuracies if the value for D is chosen similar to the maximum lookup radius R. Actually not infinite rays but ray segments are used for density estimation. Moreover, they do not carry all they same portion of energy in general. However, it turned out that using eqn. 4.6 to roughly compensate for sampling error can help to reduce potential bias (cf. section 4.8.6).

4.8.6 Radiance Estimation

In fact photons are used only to locate rays, any ray based radiance estimator (cf. [31, 17]) may be used in conjunction with our technique. To roughly compensate for the systematic under estimation error caused by our method (cf. section 4.8.5) we introduce an additional factor $s(\alpha) := 1/(1-\bar{E}(\alpha))$ which scales the radiance estimate according to the average underestimation error $\bar{E}(\alpha)$. Then for an adaptive kernel-based radiance estimator $L(x,\omega_o)$ with respect to some position x, an exitant direction ω_o and a local scattering function $f(x,\omega_i,\omega_o)$ yields:

$$L(x,\omega_o) = s(\alpha)\frac{\sum_{j=1}^{K}\kappa(d_j/d_{max})f(x,\omega_i^j,\omega_o)\Delta\phi_j}{d_{max}^2} \tag{4.7}$$

Here, the sum accounts for the K closest ray segments with respect to a given distance metric. According to this metric the distance of the j-th ray segment is denoted d_j and the maximum distance of a segment the estimate is based on is given by $d_{\max} := \max_{j=1..K}\left(d_j\right)$. The flux represented by the j-th ray is denoted $\Delta\phi_j$.

Note that the estimator $L(x,\omega_o)$ accounts for ray segments intersecting the lookup sphere of radius R. Hence, the bias of $L(x,\omega_o)$ depends not only on α but also implicitly on the choice of R.

4.8.7 Results and Conclusion

Since the main focus of this thesis is on fiber rendering, only a few selected case studies for surface rendering will be discussed. To exemplary demonstrate the capability of our approach we rendered the “robot in a box” scene shown in Fig. 4.13 for several settings using the Hemisphere-Disc Estimator of [17] and compared the results to conventional photon mapping (see Tab. 4.1). This scenes is challenging

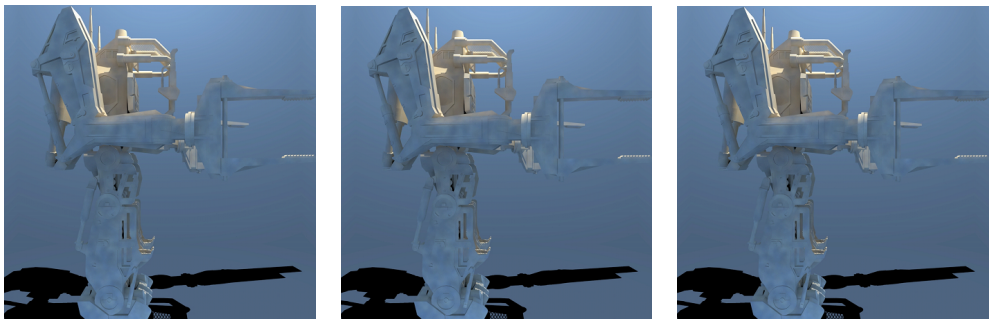

Fig. 4.13: A robot in a big, bluish box (four times the extent of the robot). Direct visualization of the ray-based photon map for **Left:** $\alpha = 1$, **Middle:** $\alpha = 1.5$, **Right:** $\alpha = 2$. Note that a bigger α introduces only little perceptual differences.

	pm	**rb**($\alpha = 1$)	**rb**($\alpha = 1.25$)	**rb**($\alpha = 1.5$)	**rb**($\alpha = 2$)
#photons/ray segments	2M p	2M rs	2M rs	2M rs	2M rs
#particle references	-	6.9M	5.7M	4.9M	4M rs
total mem usage	88MB	183MB	167MB	154MB	139MB
render times	1340s	1480s	1317s	1259s	1199s

Tab. 4.1: Rendering times and memory usage of the robot example (Fig. 4.13, Fig. 4.9) with various values of α compared to conventional photon mapping. Other settings: $K = 512$, $R \approx 3\%$ of the extent of the scene. The abbreviation "pm" stands for photon mapping and "rb" means the ray-based approach. Note that in case of ray-based global illumination, the Hemisphere-Disc Estimator of [17] was used for density estimation.

for both conventional photon mapping and ray mapping. The detailed, complex geometry exhibits substantial discontinuities. Consequently conventional photon mapping suffers from significant artifacts (cf. Fig. 4.9). As discussed in detail in [31, 17] this is a result of strong boundary and topological bias.

On the other hand, previous ray based methods like ray mapping cannot efficiently handle geometries being heterogeneously distributed. In our examples the ray density in the inner of the diffuse box (which has roughly twice the dimension of the robot) is very high. Hence, a huge number of references to ray segments need to be stored which will never be used for an estimate. Note that most of the interior of the box is visible, which makes an efficient lazy construction of the ray

map (cf. [17]) very problematic. Moreover the maximum lookup radius is much bigger than the extent of a KD-voxel and many redundant references to a single ray would be found during ray lookup, if ray mapping was used. Consequently Havran et al reported relative rendering times (compared to conventional photon mapping) ranging from two to five for simple scenes of relatively low complexity. In contrast the rendering times obtained with our approach are comparable to conventional photon mapping, not only for the examples given in this thesis. Also the memory requirements for our example is moderate compared to the test scenes presented by [17]. Moreover, this was achieved without any complex memory limiting/caching technique as is the case of Havran et al.

The actual performance of our approach is closely related to the sampling distance D. In this context the accuracy of our approach can be controlled by the sampling parameter α. Based on several tests we found that $\alpha \approx 1$ usually is a good compromise between accuracy and efficiency. However, as for conventional photon mapping, additional scene dependent fine tuning can substantially increase the performance without introducing noticeable artifacts (Fig. 4.13).

We showed that our approach is an efficient alternative to previous methods like ray mapping and ray caching, if perfect accuracy is not needed. The accuracy is scalable and can be adapted to a scene by only one parameter (α). Especially for heterogenous scenes it can be expected that our method clearly outperforms ray mapping in terms of memory efficiency and rendering speed. Since most infrastructure from conventional photon mapping can be reused, our approach is easy to integrate into existing photon mapping frameworks.

We think that extending the basic algorithm presented in this paper may further increase efficiency. For instance the value of α could not only be adapted to the geometry of a scene, but also according to the flux a ray represents. Rays carrying higher energies could be sampled more densely, than rays representing a low flux. Such an heuristic would increase the chance that “important photon paths” are not missed.

In the following section it will be shown, how our ray-based technique can be applied to fiber rendering.

4.9 Efficient Ray-Based Global Illumination for Fiber Assemblies

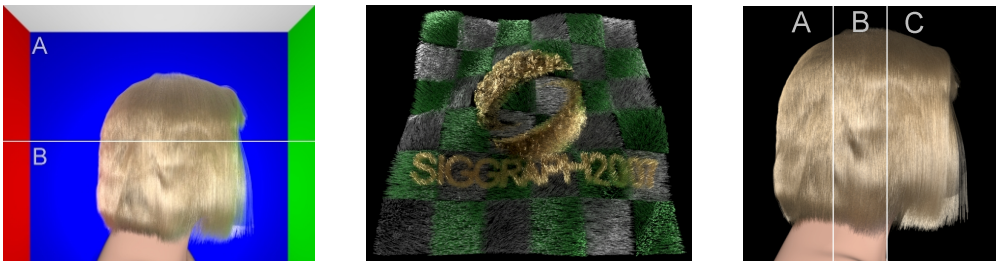

Fig. 4.14: **Left:** Color Bleeding. Split-screen comparison of our ray-based approximation, which is used for rendering the lower half of a blond hair style (B), with a path tracing reference used for the upper part (A). **Middle:** A carpet made of a mixture of fibers including the SIGGRAPH logo in golden fibers rendered with our ray-based approximation method. **Right:** Comparison: "double scattering" approximation (A, cf. Sec. 4.10), a path tracing reference (B), and our ray-based approximation (C).

In this section, a novel and efficient physically-based technique to accurately approximate global illumination for fiber based geometries is presented. Compared to the method proposed by Moon and Marschner [43] our approach differs on a conceptual level, since a variant of ray-based global illumination, introduced in the previous section, is used. The incident irradiance is evaluated from neighboring light paths and the exitant radiance is estimated according to a local fiber scattering function. In contrast to the approach presented by Moon and Marschner [43] our technique is based on the general and physically accurate concept of Bidirectional Fiber Scattering Distribution Functions (BFSDF) discussed in chapter 3. This strict formulation allows for a systematic derivation of approximations based on explicit assumptions which helps to identify potential sources of bias. Note for example that the fiber rendering integral (2) given in [43] implicitly assumes distant light sources (a constant illumination across the width of the fiber). But there is no a priori justification for such an assumption in case of indirect illumination. Hence, there are cases, where this implicit far-field assumption is a source of bias (see Fig. 4.15).

Fig. 4.15: Introducing bias by a far-field assumption for multiple fiber scattering. Path tracing results: A) according to section 4.7 using a near-field model for indirect illumination; B) with a far-field model. Notice the subtle but visible differences.

Our formulation is very flexible since it can—at least in principle—handle all different kinds of fibers and is not restricted to human hair only. Finally the method can be easily integrated into existing photon map based renderers, since most infrastructure developed for conventional photon mapping can be reused.

4.9.1 Overview

We will adopt the basic frame work for efficient ray-based global illumination (section 4.8) to fiber rendering. Incident irradiance at a fiber is estimated based on neighboring light paths via kernel based density estimation. To separate out direct illumination, which has different characteristics from the indirect the incident radiance distribution is split according to section 4.4. The direct illumination is always evaluated using the BCSDF and Monte Carlo integration of the corresponding scattering integral, whereas indirect illumination is estimated using a ray-based global illumination approach.
A key to an efficient approximation of indirect illumination is caching. Motivated by the fact that indirect illumination tends to have only little spatial variance along

a fiber it is evaluated only for a fixed set of sample positions. For simplicity, the exitant radiance is estimated on a per vertex basis and interpolated in-between. Adding level of detail and visibility considerations the performance of this approach can be enhanced further. The basic goal is to estimate global illumination only as accurate as needed. Note that in our context visibility does not necessarily mean direct visibility to an observer, but also indirect visibility—like visibility through a mirror.

Summing up, our method consists of the following four key steps:

Step 1: Visibility check and level of detail consideration.

Step 2: Particle tracing pass.

Step 3: Estimation of exitant radiance due to indirect illumination for a given point set (fixed to the fiber) based on step 1.

Step 4: Rendering: Interpolation of the radiance estimations of step 3 along the fibers.

4.9.2 Visibility Check and LOD

Typically, in case of complex fiber based scenes, not all fiber primitives are directly (or indirectly) visible to the camera. Hence, these primitives may be safely neglected for further considerations. Moreover, most primitives are not fully visible, but may be partially (even almost fully) covered by other primitives. For those primitives it is very likely that little inaccuracies in the radiance estimation will not drastically increase the perceptual error. Based on this assumption our approach approximates global illumination with respect to visibility.

Suppose that a fiber assembly is given by a set of segments with a cross section matching the effective diameter of a fiber. Then, in a first step a visibility measure for each segment primitive is computed. To account for direct visibility to the camera the scene is rendered from the camera's point of view and the number of eye rays hitting each primitive is counted. Based on this visibility measure our algorithm probabilistically decides whether to compute the global illumination at a segment or to interpolate it from neighboring segments. In addition a global

parameter β controls the accuracy of this approach by scaling the probability that the illumination is computed.

The algorithm can be described best by a pseudo code (see Alg. 3). It is possible to extend this heuristic strategy to other point sets than vertices. However, for simplicity we estimate the global illumination at a per vertex basis. During rendering this pre-computed radiance is then interpolated along the fiber.

4.9.3 Particle Tracing Pass

Assuming that internal light transport inside a fiber is limited to a small region around the incident position we can "concentrate" the BFSDF to the position where light penetrates a fiber without introducing high bias. The result is a BSDF varying with respect to h_i, which is used for the particle tracing phase. According to section 4.3.1 this BSDF can be computed right from the BFSDF of a given fiber:

$$f_{\mathrm{BSDF}}[h_i](\varphi_i,\theta_i,\varphi_o,\theta_o) := \int_{-\infty}^{\infty}\int_{0}^{2\pi} f_{\mathrm{BFSDF}}\mathrm{d}\xi_o\mathrm{d}\Delta s \tag{4.8}$$

with

$$\xi_o = \begin{cases} \varphi_o + \arcsin h_o, & 0 \le \varphi_o + \arcsin h_o < 2\pi, \\ 2\pi + \varphi_o + \arcsin h_o, & \varphi_o + \arcsin h_o < 0, \\ \varphi_o + \arcsin h_o - 2\pi, & \varphi_o + \arcsin h_o \ge 2\pi. \end{cases} \tag{4.9}$$

In the following it is assumed that all hairs are modeled either as flat ribbons or half cylinders always facing the ray and and having the same cross section as the original fiber.

Recalling section 4.8 each ray segment of the light path representing indirect illumination is sampled by several reference photons which are stored in a conventional photon map. If one of these photons is found in a nearest neighbor search, the corresponding ray segment is used in the radiance estimation. Suppose a ray segment with a starting position v_p and ending at another point v_s is given. Then photons being equally distributed along the segment by a certain distance D (cf. Fig. 4.11 Left) are stored in the map. For rays shorter than D a single photon is created at v_s. Note that it is important to limit the lookup region by a sphere of

radius R around the lookup point in order to avoid disproportional long estimation times in case of dark areas. Based on R the distance D can be expressed by multiples of R: $D = \alpha R$, where α is a parameter controlling the sampling density.

Although a single reference photon has only a low memory footprint it is important to avoid useless references which will never be used for density estimation. According to section 4.8 photon needs to be stored in the map only if it can potentially contribute in a radiance estimate, if the minimum distance to a visible fiber is less than R. A very efficient conservative approximation uses an uniform grid to identify empty regions (i.e. regions without visible fibers). The extent of this grid is based on the bounding box of the fiber based geometry and the edge length of a voxel is R (Fig. 4.11 Right). Note that using this technique we are not only able to identify relevant references but also segments of a light path which can be neglected, i.e. left out.

4.9.4 Radiance Reconstruction

Similar to conventional photon mapping the exitant radiance due to indirect illumination can now be estimated based on the photon map generated during particle tracing. We use a variant of a K-nearest-neighbor search to estimate irradiance due to indirect illumination. Based on this irradiance the exitant radiance is computed from the local BCSDF of the fiber. As described earlier in section 4.9.2 the radiance reconstruction is performed on a per vertex basis and interpolated along the fiber.

4.9.5 Approximating the BFSDF Rendering Integral

Based on the local BFSDF (the BFSDF at s_o) the exitant radiance L_o is approximated using illumination samples from the photon map. Applying a density estimator approximating the BFSDF rendering integral Lo is reconstructed. According to section 3.5 this integral is given by:

$$L_o(s_o,h_o,\varphi_o,\theta_o) = \int_{-\infty}^{\infty}\int_{-1}^{1}\int_{0}^{2\pi}\int_{-\pi/2}^{\pi/2} f_{\text{BFSDF}}(\Delta s,h_i,\varphi_i,\theta_i,h_o,\varphi_o,\theta_o) \cos^2\theta_i L_i(s_i,h_i,\varphi_i,\theta_i)\,\mathrm{d}\theta_i\,\mathrm{d}\varphi_i\,\mathrm{d}h_i\,\mathrm{d}\Delta s \tag{4.10}$$

Note that trying to solve this complex rendering integral with sparse samples from the photon map would give extremely noisy results. Therefore a simplified rendering integral will be derived. Based on this approximation the exitant radiance is estimated using a density based radiance estimator.

In a first step the integrand of (4.10) is modified by multiplying it by a piecewise constant function $C(x,c)$ with $C(x,c) = 1$ if $|x| \leq c$ and zero otherwise. Now the integral can be transformed to an equivalent form, where the integration with respect to h_i is no more limited to a compact interval $[-1,1]$:

$$L_o(s_o,h_o,\varphi_o,\theta_o) = \int_{-\infty}^{+\infty}\int_{-\infty}^{+\infty}\int_{0}^{2\pi}\int_{-\pi/2}^{\pi/2} f_{\text{BFSDF}}(\Delta s,h_i,\varphi_i,\theta_i,h_o,\varphi_o,\theta_o) C(h_i,1)\cos^2\theta_i L_i(s_i,h_i,\varphi_i,\theta_i)\,\mathrm{d}\theta_i\,\mathrm{d}\varphi_i\,\mathrm{d}h_i\,\mathrm{d}\Delta s \tag{4.11}$$

Assuming that all relevant scattering mainly occurs in a small region around the longitudinal incident coordinate s_i, all exitant scattering is "concentrated" to s_i. Hence, intensity can be measured only if $s_i = s_o$, which gives an extra delta distribution $\delta(\Delta s)$ in the integrand:

$$L_o(h_o,\varphi_o,\theta_o) \approx \int_{-\infty}^{+\infty}\int_{-\infty}^{\infty}\int_{0}^{2\pi}\int_{-\pi/2}^{\pi/2} \delta(\Delta s)\hat{f}_{\mathrm{BFSDF}}(h_i,\varphi_i,\theta_i,h_o,\varphi_o,\theta_o) \, C(h_i,1)\cos^2\theta_i L_i(s_i,h_i,\varphi_i,\theta_i)\,\mathrm{d}\theta_i\,\mathrm{d}\varphi_i\,\mathrm{d}h_i\,\mathrm{d}\Delta s \tag{4.12}$$

with

$$\hat{f}_{\mathrm{BFSDF}} = \int_{-\infty}^{+\infty} f_{\mathrm{BFSDF}}\left(\Delta s', h_i,\varphi_i,\theta_i,h_o,\varphi_o,\theta_o\right)\mathrm{d}\Delta s'. \tag{4.13}$$

It is very unlikely that the resolution of a photon map is good enough to resolve fine details across the width of a fiber. Therefore, a constant (directional) incident illumination across its width is assumed. Note that this far-field assumption (which is also implicitly assumed in [37]) is not a priori satisfied and may lead to substantial bias in some cases. However, since there is no general solution for this problem, we think that this approximation is acceptable. Assuming moreover a distant observer the exitant radiance may be averaged with respect to h_o (see also section 3.7). Applying these simplification one obtains the following approximate rendering integral:

$$L_o(\varphi_o,\theta_o) \approx \int_{-\infty}^{+\infty}\int_{-\infty}^{+\infty}\int_{0}^{2\pi}\int_{-\pi/2}^{\pi/2} f_{\mathrm{BCSDF}}(\varphi_i,\theta_i,\varphi_o,\theta_o) \, C(h_i,1)\delta(\Delta s)\cos^2\theta_i L_i(s_i,h_i,\varphi_i,\theta_i)\,\mathrm{d}\theta_i\,\mathrm{d}\varphi_i\,\mathrm{d}h_i\,\mathrm{d}\Delta s \tag{4.14}$$

with

$$f_{\mathrm{BCSDF}}(\varphi_i,\theta_i,\varphi_o,\theta_o) = \frac{1}{2}\int_{-1}^{1}\int_{-1}^{1}\int_{-\infty}^{\infty} f_{\mathrm{BFSDF}}\left(\Delta s', h_i',\varphi_i,\theta_i,h_o',\varphi_o,\theta_o\right)\mathrm{d}\Delta s'\,\mathrm{d}h_i'\,\mathrm{d}h_o'. \tag{4.15}$$

Finally (4.15) can be approximated by Monte Carlo density estimation using samples from the photon map.

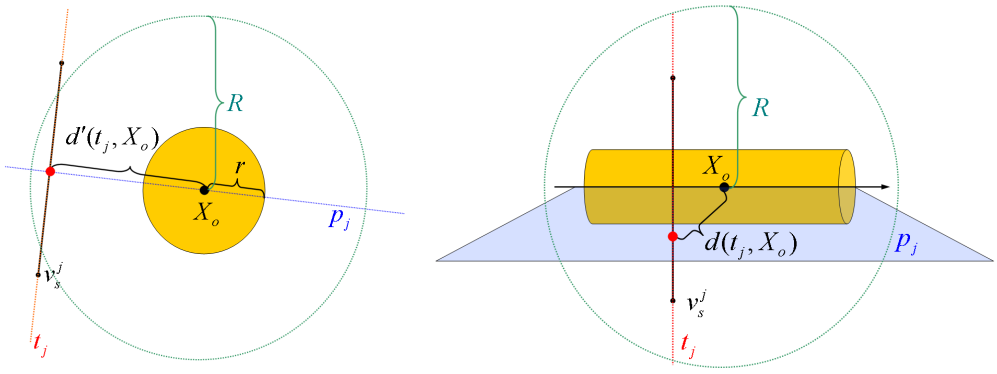

Fig. 4.16: Parameters of density estimation. The variable $\mathrm{d}'(p_j, v_s^j)$ is the projection of $\mathrm{d}(p_j, v_s^j)$ onto the cross section plane.

4.9.6 Radiance Estimation

Using the simplified rendering integral derived in section 4.9.5 the problem of radiance estimation can be approximately solved by density estimation based on a K-nearest-neighbor search with some adaptive kernel function κ.

Suppose the radiance at a point X_o at s_o on axis of a fiber of width $2r$ has to be estimated. Let r_j denote the j-th ray segment with endpoint v_s^j, direction ω_i^j and supporting line l_j. Consider the plane p_j at X_o and with normal ω_i^j. Those ray segments which intersect p_j or with $\mathrm{d}(p_j, v_s^j) < r$ are potential candidates for a K-nearest-neighbor density estimation (Fig. 4.16). In this context the K nearest ray segments are identified with respect to the distance $d_j = \max(\mathrm{d}(l_j, X_o) - r, 0)$. Then for the exitant radiance L_o to direction ω_o approximately holds:

$$L_o(s_o, \omega_o) \approx \frac{\sum_{j=1}^{K} \Delta\phi_j \kappa\left(\frac{d_j}{d_{\max}}\right) \cos\theta_i^j f_{\mathrm{BCSDF}}(\omega_i^j, \omega_o)}{d_{\max}^2} \tag{4.16}$$

with $\Delta\phi_j$ denoting the flux represented by the j-th ray segment and the maximum distance $d_{\max} = \max_{j=1,\ldots,K}(d_j)$. Note that f_{BCSDF} is the local BCSDF which is evaluated at s_o.

To reduce sampling bias we add a factor $s(\alpha) := 1/(1 - \bar{E}(\alpha))$ to the right hand side of (4.16), which roughly compensates for "missing rays". It scales the

radiance estimate according to the average underestimation error $\bar{E}(\alpha)$. With this modification one finally obtains the following radiance estimator:

$$L_o(s_o,\omega_o) \approx s(\alpha)\frac{\sum_{j=1}^{K}\Delta\phi_j\kappa\left(\frac{d_j}{d_{\max}}\right)\cos\theta_i^j f_{\mathrm{BCSDF}}(\omega_i^j,\omega_o)}{d_{\max}^2} \tag{4.17}$$

To verify our approach it was tested against unbiased path tracing using the implementation discussed in section 4.7.

Example	**#fibs**	**#tot segs**	**#segs**	**#photons**	**tracing**	**total**
Fig.4.14 Middle	120K	4.6 M	659K	13.4M	9 min	**75 min**
Fig.4.14 Left A	87K	5.4M	403K	12.5M	17 min	**68 min**
Fig.4.30 Left	87K	5.4M	418K	6.7M	18 min	**69 min**
Fig.4.30 Middle	81K	3.8M	367K	7.1M	17 min	**63 min**
Fig.4.30 Right	83K	4.8M	327K	7.9M	19 min	**58 min**
Fig. 4.26- 4.28 (average)	87K	5.4M	351K	6.5M	17 min	**64 min**

Tab. 4.2: Overview of examples used for the photon-mapping approach (see also Fig. 4.14, 4.30 and Fig. 4.26- 4.28). All estimates are based on 5M ray segments. From left to right: number of fibers, total number of fiber segments, number of fiber segments for which global illumination was estimated according to visibility and LOD, total number of reference photons in the photon map (to sample 5M ray segments), time for the particle tracing pass, total rendering time including single scattering and particle tracing. All images are originally rendered with a resolution 1024x1024 pixels and with 32 eye rays per pixel and the following parameters: $\alpha = 1.0$, $\beta = 1/32$, $K = 4096$. All tests were implemented on a P-IV with 3MHz.

4.9.7 Implementation and Results

For comparison between path tracing and the ray based solution several setups, to test different aspects of global illumination, were created. All materials base on the BFSDF models derived in section 3.10.

The first test scene (Fig. 4.14 Right C) compares the visual quality of multiple fiber scattering, which is very important for light colored hair. Note how well our approximation matches the unbiased path traced version. There are only very slight differences such as smoothing artifacts and color variations, which are a consequence of the bias introduced by the ray based approximation. Results for other perspectives of this scene are compared in Fig. 4.26- 4.28.

In a second test our approach was used to render more general global illumination effects such as color bleeding (Fig. 4.14 Left,Fig. 4.33). Again the approximations match the reference images very well. Since our ray based approach is very general, it can be used in conjunction with almost any kind of BFSDF. As an example we refer to Fig. 4.14 Middle, which shows a rendering of a carpet made of a mixture of artificial fibers including the SIGGRAPH logo consisting of golden fibers.

Finally, the ray based approach was tested in conjunction with animation. Although the photon map is visualized directly and generated from scratch for every frame, surprisingly little low frequency noise occurs. We believe that this slight noise can be eliminated by using standard techniques like inter frame filtering. However, even without any filtering the results indicate that our approach is usable also in the context of animation.

A typical BCSDF for a dielectric fiber like human hair may exhibit narrow scattering lobes (cf. [37]). Hence, the radiance estimate has to base on many neighboring ray segments (in our tests up to 4096) to get meaningful results. However, for extreme cases it can be appropriate to use a pre-filtered BCSDF (by applying energy-conserving smoothing) for radiance estimation. Although such a filtering provokes some additional bias it helps to keep the variance of the radiance estimate low. Note that the BCSDF was not modified for all examples presented in this paper. Exemplary renderings illustrating the importance of a dense photon map are given in Fig. 4.41.

All tests show that our approach is an efficient and general alternative to costly path tracing. It is up to two orders of magnitude faster and delivers accurate results with a relatively low memory footprint.

4.9.8 Comparison to Other Photon Mapping Based Approaches

We proved that ray-based global illumination is a very efficient approach for approximately solving the global illumination problem for fiber assemblies. However, there are other existing and potential photon mapping approaches which will now be discussed in more detail.

Moon and Marschner

Recently, a method for rendering multiple fiber scattering for human hair was presented by Moon and Marschner [43]. For this method the indirect incident radiance at a fiber is estimated for a certain set of directions which are chosen according to the scattering lobes of a dielectric cylinder and which account for "the most important" light paths contributing to viewing direction. Based on these samples the induced exitant radiance is computed from the far-field scattering model of Marschner et al. [37]. This approach is used for both, the path tracing reference solutions and the photon mapping approximations.

Choosing a set of "important light paths" can be seen as an instance of importance sampling, a general variance reduction technique. However, finding a set of "important directions" for a given Bidirectional Curve Scattering Distribution Function (BCSDF) is a non trivial problem (at least in the general case) which has not to be solved in our case. Moreover, the examples presented by [43] require an extremely high photon count (>90M photons) whereas for all of our examples this number was about one order of magnitude lower, cf. Table 4.2.

This situation does not only reflect an improved constant factor, but is asymptotically even more dramatic, as the asymptotic behavior (keeping the maximum lookup radius constant) is $O(n^2)$ vs. $O(n^5)$. In our approach the resolution of the estimate is inversely proportional to the maximum distance $d_{\max}$ in a K-nearest-neighbor search. Hence, according to (4.16) roughly four times more ray segments have to be generated to double the resolution. Letting the lookup radius R constant

the corresponding increase in the number of reference photons exhibits basically the same growth. On the other hand, in the approach of [43] the corresponding growth of photons is by a fifth power. However, in contrast to our approach this induces not only a better spatial but at the same time also a higher angular resolution of the map.

The radiance estimate of [43] is based on a 5-sphere which makes it very sensitive to variance of its radius, whereas our method is based on oriented discs (2-spheres), which gives much more robustness in the estimate. Although we have no mechanism to explicitly control smoothing in angular dimensions it turns out that using an adequate number of photons for radiance estimation yields accurate results with only little noise for a variety of realistic BCSDFs.

The overall memory footprint of our approach is substantially lower than for the method proposed in [43]. Not only because of using less photons in the photon map, but also because of sampling light paths by reference photons instead of conventional photons. These references require only little memory—in our implementation 8 bytes: A pointer to the corresponding segment of the light path and a scalar parameterizing the position on this ray segment.

Finally the method of [43] tends to systematically underestimate exitant radiance for points close to solid geometry, because incident radiance is integrated simultaneously over direction and volume. In contrast — since our estimation bases on oriented discs— less bias occurs (Fig. 4.17). For a more detailed discussion of this issue we refer to the next section.

A Volumetric Photon Mapping Approach

Although not yet implemented, a variant of volumetric photon mapping would be another option for the approximately solving the global illumination problem. In this case light paths would have to be uniformly sampled by photons very similar to [43]. Suppose the radiance at a point X_o at s_o has to be estimated and that N light paths were generated during particle tracing. Let furthermore p_j denote the j-th photon with position x_j, direction ω_i^j and representing a radiant flux $\Delta\phi_j$. Based on the K nearest photons (Euclidean distance) found in a small lookup region the

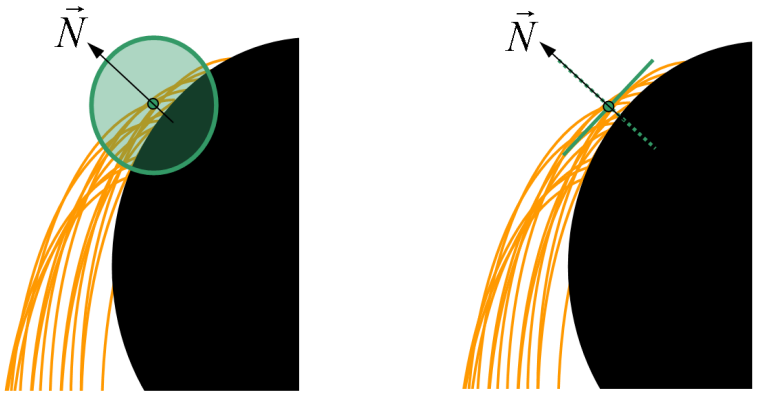

Fig. 4.17: Systematic under estimation of exitant radiance for points close to solid geometry (black). **Left**: Volumetric photon mapping. Here, the maximum lookup volume (indicated by a green disc) is always intersecting the solid. **Right**: Using oriented discs. If the solid geometry is locally convex, discs (indicated by a green line) oriented perpendicular to the local normal $\vec{N}$ do not intersect the solid geometry (best case: solid, worst case: dashed).

outgoing radiance L_o could be estimated with the following volumetric density estimator:

$$L_o(s_o,\omega_o) \approx \frac{\sum_{j=1}^{K} \Delta\phi_j \kappa'\left(\frac{d'_j}{d'_{\max}}\right) \cos\theta_i^j f_{\text{BCSDF}}(\omega_i^j,\omega_o)}{d'^3_{\max}} \tag{4.18}$$

with $d'_j = \mathrm{d}(X_o, x_j)$, $d'_{\max} = \max_{j=1,\ldots,K}\left(d'_j\right)$ and a volumetric kernel function κ'.

However, using a ray-based approximation has several advantages over such a volumetric photon mapping. First of all a ray-based approach needs photons only to identify ray segments and not to characterize its length covered inside the lookup region as for volumetric photon mapping. This situation is directly related to the fact that a volumetric estimator is used: To double the resolution of the estimate, roughly eight times more photons are needed. Moreover, since the estimate is based on a 3-sphere, the variance introduced by little inaccuracies of $d'_{\max}$ is higher than for the ray-based method where the estimate is based on a 2-sphere.

In addition, a volumetric approach tends to provoke higher bias for scenes consisting not only of fibers but also of other solid geometry. As a common example lets consider a human head with almost straight hair. In this case it is very likely that the volume used for density estimation is intersecting the head geometry introducing high under estimation bias since the head volume never contains any photon. For ray based density estimation this error is less prominent since it is based on oriented discs. If a disc is oriented roughly along the surface normal it is very likely that it is not intersecting the head geometry minimizing estimation error (Fig. 4.17).

4.10 Physically Plausible Approximation of Multiple Fiber Scattering for Hair

When rendering light colored hair, multiple fiber scattering is essential for the right perception of the overall hair color. However, although our ray-based approximation can basically handle this effect quite efficiently, rendering times can still be an issue, in particular if interactive frame rates are needed.

Especially in the context of self shadowing for (interactive) hair rendering several publications address some aspects of efficient global illumination for hair volumes [7, 40, 28, 66, 34, 16]. However, there is no canonic mapping of physically based material properties to the parameters of these techniques. All these ad-hoc approaches may give plausible images in some situations but provide no general physically-based solution. Moreover, multiple fiber backward scattering is neglected or modeled by ad-hoc fiber based diffuse or ambient components. But since such components have no physical basis a plausible look requires massive parameter tweaking. Moreover, it is very likely that static parameter settings do not suffice. Hence, if the camera moves or the illumination changes the parameters have to be readjusted.

As now will be shown, multiple fiber scattering can be approximated very well by using aggressive simplifications. In this context, a novel technique to efficiently approximate this effect for a full head of human hair or a similar fiber based geometry is presented. In particular we claim the following contributions:

- We show that multiply scattered light in a hairstyle can be approximated well by accounting for only two different anisotropic components: A *global backscattering* component subsuming all multiple backscattered light and *global forward scattering* subsuming all forward scattered light, respectively.

  In section 4.10 we summarize some facts about scattering in a hairstyle motivating this claim; in section 4.10.8 we compare results of our "double scattering" approximation with the ones of unbiased Monte Carlo path tracing verifying the claim for many settings, in which we systematically vary relevant parameters of hairstyles.

- We derive an *analytical* fiber-based approximation for *global backscattering* (Sec. 4.10.2).

- We present a novel approach for estimating *global forward scattering*, which is closely related to existing shadow map based approaches (Sec. 4.10.4).

  In contrast to all prior ad-hoc methods our "double scattering" approximation is generic and delivers physically plausible results for human hairstyles. Hence, no parameter tweaking is needed and a suitable approximation for multiple scattering is computed right from the scattering function of an individual fiber—specifically the BCSDF.

- Two different implementations are presented in section 4.10.7. First, a technique which accurately evaluates global backscattering and global forward scattering "on the fly" and second, a less accurate, but more efficient technique which bases on pre-computed maps. In addition we sketch, how the method can be implemented on a GPU, which opens the door for interactive photo realistic hair rendering.

4.10.1 Basic Ideas and Assumptions

In the following we show how multiple fiber scattering can be approximated using the BCSDF for dielectric fibers, in particular the BCSDF proposed in section 3.10.2 or the model presented by Marschner et al. [37]. However, our simplifications base on several assumptions on the properties of multiply scattered light at clusters of disciplined fibers (Fig.4.20 Left):

- In contrast to direct illumination the scattering distribution of multiple fiber scattering tends to be smooth and behaves in a quite predictable manner, cf. Fig. 4.6.
- For clusters of dielectric fibers strong anisotropic "global" multiple scattering highlights occur: a strong global highlight if the fibers are lit from behind and another one due to front lights.
- Multiple scattering is highly anisotropic if the BFSDF of a fiber (e.g. human hair) exhibits narrow scattering lobes. In this case the scattering stays directional, even after several scattering events [37, 43]. Otherwise multiple fiber scattering would be rather isotropic and its approximation less challenging (see also Fig. 4.35).

Accounting for these key properties the basic idea of our approach is to characterize all multiple fiber scattering by only two smooth anisotropic components, namely

- *global forward scattering* subsuming all multiple forward scattering, or
- *global backward scattering* subsuming multiple backward scattering, respectively.

The final approximation is a combination of both components. For each light source the incident (highly anisotropic) light distribution approaching a strand is estimated using a simple analytical approximation for global forward scattering. Then the scattered light is computed based on the BCSDF of a fiber and an approximation for global backward scattering.

Global forward and backward scattering are derived from multiple fiber scattering at a cluster of disciplined hair. Throughout the next section it is always assumed that the BFSDF which is used to approximate multiple fiber scattering does not explicitly depend on φ_o and φ_i, but on the relative azimuth $\phi = \varphi_o - \varphi_i$. This assumption is in particular satisfied for fibers with a circular cross section. For fibers exhibiting a non circular (in particular elliptic) cross section we propose to use a suitable symmetric approximation instead. For instance the original BFSDF could be replaced by the corresponding BFSDF for a circular cross section. Due to statistical variations in the orientation of the fibers it can be expected that such a modification causes only moderate bias in many cases.

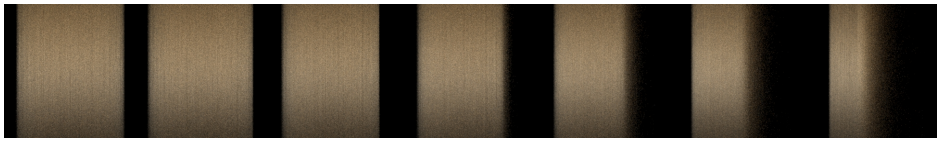

Fig. 4.18: The directionality of global backward scattering. The images show path tracing renderings of the indirect illumination of a cluster formed by vertically aligned hairs which is illuminated by one directional fixed front light. The camera is moving around the cluster (along the azimuth angle of the fibers, $0^\circ \leq \phi \leq 60^\circ$) while keeping the view point fixed. The global backward scattering highlight is centered over the specular cone and isotropic with respect to azimuth.

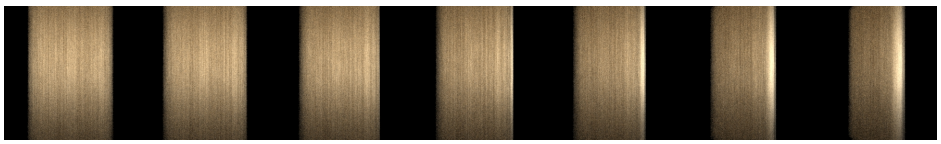

Fig. 4.19: The directionality of global forward scattering. The images show path tracing renderings of the indirect illumination of a cluster formed by vertically aligned hairs which is illuminated by one directional fixed back light. The camera is moving around the cluster (along the azimuth angle of the fibers, $0^\circ \leq \phi \leq 60^\circ$) while keeping the view point fixed. As for global backward scattering (cf. Fig 4.18) the global forward scattering highlight is centered over the specular cone and is nearly isotropic with respect to azimuth. The more scattering events occur, the more scattered light becomes isotropic.

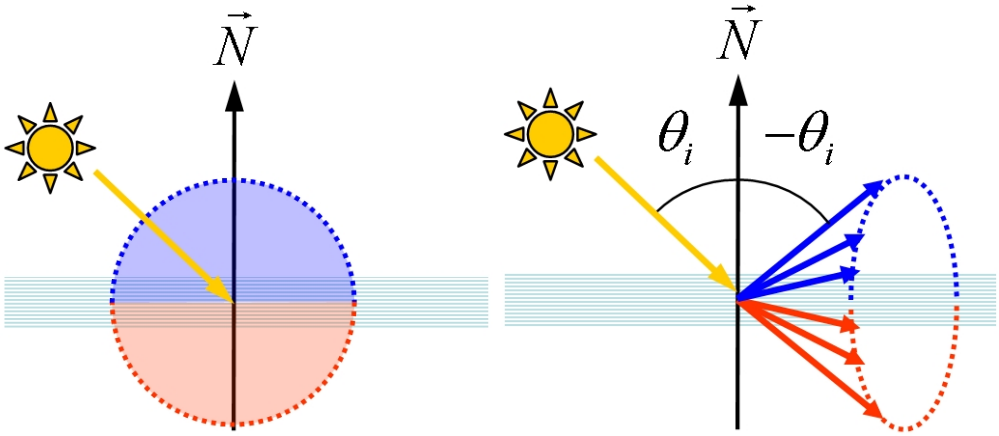

Fig. 4.20: **Left:** Global forward (blue) and backward (red) scattering at a cluster of parallel fibers (with cluster normal $\vec{N}$). The back scattering and forward scattering hemispheres are indicated by the dashed blue and the red circles, respectively. **Right:** For a cluster of parallel, smooth dielectric fibers all multiple scattered light lies on a cone (indicated by the dashed circle). This follows from the BFSDF of a dielectric fiber which forms a specular cone.

4.10.2 Approximation of Global Backscattering by a Local BCSDF

Consider a collection of almost parallel fibers, e.g. a strand of combed hair, which is illuminated by a front light. Then a substantial fraction of incident light is scattered back by multiple fiber scattering leading to some additional global highlight. Neglecting this backscattered light may totally change the hair color. The additional highlight has the following characteristics (cf. Fig.4.18):

- strong anisotropy with respect to inclination with a maximum intensity approximately at the specular cone (see Fig.4.20 Right) which directly follows from the fact that a smooth dielectric fiber exhibits a focused tangential/longitudinal scattering, cf.[37];

- little variation along the azimuth for a fixed inclination θ_o because multiple fiber scattering further spreads the anyway broad azimuthal scattering of a dielectric fiber (assuming that the orientation of the glints varies statistically) [37, 43] ;

- small amount of angular blurring around the specular cone for almost smooth fibers; this blurring is more prominent if the BFSDF exhibits wider longitudinal scattering lobes (see also Fig. 4.35).

Based upon these observations we now derive an approximation for this global highlight. Suppose a dense, infinite and layered fiber cluster with cluster normal $\vec{N}$ and orientation $\vec{O}$ is given (Fig. 4.22). Let furthermore each layer be oriented perpendicular to $\vec{N}$. In the following we make the ideal assumption that each fiber is aligned to $\vec{O}$ and belongs to exactly one layer and neglect all other geometrical properties of the cluster (in particular the actual distance between fibers). This kind of abstraction is possible, since our approximation is based on statistics about discrete, uncorrelated scattering events. In this case the attenuation along a light path does not depend on the path length within the hair volume or on the actual scatterers, but only on the number and quality of scattering events. Figure 4.21 shows that this simplification is justified for hair clusters. In addition—because an infinite, uniformly illuminated cluster was assumed—only the angular distribution of backscattering is relevant and no spatial variation along the cluster occurs.

Please note that the cluster concept is introduced only to roughly estimate multiple scattering at disciplined hair and that the final approximation will no longer rely on this assumption.

Fig. 4.21: The influence on the hair density on global (multiple fiber) backward scattering. The images show path tracing renderings of the indirect illumination of a cube (20 x 20 x 20 cm) formed by vertically aligned hairs which is illuminated by one directional front light. The fiber density (from left to right) is: 400, 200, 100 hairs$/\text{cm}^{-2}$. Note that the hair density has virtually no influence on backward scattering for typical human hair densities ($\approx 200\,\text{hairs}/\text{cm}^{-2}$).

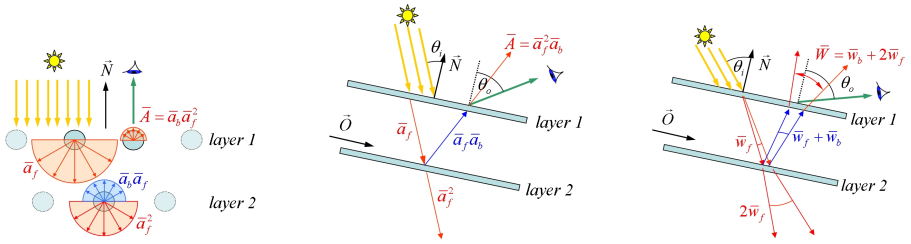

Fig. 4.22: Approximation of multiple fiber scattering from a dense, infinite, layered cluster of dielectric fibers. All scattering is classified as either forward or backward scattering with respect to cluster normal $\vec{N}$ and all fibers are aligned to an orientation $\vec{O}$. **Left:** Average azimuthal scattering and average attenuation along a light path. **Middle:** Longitudinal scattering along the specular cone (cone angle is $2\theta_i$) and average attenuation. **Right:** Longitudinal scattering. Each segment of the light path is modeled by a Gaussian beam describing the angular distribution of light. At each scattering event the width of a beam is increased.

4.10.3 Backscattering from a Cluster

In the following incident lights from the hemisphere oriented around $\vec{N}$ will be denoted as front lights and lights from the complemental hemisphere as back lights. In addition, we assume as that all incident light is purely directional and that the projection of the incident direction ω_i onto the normal plane equals $-\vec{N}$.

Our approximation of the global highlight is based on backscattering from a cluster due to front lights which is modeled by an additional subsurface scattering like term f_{back} in the local BCSDF, hence:

$$f'^{\text{dielectric}}_{\text{BCSDF}}(\varphi_i,\theta_i,\varphi_o,\theta_o) = f^{\text{dielectric}}_{\text{BCSDF}}(\varphi_i,\theta_i,\varphi_o,\theta_o) + f_{\text{back}}(\varphi_i,\theta_i,\varphi_o,\theta_o) \tag{4.19}$$

Here the function f_{back} denotes the probability density function for curve scattering due to subsurface scattering if the cluster is illuminated from (φ_i,θ_i). The basic idea is to model this function by separate factors estimating the overall reflectance and the angular (azimuthal and longitudinal) distribution of the global backscattering component:

1. A normalized Gaussian lobe $g(\bar{W}(\theta_i),\bar{S}(\theta_i),\theta_o+\theta_i)$ modeling the longitudinal angular distribution of global backward scattering component around the specular cone. Here the parameters $\bar{W}(\theta_i)$ means the standard deviation of this Gaussian and the expectation $\bar{S}(\theta_i)$ accounts for a possible shift with respect to the specular cone.

2. A factor $\bar{A}(\theta_i)$ approximating the average probability for global backward scattering (reflectance) accounting for absorption and Fresnel attenuation.

3. A "phase function" $\tilde{g_b}(\phi)$ to model the azimuthal directionality of the subsurface component. This function should conveniently reflect the rather isotropic backscattering with respect to azimuth. Since light illuminating the width of a fiber is scattered to a half cone (backward scattering only) this function should normally integrate to two along this half cone. For simplicity $\tilde{g_b} = 2/\pi$ was assumed.

4. A factor $(\cos\theta_i)^{-1}$ accounting for the fact that backward scattered light is roughly spread to the specular cone.

5. Another factor of $(\cos\theta_i)^{-1}$ taking into account the parameterization of scattering.

Putting all factors together yields the following model for f_{back}:

$$f_{\text{back}} = \frac{\tilde{g_b}\bar{A}}{\sqrt{2\pi}\bar{W}\cos^2\theta_i} e^{-\frac{(\theta_o+\theta_i-\bar{S})^2}{2\bar{W}^2}}. \tag{4.20}$$

Let's suppose that a fiber exhibits relatively narrow scattering lobes which is commonly satisfied by e.g. human hair (see the measurements presented in [37]). Then scattering paths and attenuation roughly match the ones of perfect smooth fibers. Hence, tracing a Gaussian beam centered over this path, which spreads at each scattering event and which gets attenuated according to a smooth fiber, is a suitable approximation for the non smooth case, cf. Fig. 4.22. Since all fibers are parallel and directional illumination is assumed, all back scattered light roughly lies in a lobe of a certain width (standard deviation) $\bar{W}$ around the specular cone. Moreover this lobe may exhibit some shift $\bar{S}$ with respect to this specular cone.

Strictly speaking, only the fact that all light scattered from a smooth fiber stays exactly in the specular cone will be needed for estimating the reflectance due to backscattering. Suppose the BFSDF of a dielectric fiber $f_{\text{BFSDF}}^{\text{dielectric}}$ is given. Then a corresponding BFSDF $\hat{f}_{\text{BFSDF}}^{\text{dielectric}}$ exhibiting a perfect specular lobe can be deduced:

$$\begin{aligned}\hat{f}_{\text{BFSDF}}^{\text{dielectric}}&(h_i,\varphi_i,\theta_i,h_o,\varphi_o,\theta_o,\Delta s) = \\ &\frac{\delta(\Delta s)\delta(\theta_o+\theta_i)}{\cos^2\theta_i}\int_{-\infty}^{\infty}\int_{-\pi/2}^{\pi/2} \\ &\quad f_{\text{BFSDF}}^{\text{dielectric}}(h_i,\varphi_i,\theta_i,h_o,\varphi_o,\theta_o',\Delta s')\cos^2\theta_o' \mathrm{d}\theta_o' \mathrm{d}\Delta s'\end{aligned} \tag{4.21}$$

Intuitively speaking all scattering is concentrated to the specular cone and to incident position. In the following we suppress the Δs dependence, since we are always assuming scattering from the incident position.

Computing the Cumulated Probability $\bar{A}$ for Global Backward Scattering

For $\hat{f}_{\text{BFSDF}}$ the attenuation of multiply scattered light is estimated separately from its angular distribution. For a rough approximation of $\bar{A}$ we statistically analyze all backscattered light.

In a first step each scattering event of a light path is classified either as forward or backward scattering with respect to the cluster normal $\vec{N}$. Based on this classification the average attenuation of a light path in case of forward scattering $\bar{a}_f(\theta_i)$ and backward scattering $\bar{a}_b(\theta_i)$ at a fiber is computed:

$$\bar{a}_f(\theta_i) = \frac{1}{\pi} \int_{\frac{-\pi}{2}}^{\frac{\pi}{2}} \int_{\frac{3\pi}{2}}^{\frac{\pi}{2}} \int_{\frac{\pi}{2}}^{\frac{3\pi}{2}} \hat{f}_{\text{BCSDF}}^{\text{dielectric}}(\varphi_i', \varphi_o', \theta_i, \theta_o') \mathrm{d}\varphi_o' \mathrm{d}\varphi_i' \cos^2\theta_o' \mathrm{d}\theta_o' \tag{4.22}$$

$$\bar{a}_b(\theta_i) = \frac{1}{\pi} \int_{\frac{-\pi}{2}}^{\frac{\pi}{2}} \int_{\frac{3\pi}{2}}^{\frac{\pi}{2}} \int_{\frac{3\pi}{2}}^{\frac{\pi}{2}} \hat{f}_{\text{BCSDF}}^{\text{dielectric}}(\varphi_i', \varphi_o', \theta_i, \theta_o') \mathrm{d}\varphi_o' \mathrm{d}\varphi_i' \cos^2\theta_o' \mathrm{d}\theta_o'. \tag{4.23}$$

Here $\hat{f}_{\text{BCSDF}}^{\text{dielectric}}$ denotes the BCSDF of the modified BFSDF $\hat{f}_{\text{BFSDF}}^{\text{dielectric}}$.

Note that these approximations imply that the inclination (absolute value) of scattered light is $|\theta_i|$, regardless of the actual scattering sequence. According to [37] this assumption is satisfied for smooth dielectric fibers.

Using these coefficients we compute the total attenuation $\bar{A}$ as the probability that light is scattered back. Hence, we account for all backscattered paths, consisting of $2n+2$ forward and $2m+1$ backward scattering events ($m, n \in \mathbb{N}_0$). Then the attenuation of a path $\bar{a}$ is given by the product (see Fig. 4.22):

$$\bar{a} = \bar{a}_f^{2n+2} \bar{a}_b^{2m+1}. \tag{4.24}$$

Note again that all scattered light stays exactly in the specular cone and that the scattering along the specular cone is assumed to be isotropic. Summing over all backscattering paths gives an analytical approximation for $\bar{A}$, cf. section 4.10.3:

$$\bar{A} \approx \bar{a}_b \bar{a}_f^2 \frac{(1 + \bar{a}_b^2 + \bar{a}_b^4 + \bar{a}_f^2(\bar{a}_b^4 - 4 + \bar{a}_b^2(\bar{a}_f^2 - 2) + 6\bar{a}_f^2 - 4\bar{a}_f^4 + \bar{a}_f^6))}{(1 + \bar{a}_f)^2 (1 - \bar{a}_f)^2 (1 - \bar{a}_f^2)^3} \tag{4.25}$$

A Detailed Derivation of $\bar{a}_f$, and $\bar{a}_b$

The coefficient $\bar{a}_f$ denotes the average attenuation of a light path in case of forward scattering from a smooth dielectric fiber, if the incident illumination is constant with respect to φ_i (Incident light forms a half cone according to Fig. 4.22 Left). Since a circular symmetric cross section was assumed, we w.l.o.g. assume that $\pi/2 \leq \varphi_o \leq 3\pi/2$ are the outgoing directions of forward scattering. Then one gets by integration:

$$\begin{aligned}\bar{a}_f(\theta_i) = \frac{1}{2\pi} &\int_{-\pi/2}^{\pi/2}\int_{\pi/2}^{3\pi/2}\int_{3\pi/2}^{\pi/2}\int_{-1}^{1}\int_{-1}^{1} \\ &\hat{f}^{\text{dielectric}}_{\text{BFSDF}}(h_i,\varphi_i,\theta_i,h_o,\varphi_o,\theta_o)\mathrm{d}h_i\mathrm{d}h_o\mathrm{d}\varphi_i\mathrm{d}\varphi_o\cos^2\theta_o\mathrm{d}\theta_o \\ = \frac{1}{\pi} &\int_{\pi/2}^{3\pi/2}\int_{3\pi/2}^{\pi/2}\int_{-\pi/2}^{\pi/2} \hat{f}^{\text{dielectric}}_{\text{BCSDF}}(\varphi_i,\theta_i,\varphi_o,\theta_o)\cos^2\theta_o\mathrm{d}\theta_o\mathrm{d}\varphi_i\mathrm{d}\varphi_o\end{aligned} \tag{4.26}$$

The coefficient $\bar{a}_b$ denotes the complemental backward scattering with outgoing directions in the range $0 \leq \varphi_o < \pi/2$ and $3\pi/2 < \varphi_o < 2\pi$:

$$\begin{aligned}\bar{a}_b(\theta_i) = \frac{1}{2\pi} &\int_{-\pi/2}^{\pi/2}\int_{3\pi/2}^{\pi/2}\int_{3\pi/2}^{\pi/2}\int_{-1}^{1}\int_{-1}^{1} \\ &\hat{f}^{\text{dielectric}}_{\text{BFSDF}}(h_i,\varphi_i,\theta_i,h_o,\varphi_o,\theta_o)\mathrm{d}h_i\mathrm{d}h_o\mathrm{d}\varphi_i\mathrm{d}\varphi_o\cos^2\theta_o\mathrm{d}\theta_o \\ = \frac{1}{\pi} &\int_{\pi/2}^{3\pi/2}\int_{3\pi/2}^{\pi/2}\int_{-\pi/2}^{\pi/2} \hat{f}^{\text{dielectric}}_{\text{BCSDF}}(\varphi_i,\theta_i,\varphi_o,\theta_o)\cos^2\theta_o\mathrm{d}\theta_o\mathrm{d}\varphi_i\mathrm{d}\varphi_o\end{aligned} \tag{4.27}$$

Note that all scattering is averaged with respect to azimuth.

Computing the Width $\bar{W}$ and the Shift $\bar{S}$ of the Global Backward Scattering Lobe

In order to estimate the longitudinal width of the global backscattering lobe $\bar{W}$ a scattering path is approximated by a sequence of Gaussian beams with successively increased widths (standard deviation with respect to θ). At each scattering

event—which is again classified as either forward or backward scattering—an incident beam (radiance distribution) L_i is scattered according to the BCSDF of a fiber.

For simplicity, the longitudinal angular scattering distribution of a BCSDF is approximated by two normalized Gaussians which estimate the average angular distribution in case of forward scattering and for backscattering, respectively. The corresponding widths are denoted $\bar{w}_f(\theta_i)$ and $\bar{w}_b(\theta_i)$.

Let's for example consider an incident beam with an angular distribution modeled by a normalized Gaussian $g_i(\theta, w_i)$ of width w_i and another normalized Gaussian $g_b^{BCSDF}(\theta, \bar{w}_b)$ approximating average longitudinal backward scattering. Then $g_i \star g_b^{BCSDF}$ describes the average backscattering distribution, which is a Gaussian distribution again. The width of this distribution is given by $\sqrt{w_i^2 + \bar{w}_b^2}$.

A light path may exhibit multiple scattering events. To estimate the total angular distribution of a scattering sequence, the incident beam has to be successively convolved with the simplified Gaussian scattering distribution for forward or backward scattering, respectively (Fig. 4.22 Right).

Based on the total angular distribution of a single path the width $\bar{W}$ of the global backscattering lobe is computed as the weighted average of all multiple backward scattering paths. The following analytical approximation is derived in section 4.10.3:

$$\bar{W} \approx \left(1 + \frac{\bar{a}_f^2}{2}\right) \frac{\bar{a}_b \sqrt{2\bar{w}_f^2 + \bar{w}_b^2} + \bar{a}_b^3 \sqrt{2\bar{w}_f^2 + 3\bar{w}_b^2}}{\bar{a}_b + \bar{a}_b^3 \left(2\bar{w}_f + 3\bar{w}_b\right)} \tag{4.28}$$

Human hair exhibits several highlights, which are slightly longitudinally ("along the tangent") shifted with respect to the specular cone [37]. We account for these shifts by computing an average shift $\bar{S}$ for the global highlight very similar to $\bar{W}$. It is computed from the average shifts $\bar{s}_f(\theta_i)$ and $\bar{s}_b(\theta_i)$) of forward and backward scattered light, cf. section 4.10.3:

$$\begin{aligned} \bar{S} \approx \bar{s}_b & \frac{\bar{a}_f^6 + 3(\bar{a}_f^2 - \bar{a}_f^4) + 2\bar{a}_b^2(\bar{a}_f^2 - 1) - 1}{(\bar{a}_f^3 + 3(\bar{a}_f^2 + \bar{a}_f) + 1)(\bar{a}_f^3 + 3(\bar{a}_f - \bar{a}_f^2) - 1)} \\ + \bar{s}_f & \frac{4\bar{a}_f^2(1 - \bar{a}_b^2) - 2\bar{a}_f^4 - 2}{(\bar{a}_f^3 + 3(\bar{a}_f^2 + \bar{a}_f) + 1)(\bar{a}_f^3 + 3(\bar{a}_f - \bar{a}_f^2) - 1)}. \end{aligned} \tag{4.29}$$

A Detailed Derivation of $\bar{A}$, $\bar{W}$, and $\bar{S}$

Consider a dense infinite fiber cluster exhibiting a regular, layered structure as described in section 4.10.2. To roughly approximate the reflectance due to multiple fiber scattering we compute the average probability for backscattering $\bar{A}$. This probability is estimated by summing over all possible light paths contributing to backscattering.

Each light path is characterized by a sequence of scattering events. In this context each scattering event is classified as either forward or backward scattering with respect to the cluster normal, cf. Fig. 4.22. According to this sequence the attenuation along a light path is roughly estimated by a product of the average attenuation coefficients $\bar{a}_b$ and $\bar{a}_f$. Note that since a layered structure was assumed each path has to pass a layer twice: If it enters a layer and if it gets scattered back through it. Hence, the number of forward scattering events is even. In contrast the number of backscattering events has to be odd for all backscattering paths.

Consider the probability α_{2i+1} that light is scattered back by $2i+1$ backscattering scattering events. Then the total probability for backscattering can be expanded with respect to i:

$$\bar{A} = \sum_{i=0}^{\infty} \alpha_{2i+1} \tag{4.30}$$

Assuming a small $\bar{a}_b$ which is true for most dielectrics we skip this expansion for $i > 2$:

$$\bar{A} \approx \alpha_1 + \alpha_3 + \alpha_5 \tag{4.31}$$

Analyzing all possible scattering paths at an infinite cluster yields following expressions for $\alpha_1, \alpha_3, \alpha_5$:

$$\alpha_1 = \bar{a}_b \sum_{i=1}^{\infty} \bar{a}_f^{2i} = \frac{\bar{a}_b \bar{a}_f^2}{1-\bar{a}_f^2} \tag{4.32}$$

$$\alpha_3 = \bar{a}_b^3 \sum_{i=1}^{\infty} \sum_{j=0}^{i-1} \sum_{k=j+1}^{\infty} \bar{a}_f^{2i-2j-2+2k} = \frac{\bar{a}_b^3 \bar{a}_f^2}{\left(1-\bar{a}_f^2\right)^3} \tag{4.33}$$

$$\alpha_5 = \bar{a}_b^5 \sum_{i=1}^{\infty} \sum_{j=0}^{i-1} \sum_{k=j+1}^{\infty} \sum_{l=0}^{k-1} \sum_{m=l+1}^{\infty} \bar{a}_f^{2i-2j-4+2k-2l+2m}$$

$$= \frac{\bar{a}_b^5 \left(-1-\bar{a}_f^2\right) \bar{a}_f^2}{\left(\bar{a}_f-1\right)^2 \left(1+\bar{a}_f\right)^2 \left(\bar{a}_f^2-1\right)^3} \tag{4.34}$$

Finally (4.31) can be rearranged to match (4.25).

The approximation of multiple fiber scattering presented in section 4.10 accounts also for the angular distribution of scattered light.

The longitudinal angular distribution of backward scattered light is modeled by a Gaussian $g(\bar{W}, \bar{S}, \theta_o + \theta_i)$ centered over the specular cone.

To approximate the width $\bar{W}$ of this lobe the spread of incident directional light is estimated by statistical analysis of scattering of a sequence of Gaussian beams centered around the specular cone. At each scattering event—which is again classified as either forward or backward scattering—the width of the incident beam increases according to the BCSDF of a fiber.

The average standard deviation of the BCSDF with respect to θ is denoted by $\bar{w}_f$ in case of forward scattering and $\bar{w}_b$ for backward scattered light, respectively. Assuming that these two widths are a viable description of the angular spread of scattering at a fiber they can be used to roughly estimate the width of a scattered Gaussian beam.

Hence, if an incident beam of width w_i is scattered at a fiber the resulting width w_i' of the scattered beam can be computed by convolving the initial Gaussian beam with a Gaussian of width $\bar{w}_f$ for forward scattering and $\bar{w}_b$ for backward scattering, respectively. The convolution is another Gaussian characterizing the angular distribution of the scattered light. Its width w_i' is given by:

$$w_i' = \sqrt{w_i^2 + \bar{w}_{b,f}^2}. \tag{4.35}$$

If an incident beam is scattered along a path of multiple scattering events its width successively increases according to (4.35).

Let's suppose that $\bar{a}_f$, $\bar{a}_b$, $\bar{w}_f$ and $\bar{w}_b$ have been computed and that similar to (4.30) all backscattering is expanded with respect to the number of backscattering events. Then $\bar{W}$ is the weighted average of all cumulated widths of all multiply scattered paths contributing to the global highlight. Skipping the expansion after the third

term yields

$$\bar{W} \approx \frac{\omega_1 + \omega_3 + \omega_5}{\bar{A}} \tag{4.36}$$

with

$$\omega_1 = \bar{a}_b \sum_{i=1}^{\infty} \bar{a}_f^{2i} \sqrt{2i\bar{w}_f^2 + \bar{w}_b^2}, \tag{4.37}$$

$$\omega_3 = \bar{a}_b^3 \sum_{i=1}^{\infty} \sum_{j=0}^{i-1} \sum_{k=j+1}^{\infty} \bar{a}_f^{2i-2j-2+2k} \sqrt{3\bar{w}_b^2 + (2i-j-2+2k)\bar{w}_f^2}, \tag{4.38}$$

$$\omega_5 = \bar{a}_b^5 \sum_{i=1}^{\infty} \sum_{j=0}^{i-1} \sum_{k=j+1}^{\infty} \sum_{l=0}^{k-1} \sum_{m=l+1}^{\infty} \bar{a}_f^{2i-2j-4+2k-2l+2m} \tag{4.39}$$

$$\sqrt{5\bar{w}_b^2 + (2i-2j-4+2k-2l+2m)\bar{w}_f^2}). \tag{4.40}$$

The sum (4.36) is approximated analytically by (4.28).

According to the section 3.10.2 (see also [37]) the BFSDF is approximated by sums of scattering functions accounting for different scattering lobes f^i_{BFSDF}.

$$f_{\mathrm{BFSDF}} = \sum_i f^i_{\mathrm{BFSDF}} \tag{4.41}$$

The longitudinal scattering distribution of such a lobe is commonly modeled by normalized Gaussians. In this context the corresponding standard deviation will be denoted w_i.

Based on this decomposition $\bar{w}_f$ and $\bar{w}_b$ are approximated by taking into account the relative contribution of a lobe in case of backward scattering (I^b_i) and forward scattering (I^f_i), respectively:

$$I^b_i = \frac{1}{\pi \bar{a}_b(\theta_i)} \int_{3\pi/2}^{\pi/2} \int_{3\pi/2}^{\pi/2} \int_{-\pi/2}^{\pi/2} f^i_{\mathrm{BCSDF}}(\varphi_i, \theta_i, \varphi_o, \theta_o) \cos^2\theta_o \mathrm{d}\theta_o \mathrm{d}\varphi_i \mathrm{d}\varphi_o \tag{4.42}$$

$$I_i^f = \frac{1}{\pi \bar{a}_f(\theta_i)} \int_{\pi/2}^{3\pi/2} \int_{3\pi/2}^{\pi/2} \int_{-\pi/2}^{\pi/2} f^i_{\mathrm{BCSDF}}(\varphi_i, \theta_i, \varphi_o, \theta_o) \cos^2\theta_o \mathrm{d}\theta_o \mathrm{d}\varphi_i \mathrm{d}\varphi_o \tag{4.43}$$

Using I_i^f and I_i^f the widths $\bar{w}_f$ and $\bar{w}_b$ are estimated by the weighted average of all widths w_i neglecting potential shifts of the lobes:

$$\bar{w}_b = \sum_i I_i^b w_i \tag{4.44}$$

$$\bar{w}_f = \sum_i I_i^f w_i \tag{4.45}$$

Human hair exhibits several highlights, which are slightly longitudinally shifted with respect to the specular cone [37]. If the average shifts $\bar{s}_f(\theta_i)$ and $\bar{s}_b(\theta_i)$) of forward and backward scattered light (fiber based) are given then an average shift $\bar{S}$ of the global highlight can be estimated. Note that these shifts can be basically computed from the expectation of the scattering distribution with respect to θ. However, if longitudinal scattering is explicitly modeled by Gaussian lobes $\bar{s}_f(\theta_i)$ and $\bar{s}_b(\theta_i)$ can be approximated similar to $\bar{w}_f$ and $\bar{w}_b$:

$$\bar{s}_b = \sum_i I_i^b s_i \tag{4.46}$$

$$\bar{s}_f = \sum_i I_i^f s_i \tag{4.47}$$

where s_i denotes the shift of the i^{th} scattering lobe. Then for the shift of the global highlight $\bar{S}$ the following holds:

$$\bar{S} \approx \frac{\varsigma_1 + \varsigma_3 + \varsigma_5}{\bar{A}} \tag{4.48}$$

with

$$\varsigma_1 = \bar{a}_b \sum_{i=1}^{\infty} \bar{a}_f^{2i} \left(2i\bar{s}_f + \bar{s}_b\right), \tag{4.49}$$

$$\varsigma_3 = \bar{a}_b^3 \sum_{i=1}^{\infty} \sum_{j=0}^{i-1} \sum_{k=j+1}^{\infty} \bar{a}_f^{2i-2j-2+2k} \left(3\,\bar{s}_b + (2i-2j-2+2k)\,\bar{s}_f\right), \tag{4.50}$$

$$\varsigma_5 = \bar{a}_b^5 \sum_{i=1}^{\infty} \sum_{j=0}^{i-1} \sum_{k=j+1}^{\infty} \sum_{l=0}^{k-1} \sum_{m=l+1}^{\infty} \bar{a}_f^{2i-2j-4+2k-2l+2m} \left(5\,\bar{s}_b + (2i-2j-4+2k-2l+2m)\,\bar{s}_f\right). \tag{4.51}$$

The function 4.48 is approximated by (4.29).

4.10.4 Approximation of Global Forward Scattering

In the following we will present a novel approach for estimating the forward scattered component which is closely related to shadow mapping. The basic idea of shadow maps is to compute occlusion for opaque objects by rendering a scene from a light's point of view and storing information about the depth of the first visible surface in a two dimensional map. Then every point in the scene which has a bigger distance (from the lights point of view) than the appropriate depth value stored in the map is in shadow with respect to that light source. This shadow map idea was extended to render self shadowing for translucent objects like hair. Instead of only a single depth value a transmittance (visibility) function with respect to depth is stored in every element of the map. This function encodes the fraction of light reaching a (sampled) point in space along a ray from this point to the light source

However, since multiple fiber scattering is typically highly anisotropic it is not sufficient to approximate a hair cluster—which exhibits some regular structure—by a simple density distribution. Note that such an assumption was implicitly made by all previous shadow map based approaches in the realm of hair rendering [7, 40, 34, 66, 15]. In contrast to prior approaches the incident light distribution f_{forward} penetrating a fiber in case of indirect illumination is estimated by a physically-based, anisotropic transmittance function T and a *spread function* S modeling the angular spread of the illumination:

$$f_{\text{forward}} = TS. \tag{4.52}$$

Similar to section 4.10.3 all following derivations base on the assumption that a fiber exhibits relatively narrow scattering lobes which is commonly satisfied by human hair [37]. Again scattering from a fiber cluster Again scattering from a fiber cluster according to figure 4.20 is the basis for all further considerations and it is assumed that all incident light is purely directional and that the projection of the incident direction ω_i onto the normal plane equals $\vec{N}$.

Computing the Transmittance Function T

Consider a straight path starting at the light source (light sample) which is parameterized by a direction $\vec{x}$ and a parameter t. Let $\text{Fibs}(t',\vec{x}) := \{\text{fib}_1,\ldots,\text{fib}_n\}$ be an ordered set according to the sequence $Seq(t',\vec{x})$ of all fibers intersecting the path until a position t'. Let furthermore $\Theta(t',\vec{x}) := \{\theta_i^1,\ldots,\theta_i^n\}$ be the ordered set of the corresponding incident inclinations with respect to incident direction $\vec{x}$. Note that scattering along a straight path occurs only in exactly one single case: if all fibers along the path lie in the same plane and if the incident ray enters at $h_i = 0$. However, to approximate the attenuation of forward scattered light penetrating t' we compute the average attenuation for a path exhibiting n forward scattering events, with inclinations $\Theta(t')$. Suppose an average attenuation coefficient $\bar{a}_f(\theta_i^k)$ for forward scattered light is given according to Sect. 4.10.3. Then the total attenuation is a product of all attenuation coefficients along a path with one factor per scattering event. Hence, for the transmittance function $T(t',\vec{x},\text{Fibs},\Theta)$ the following holds:

$$T(t',\vec{x},\text{Fibs},\Theta) := \begin{cases} 1, & n = 0, \\ \prod_{k=1}^{n} \bar{a}_f(\theta_i^k), & n > 0. \end{cases} \tag{4.53}$$

Although a transmittance function can be evaluated on the fly (see also section 4.10.7), it is commonly approximated by pre-computed deep shadow or opacity shadow maps.

Computing the Spread Function S

However, it is not sufficient to account only for the attenuation along a light path. There is also an angular spread at each scattering event which must not be ne-

glected since it changes the ray density (Fig. 4.22 Right). Therefore a *spread function S* is introduced which roughly approximates the angular distribution of the global forward scattering component. The longitudinal distribution is modeled by a normalized Gaussian of width $\bar{W}_T$ and the azimuthal directionality by a "phase function" $\tilde{g_f}(\phi)$. Assuming an isotropic distribution $\tilde{g_f} = 1/\pi$ is used.

Finally, this yields the following expression for S:

$$S = \frac{\tilde{g_f}}{\sqrt{2\pi}\bar{W}_T} e^{-\frac{(\theta_o+\theta_i)^2}{2\bar{W}_T^2}}. \tag{4.54}$$

This equation can not be applied for direct illumination ($n = 0$) since then the incident light was assumed to be directional. We account for this special case by making a case differentiation:

$$S := \begin{cases} \delta(\omega_i + \omega_o), & n = 0, \\ \frac{\tilde{g_f}}{\sqrt{2\pi}\bar{W}_T} e^{-\frac{(\theta_o+\theta_i)^2}{2\bar{W}_T^2}}, & n > 0. \end{cases} \tag{4.55}$$

Similar to the transmittance T the width $\bar{W}_T$ is estimated based on the sequence $Seq(t', \vec{x})$ by accumulating the average widths $\bar{w}_f(\theta_i)$ of a sequence till position t':

$$\bar{W}_T(t', \vec{x}, \text{Fibs}, \Theta) = \sqrt{\sum_{k=1}^{n} \bar{w}_f^2(\theta_i^k)}. \tag{4.56}$$

4.10.5 Combining the Models for Global Backward and Forward Scattering

Please note that the cluster concept was introduced only to motivate the characteristics of scattering at disciplined hair. In the following we generalize our approach by characterizing forward and backward scattering with respect to projection of the incident light light direction ω_i onto the normal plane (ω_i'). Hence, all multiple fiber scattering is computed for a virtual cluster aligned to the local hair tangent ($\vec{O} = \vec{u}$) and with $\vec{N} = -\omega_i'$. Since all azimuthal back and forward scattering is rather isotropic along the specular cone and because locally disciplined hair was assumed this generalization is applicable.

Now that we have models for forward and global backward scattering, both component can be combined to estimate the exitant scattering distribution according to Fig. 4.23. Suppose a directional light source with normal irradiance $E_\perp$ is

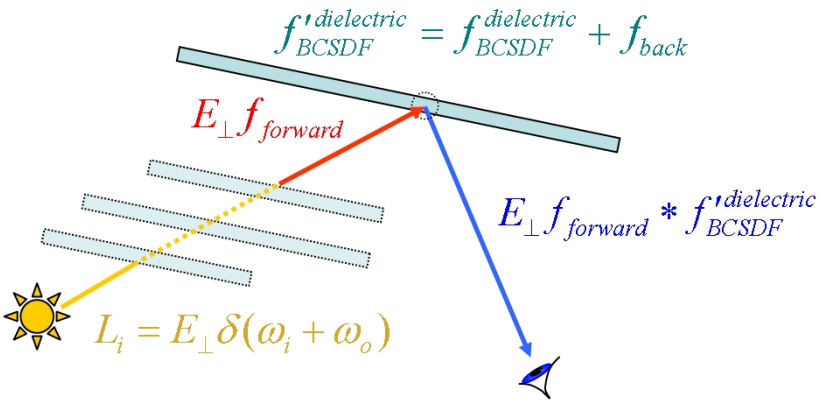

Fig. 4.23: Combining forward and backward scattering. For a directional light source L_i the incident illumination approaching a fiber is modeled by $E_\perp f_{\text{forward}}$. To obtain the exitant radiance this distribution is convolved with $f'^{\text{dielectric}}_{\text{BCSDF}}$.

illuminating the scene from direction ω_i. In this case the illumination penetrating a fiber is modeled by $E_\perp f_{\text{forward}}$ and the exitant scattering distribution $E_\perp D(\omega_i, \omega_o)$ can be described by convolving f_{forward} with the scattering function $f'^{\text{dielectric}}_{\text{BCSDF}}$ already defined in section 4.10.3:

$$D(\omega_i, \omega_o) = f_{\text{forward}}(\omega_i) \star f'^{\text{dielectric}}_{\text{BCSDF}}(\omega_i, \omega_o). \tag{4.57}$$

Hence, assuming distant illumination, the total exitant radiance L_o at a hair fiber can be computed by integrating the incident radiance with respect to solid angle:

$$L_o(\omega_o) = \int_\Omega L_i(\omega_i) D(\omega_i, \omega_o) \cos\theta_i(\omega_i) \mathrm{d}\omega_i \tag{4.58}$$

Note that the forward scattering components explicitly accounts for light paths exhibiting exclusively forward scattered events. Since forward scattering is clearly dominant for hair and most other dielectric fibers, the impact of this restriction tends to be comparatively small. Moreover, some multiple scattering effects of forward scattering are implicitly captured also by f_{back} ($f_{\text{back}} > 0$ for forward scattering).

Our "double scattering" approximation described by (4.58) only accounts for the angular scattering distribution of multiple scattered light. Hence, it can not

be used to properly simulate spatial volumetric scattering effects such as light diffusion.

Using the Scattering Models of Marschner et al. and the BCSDF Introduced in Section 3.10.2

To date the model proposed by Marschner et al. [37] and the BCSDF presented in section 3.10.2 are the only physically-based scattering functions for light scattering from dielectric fibers. Both models are expressed by a sum of three scattering lobes accounting for the three most relevant scattering components which are denoted R-, TT- and TRT-component according to Marschner at al.[37].

$$f_{\mathrm{BCSDF}}^{\mathrm{dielectric}} = f_{\mathrm{BCSDF}}^{\mathrm{R}} + f_{\mathrm{BCSDF}}^{\mathrm{TT}} + f_{\mathrm{BCSDF}}^{\mathrm{TRT}} \tag{4.59}$$

For each of the components $f_{\mathrm{BCSDF}}^{\mathrm{R,TT,TRT}}$ the longitudinal angular distribution is modeled by a Gaussian. Let $w_{\mathrm{R,TT,TRT}}^{\theta}$ denote the width (standard deviation) of a lobe according to section 3.10.2. (These widths are denoted $\beta_{\mathrm{R,TT,TRT}}$ in [37]).

If those lobes are only slightly shifted with respect to the specular cone—which is fulfilled for human hair according to the measurements of [37]—and if $\bar{W}_T$ is sufficiently small the convolution in (4.57) can be approximated by using the following expression for D:

$$D := \begin{cases} f'^{\mathrm{dielectric}}_{\mathrm{BCSDF}}, & n = 0, \\ 2\tilde{g}_f(f_{\mathrm{BCSDF}}^{\mathrm{dielectric}}(w_{\mathrm{R,TT,TRT}}^{\theta} \leftarrow w_{\mathrm{R,TT,TRT}}^{\prime\theta}) & \\ \quad + f_{\mathrm{back}}(\bar{W} \leftarrow \bar{W}')), & n > 0. \end{cases} \tag{4.60}$$

In case of direct illumination ($n = 0$) nothing changes compared to (4.57). Since the incident illumination is directional, the convolution with $f'^{\mathrm{dielectric}}_{\mathrm{BCSDF}}$ trivially yields $f'^{\mathrm{dielectric}}_{\mathrm{BCSDF}}$ as for (4.57). However, in case of indirect illumination ($n > 0$) we explicitly exploit the fact that the incident illumination is modeled by a narrow lobe of width $\bar{W}_T$. Then all incident light is concentrated around a single light direction θ_i'. Hence, assuming that the variance of the attenuation of the scattering paths is only a moderate, D can be estimated by computing $f'^{\mathrm{dielectric}}_{\mathrm{BCSDF}}$ for $\theta_i = \theta_i'$ and by increasing the widths of the scattering lobes in $f'^{\mathrm{dielectric}}_{\mathrm{BCSDF}}$ according to $\bar{W}_T$: $w_{\mathrm{R,TT,TRT}}^{\prime\theta} = \sqrt{(w_{\mathrm{R,TT,TRT}}^{\theta})^2 + \bar{W}_T^2}$ and $\bar{W}' = \sqrt{\bar{W}^2 + \bar{W}_T^2}$.

4.10.6 Modifications and Details

Although the basic model derived in the last section gives plausible results already, some minor empirically motivated modifications can further improve the results for many relevant scenes and settings:

- We replace θ_i by the relative inclination $\theta_d = (\theta_o - \theta_i)/2$, as was already suggested in [37] for their single scattering model.

- The width and the shift of the global highlight are computed for the strongest color channel (e.g. red, green or blue) only, but then is used for all other components, too. This prevents color shifting artifacts, which otherwise might occur.

- All conventional Gaussians in the model are replaced by the following modified Gaussian:

  $$g(\sigma, x) := N(\sigma)\exp(-x^2/(2\sigma^2))$$

  with a normalization factor of

  $$N(\sigma) := 1/\int_{-\pi/2}^{\pi/2} \exp(-x^2/(2\sigma^2))\mathrm{d}x.$$

  The modified Gaussian is less critical for wider lobes since it is normalized with respect to the domain of θ ($\pi/2 \leq \theta \leq -\pi/2$).

- We found that a slight underestimation of $\bar{W}$ tends to be more noticeable than overestimation. To improve the perceptual quality for complex hairstyles, we therefore propose to slightly increase the longitudinal width of the backscattering highlight $\bar{W}$ by an empirical factor of 1.2.

- For real hairstyles backscattering is less pronounced than for an ideal infinite cluster. A compromise is to scale the global backscattering component f_{back} slightly down. Good results were obtained with a factor of 0.9.

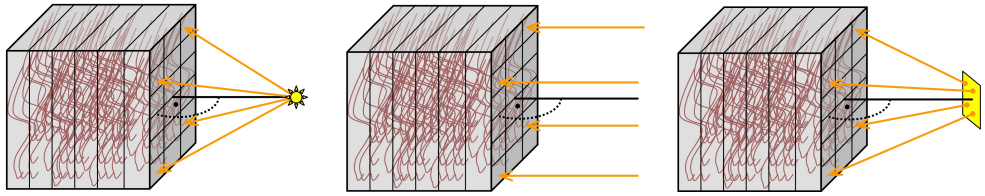

Fig. 4.24: An illumination map consists of a set of parallel slices oriented perpendicular to the average light direction. The extent of the map is given by the bounding box aligned to the orientation of the slices. Examples: **Left:** point light source, **Middle:** directional light source, **Right:** small area light source.

4.10.7 Rendering

We used our approach with two different techniques:

1. A method where both transmittance and spread are computed on the fly ("ray shooting method") and

2. a more efficient technique which uses pre-computed illumination maps very similar to opacity/shadow maps.

However, both methods imply that $\bar{a}_f, \bar{a}_b, \bar{w}_f, \bar{w}_b, \bar{s}_f, \bar{s}_b$ are given. We compute these values offline using numerical integration which takes only a few seconds on a standard desktop PC.

Ray Shooting Method

The first method is straight forward, since it approximates T and $\bar{W}_T$ by shooting rays from the point were radiance has to be estimated to the light source accumulating spread and transmission along a ray. The algorithm can be easily integrated into existing ray tracing frameworks. Every time a ray intersects a hair object a ray (very similar to conventional shadow rays) is shot to a given light sample and T and $\bar{W}_T$ are evaluated according to (4.53) and (4.56). Finally the exitant radiance is computed according to (4.60). A more detailed pseudo code description is given by Alg. 1.

Using Pre-computed Illumination Maps

Based on the ideas of the previous section it is now shown, how pre-computed illumination maps can be implemented to accelerate rendering (see also Alg. 2). Our approach is closely related to the methods described in [7, 28]. For each light source the hair volume is sliced into a set of parallel slices perpendicular to the average light direction (see Fig. 4.24). A slice contains a two dimensional, regular grid holding information about the average illumination approaching a grid element. To estimate the illumination, a scene is rendered from the lights point of view using a fixed number of sample rays. For each sample the transmittance and the spread of light is accumulated along the ray according to (4.53) and (4.56) and stored if a slice is intersected. Moreover the illumination is classified as either direct or indirect. Finally the transmittance and the spread is averaged with respect to each grid element and the average fraction of direct illumination is computed.

Using these pre-computed maps the illumination approaching a point in space can be estimated via trilinear interpolation. Since our implementation is based on ray tracing, for each ray-hair intersection a lookup in the corresponding illumination map has to be performed for every light source.

Naturally, the visual quality of this approach strongly depends on the spatial resolution of the illumination map as well as on the number of ray samples used to create it. If the number of samples is not adequate the rendering exhibits noise and if the resolution of the grid is chosen too low artifacts —such as smoothing— occur. The time which is needed to compute an illumination map is proportional to the number of ray samples used to approximate the illumination and is typically in the order of only a few minutes per light source. A comparison of results obtained with different settings are shown in Fig. 4.41, 4.42.

Our tests indicated that even an uncompressed representation of a typical illumination map has only moderate memory requirement. However, due to its cubic memory complexity it still makes sense to think about a more compact representation. In our implementation each grid element uses 64 bits of memory. The transmittance which is in the range of $[0, 1]$ is packed to a 32 bit representation. For each color channel of the RGB-model 10 bits are used to encode the mantissa for each color channel. The remaining two bits are used as an additional exponent

which is fixed for all channels. The fraction of direct illumination which is also in the range of $[0,1]$ and the spread which is limited by 2π are both stored in 16 bits each. However, using a deep shadow map like compression scheme the memory requirements could be reduced further [34].

Towards Interactive Hair Rendering

One bottleneck of our current implementation is that costly ray tracing is used for rendering. Replacing it by a more efficient line rendering algorithm could dramatically increase the performance of our illumination map method, especially in the context of hardware accelerated rendering. Moreover, it has been shown that using graphics hardware transmittance maps can be computed at interactive frame rates by rendering the scene from lights point of view (using multiplicative blending) [7, 30]. Since the spread map can be computed very similar (with additive blending) and the direct visibility can be computed with traditional shadow maps our approach is suitable to be implemented on existing graphics hardware.

4.10.8 Results

Our approach is a rough physically-based simplification and it cannot be expected that it fully preserves all detail while using such an aggressive approximation. However, for many relevant cases the results are surprisingly accurate. Moreover, the rendering times dramatically decreased compared to path tracing and to the ray-based approach presented before (see Tab. 4.2 and Tab. 4.3). In contrast to existing deep/opacity shadow map based techniques no additional ad-hoc material parameters are needed and both global back and forward scattering is approximated based on the BCSDF of a fiber.

For a first systematic comparison we refer to Fig. 4.34 where scattering from a cluster of disciplined hair is rendered using the "double scattering approximation". There are visible differences compared to the results obtained with unbiased path tracing. However, irregularities which occur in real hairstyles tend to conceal such errors.

A comparison proving the potential of our "double scattering" approximation is presented in Fig. 4.36. It shows renderings of a blond hairstyle obtained

Example	path tracing	ray shooting	map	time for map building
Fig. 4.36	18 h	19 min	**8 min**	4 min
Fig. 4.26 (avg. times)	17 h	15 min	**7 min**	4 min

Tab. 4.3: Total rendering times for exemplary scenes (3 GHz Pentium 4). First column: path tracing reference; Second column: "double scattering" approximation using ray shooting; Third column: "double scattering" using illumination maps (the given rendering times already include the times for map building); Fourth column: time for building the maps. All maps were generated based on 1.5M samples and have a resolution (extent of a voxel) of 0.5 cm.

using opacity shadow maps, the novel approximation and path tracing (as a reference). For this quite complex example the overall hair color is clearly dominated by multiple back scattering. Although there are slight differences which are noticeable with a side by side comparison, our approximation matches the reference quite well, whereas the opacity shadow map results, obtained with a re-implementation of [29], completely fails in reproducing the correct hair color since it lacks a backscattering component.

Another example is given in figures 4.26 to 4.28. Here a blond hairstyle is rendered from different perspectives. Again most of the intensity comes from multiple fiber scattering and the reference image is matched very well by our approximation, regardless of the perspective.

Slight changes of the optical properties of a fiber—such as absorption—may have a drastic impact on the overall hair color. As it can be seen in Fig. 4.31, the approximation handles such a variation correctly. However, for very light fibers (e.g. Fig. 4.31, leftmost image) there are visible differences.

Finally we varied the longitudinal widths of the scattering lobes in a range which is typical for human hair. The results shown in Fig. 4.35 clearly indicate that our approach properly accounts for such variations.

Discussion of Artifacts and Bias

Since our "double scattering" technique is a biased approach it can not be expected that it always preserves all scattering details, even if the basic assumptions are fulfilled. However, it is hard to quantify the actual bias introduced by our solution. Of course, it is possible to construct cases where it is very likely that the bias is noticeable.

Especially if the mean path length of light is big or if only very little attenuation occurs, global illumination strongly depends on the global structure of a hairstyle. Hence, if a fiber exhibits only very little absorption (Fig. 4.31, leftmost image) or if the fibers are loosely and non-uniformly distributed visible bias can occur (Fig. 4.39), in particular if the individual fibers are locally not aligned (Fig. 4.39, bottom row). A more systematic comparison for different hair densities is given in figure 4.40.

Also, if only a small strand of hair is rendered, the assumption that every hair is embedded in a layered cluster is no longer valid which typically leads to significant estimation error (See Fig. 4.38).

If different fibers are mixed the assumption that a hair fiber is surrounded by similar fibers is clearly violated. This leads to some bias as it can be seen when having a closer look at Fig. 4.37. Using the approximation the overall color is slightly different and the highlights are more distinguishable.

However, in cases arising in the context of hair style there seems to be the effect of a "statistical averaging" towards the assumptions leading to plausible results even if assumptions are violated. In addition, our approach accounts for local variations of the orientations of the fibers since it is evaluated per strand.

Recapitulating therefore, it can be said that the approximation gives quite accurate results if a hairstyle can be locally approximated by a dense, aligned hair cluster. On the other hand there are cases where significant bias is introduced. But even for those cases the results look still plausible and much more convincing than without accounting for multiple fiber scattering. Moreover, the bias can be identified only with a side by side comparison to a reference solution.

4.10.9 Conclusion and Future Work

Multiple fiber scattering in hair and similar geometry is essential for the overall color. This scattering is quite a complex phenomenon, which could previously handled adequately only by costly techniques such as photon mapping, ray based rendering or path tracing. However, we showed that it is basically possible to model the effect by aggressive simplifications while still preserving the right look. Moreover, we presented a novel "double scattering" approach which is much less costly than existing accurate approaches but still delivers physically plausible results. In contrast to existing techniques no ad-hoc parameter tweaking is needed and both, anisotropic forward and backward scattering, is based on Bidirectional Curve Scattering Distribution Functions. Moreover the method is well suited to be implemented on current hardware. Realizing such an implementation will be one topic of our future work. The improved performance of these methods might also be crucial when estimating the model parameters of hair fibers from photographs in an analysis-by-synthesis loop. In this context our approximations for global illumination might be sufficient in many settings—at least in initial iterations of such a loop.

4.11 Pseudo Codes for Sec. 4.9 and Sec. 4.10

Algorithm 1 Pseudo code for the ray shooting method.

// Estimate exitant radiance L_o at a point P to direction ω_o

EstimateRadiance(p, ω_o)**:**

$L_o = 0$

for all light samples l_i **do**

  $r \leftarrow$**GenerateRaySegment**(p, l_i)

  $T \leftarrow$ **AccumulateTransmittance**(r)

  $\bar{W}_T \leftarrow$ **AccumulateSpread**(r)

  if $\bar{W}_T = 0$ **then**

    $L_o \leftarrow L_o +$ **Intensity**$(l_i) \cdot \cos^2 \theta_i \cdot f'^{\text{dielectric}}_{\text{BCSDF}}(w_i, \omega_i, \omega_o)$

  else

    $w_i' \leftarrow \sqrt{w_i^2 + \bar{W}_T^2}$

    $\bar{W}' \leftarrow \sqrt{\bar{W}^2 + \bar{W}_T^2}$

    $L_o \leftarrow L_o +$ **Intensity**$(l_i) \cdot \cos^2 \theta_i \cdot \tilde{g_f} \cdot \left(f^{\text{dielectric}}_{\text{BCSDF}}(w_i', \omega_i, \omega_o) + f_{\text{back}}(\bar{W}', \omega_i, \omega_o) \right)$

  end if

end for

GenerateRaySegment(p, l_i)**:**

Generates a ray segment between a light sample l_i and a point p.

AccumulateTransmittance(r)**:**

Evaluates the transmittance function along a ray segment r according to (4.53).

AccumulateSpread(r)**:**

Evaluates the spread function along a ray segment r according to (4.56).

Algorithm 2 Pseudo code for the map based approach.

// Exitant radiance L_o at a point P to direction ω_o
EstimateRadiance(p, ω_o)**:**
$L_o = 0$
for all lights l_i **do**
  $T \leftarrow$ **InterpolateTransmittance**(p, l_i)
  $\bar{W}_T \leftarrow$ **InterpolateSpread**(p, l_i)
  $d \leftarrow$ **InterpolateDirectFraction**(p, l_i)
  $L_{direct} \leftarrow$ **Intensity**$(l_i) \cdot \cos^2 \theta_i \cdot f'^{\text{dielectric}}_{\text{BCSDF}}(w_i, \omega_i, \omega_o)$
  $w_i' \leftarrow \sqrt{w_i^2 + \bar{W}_T^2}$
  $\bar{W}' \leftarrow \sqrt{\bar{W}^2 + \bar{W}_T^2}$
  $L_{indirect} \leftarrow T \cdot$ **Intensity**$(l_i) \cdot \cos^2 \theta_i \cdot \tilde{g_f} \cdot \left(f^{\text{dielectric}}_{\text{BCSDF}}(w_i', \omega_i, \omega_o) + f_{\text{back}}(\bar{W}')\right)$
  $L_o \leftarrow L_o + d \cdot L_{direct} + (1-d) \cdot L_{indirect}$
end for

// Generate illumination maps for a hair volume and for all lights
GenerateMaps:
for all lights l_i **do**
  GenerateMap$(n_x, n_y, n_z, light, hair)$
end for

// Generate an illumination map of $n_x \cdot n_y \cdot n_z$ voxels
GenerateMap$(n_x, n_y, n_z, light, hair)$**:**
// Align the map to the light source
// Its extent is based on the bounding box of the hair object
$bbox \leftarrow$**GetOrientedBBox**$(light, hair)$
$map \leftarrow$**MakeMap**$(bbox, n_x, n_y, n_z)$
// Generate relevant light samples according to the oriented bounding box of the hair volume
$\{s_i\} \leftarrow$**GenerateLightSamples**$(bbox, light)$
for all samples $s \in \{s_i\}$ **do**
  $r \leftarrow$**GenerateRay**(s)
  // Trace ray through bounding box and update maps
  UpdateTransmittanceMap(r)
  UpdateSpreadMap(r)
  UpdateDirectFractionMap(r)
end for

InterpolateTransmittance(p, l_i)**:**
For a given light source l_i the transmittance at a point p is estimated from the pre-computed transmittance map using trilinear filtering.

InterpolateSpread(p, l_i)**:**
For a given light source l_i the spread at a point p is estimated from the pre-computed spread map using trilinear filtering.

InterpolateDirectFraction(p, l_i)**:**
For a given light source l_i the fraction of direct illumination at a point p is estimated from a pre-computed map using trilinear filtering.

UpdateTransmittanceMap(r**):**
Update the transmittance map according to the transmittance along a ray sample r.

UpdateSpreadMap(r**):**
Update the spread map according to the spread along a ray sample r.

UpdateDirectFractionMap(r**):**
Update the direct visibility map according to the visibility along a ray sample r.

Algorithm 3 Pseudo code for section 4.9.2 For notation see Fig. 4.25.

RadianceEstimationWithLOD:
for all segments s_i **do**
  $m_i \leftarrow VisibilityMeasure(s_i)$
end for
for all segments s_i**:** $m_i > 0$ **do**
  $s_s \leftarrow Succ(s_i)$
  $s_p \leftarrow Pred(s_i)$
  if s_s **has been estimated or** s_p **has been estimated then**
    if $Random() > \beta * m_i$ **then**
      if s_s **has been estimated and** s_p **has been estimated then**
        $v_s \leftarrow SuccVertex(s_i)$
        $v_p \leftarrow PredVertex(s_i)$
        $tmp \leftarrow \frac{GetEstimate(v_s)+GetEstimate(v_r)}{2}$
        $SetEstimate(v_s, tmp)$
        $SetEstimate(v_r, tmp)$
      end if
      if s_s **has been estimated and** s_p **has not been estimated then**
        $SetEstimate(v_p, GetEstimate(v_s))$
      end if
      if s_s **has not been estimated and** s_p **has been estimated then**
        $SetEstimate(v_s, GetEstimate(v_p))$
      end if
    else
      $Estimate(s_i)$
    end if
  else
    $Estimate(s_i)$
  end if
end for

Estimate(s_i):

$v_s \leftarrow SuccVertex(s_i)$
$v_p \leftarrow PredVertex(s_i)$
$p \leftarrow \frac{v_s+v_p}{2}$
$L_o \leftarrow DensityEstimation(p)$
if (s_s) **has been estimated then**
  $SetEstimate(v_s, \frac{L_o+GetEstimate(v_s)}{2})$
end if
if (s_s) **has not been estimated then**
  $SetEstimate(v_s, L_o)$
end if
if (s_p) **has been estimated then**
  $SetEstimate(v_p, \frac{L_o+GetEstimate(v_p)}{2})$
end if
if (s_p) **has not been estimated then**
  $SetEstimate(v_p, L_o)$
end if

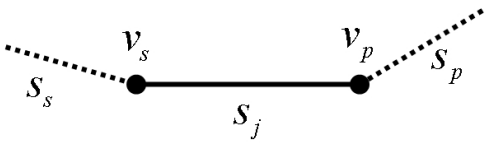

Fig. 4.25: Notation for Alg. 3. A fiber is represented by a chain of oriented segments. Considering a segment s_j which is defined by its starting point v_p and its endpoint v_s. s_j is connected to the segments s_p and s_s, respectively.

4.12 Results

4.12.1 Comparison of Results: Path Tracing vs Approximations

This section compares further rendering results to validate the visual quality of the ray-based approximation (cf. Sec. 4.9) and the “double scattering” approximation (cf. Sec. 4.10) against unbiased path tracing.

Fig. 4.26: A blond hairstyle illuminated with four directional light sources. Comparison of results obtained with: path tracing (reference) (top left), ray-based global illumination (bottom left), "double scattering" approximation using maps (middle right), "double scattering" approximation with ray shooting (middle left), single scattering only (top right).

Fig. 4.27: A blond hairstyle illuminated with four directional light sources. Comparison of results obtained with: path tracing (reference) (top left), ray-based global illumination (bottom left), "double scattering" approximation using maps (middle right), "double scattering" approximation with ray shooting (middle left), single scattering only (top right).

Fig. 4.28: A blond hairstyle illuminated with four directional light sources. Comparison of results obtained with: path tracing (reference) (top left), ray-based global illumination (bottom left), "double scattering" approximation using maps (middle right), "double scattering" approximation with ray shooting (middle left), single scattering only (top right).

Fig. 4.29: A blond hairstyle (model by Paris et al. [48], ca. 88000 hair strands) illuminated with three directional light sources. Comparison of results obtained with: path tracing (reference) (top left), ray-based global illumination (top right), "double scattering" approximation using maps (bottom left), single scattering only (bottom right).

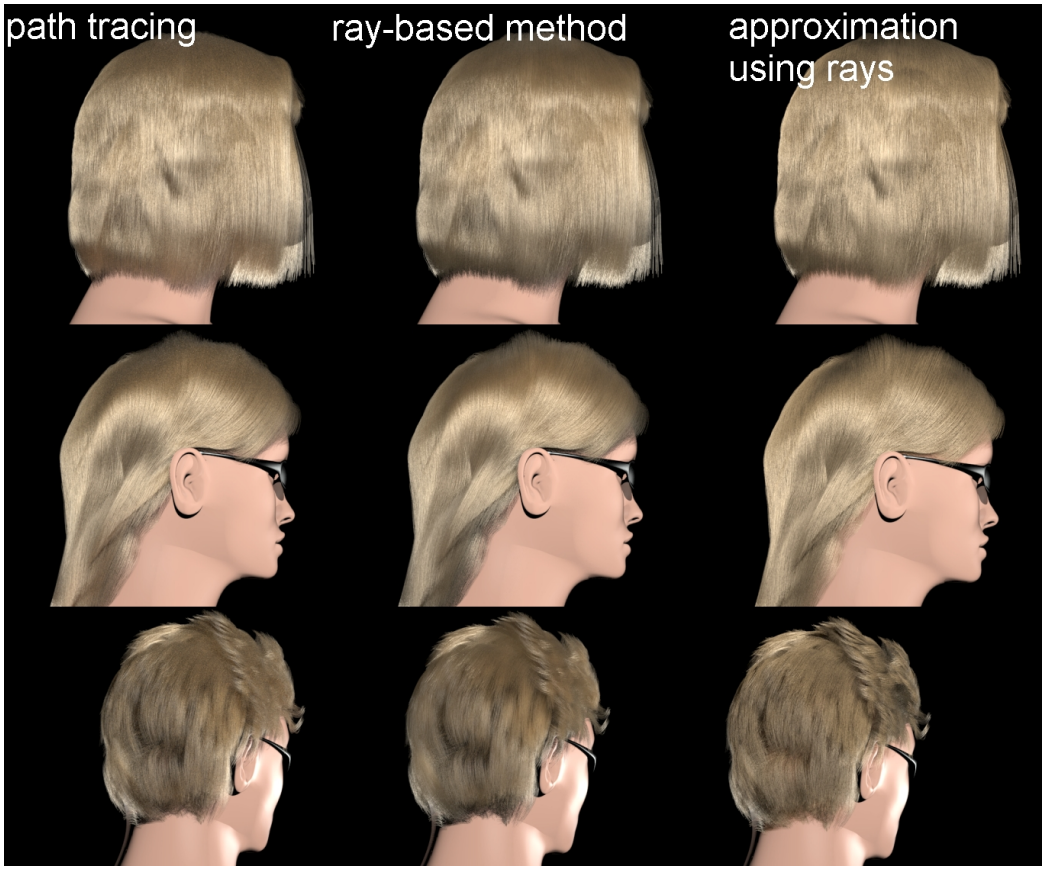

Fig. 4.30: Various hairstyles rendered using different approaches.

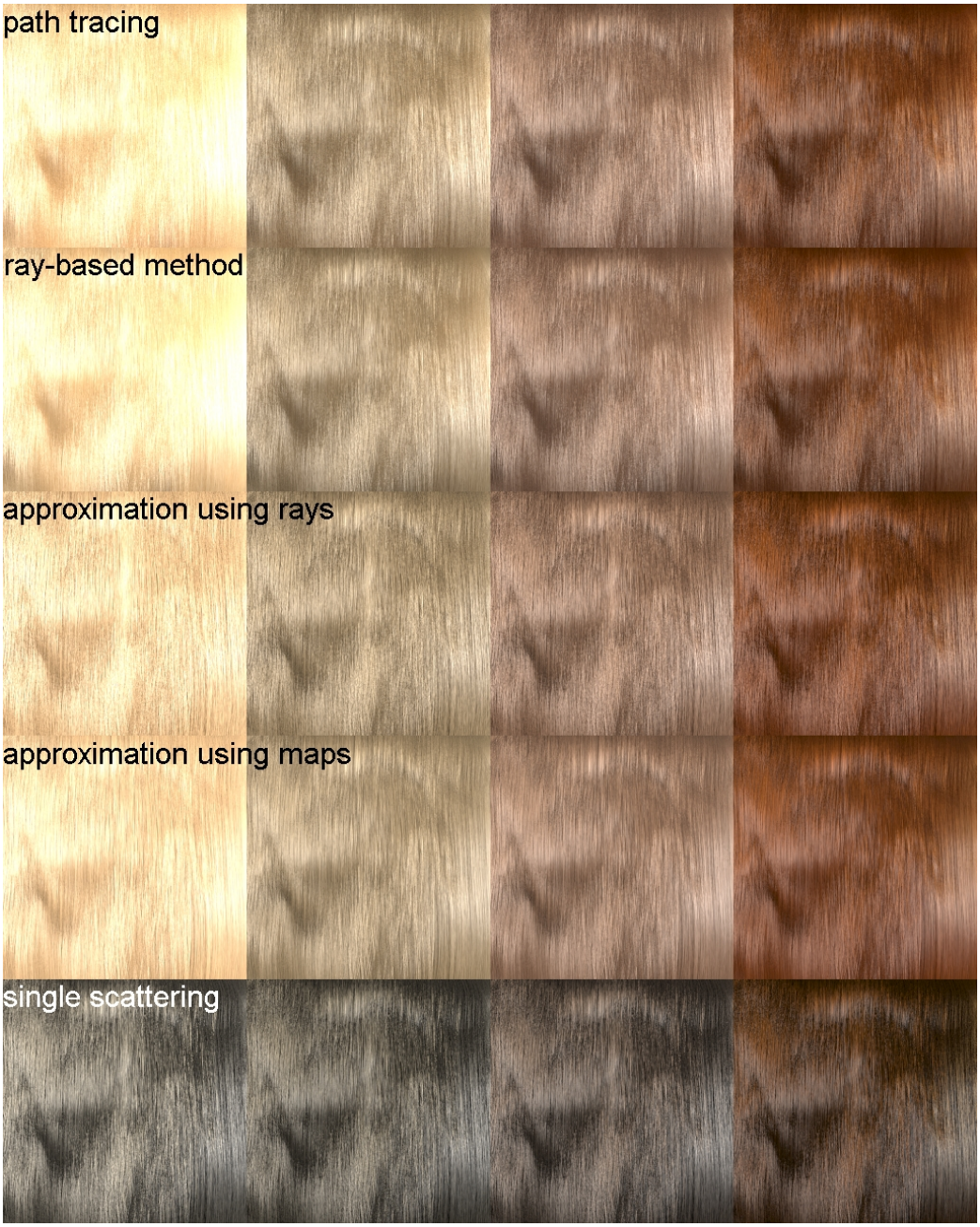

Fig. 4.31: Comparison of various hair colors, rendered using the model presented in section 3.10.2 with the following relative absorption coefficients (from left to right): $(8.6, 20.0, 42.9)cm^{-1}$; $(42.9, 57.1, 85.7)cm^{-1}$—which is typical for light blond hair; $(57.1, 85.7, 114.3)cm^{-1}$; $(85.7, 171.4, 342.9)cm^{-1}$. Please note the qualitative accordance of direct and global illumination with the measurement shown in Fig. 4.1.

4.12.2 Results of the Ray-Based Approximation

To exemplarily show the influence of different parameter settings for the ray-based approximation discussed in section 4.9 this section includes further rendering results obtained with different settings. Moreover, we present an interesting example indicating that our approximation is able to reproduce subtle global illumination effects, such as color bleeding.

Fig. 4.32: Varying the total number of ray segments stored in the map: 2M ray segments (top left) rendered in 2700s, 0.5M samples (top right) rendered in 780s, 0.1M samples rendered in 280s (bottom left), 0.05M samples (bottom right). Each estimate is based on up to 4096 neighboring ray segments (maximum lookup radius was 1cm and $\alpha = \beta = 1$) and all images were originally rendered at 1024×1024 pixels. Note how the variance is noticeable ("blotches") if the map contains too few ray segments, if a radiance estimate is based only on a few photons.

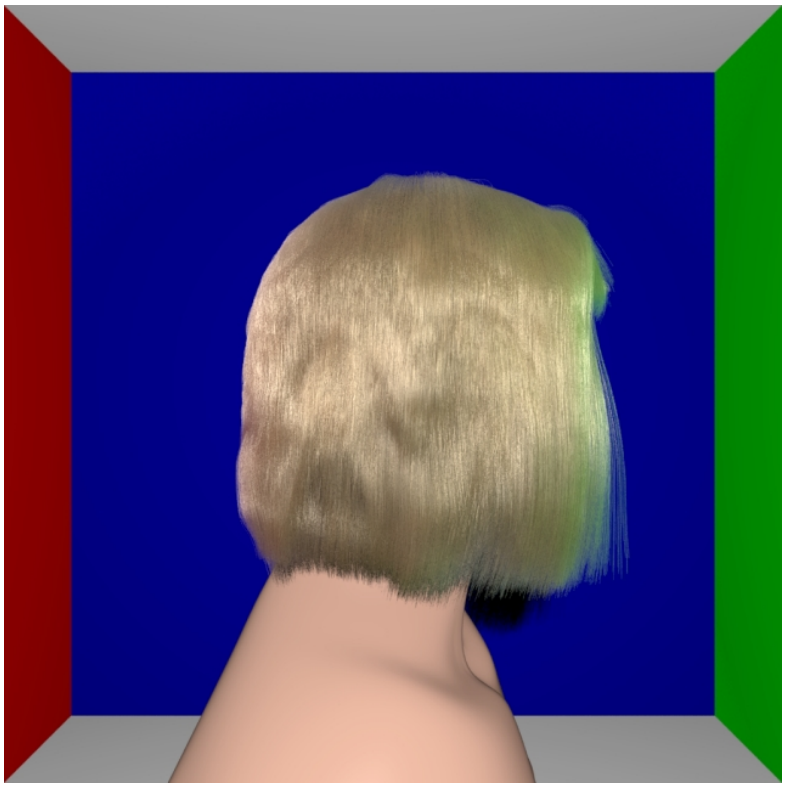

Fig. 4.33: Our ray-based approximation is able to accurately reproduce subtle global illumination effects, such as color bleeding.

4.12.3 Results of the "Double Scattering" Approximation

This section includes various examples proving that our "double scattering" approximation (cf. section 4.10) gives plausible results even in complicated cases. Moreover the influence of different parameter settings is shown by systematical comparisons.

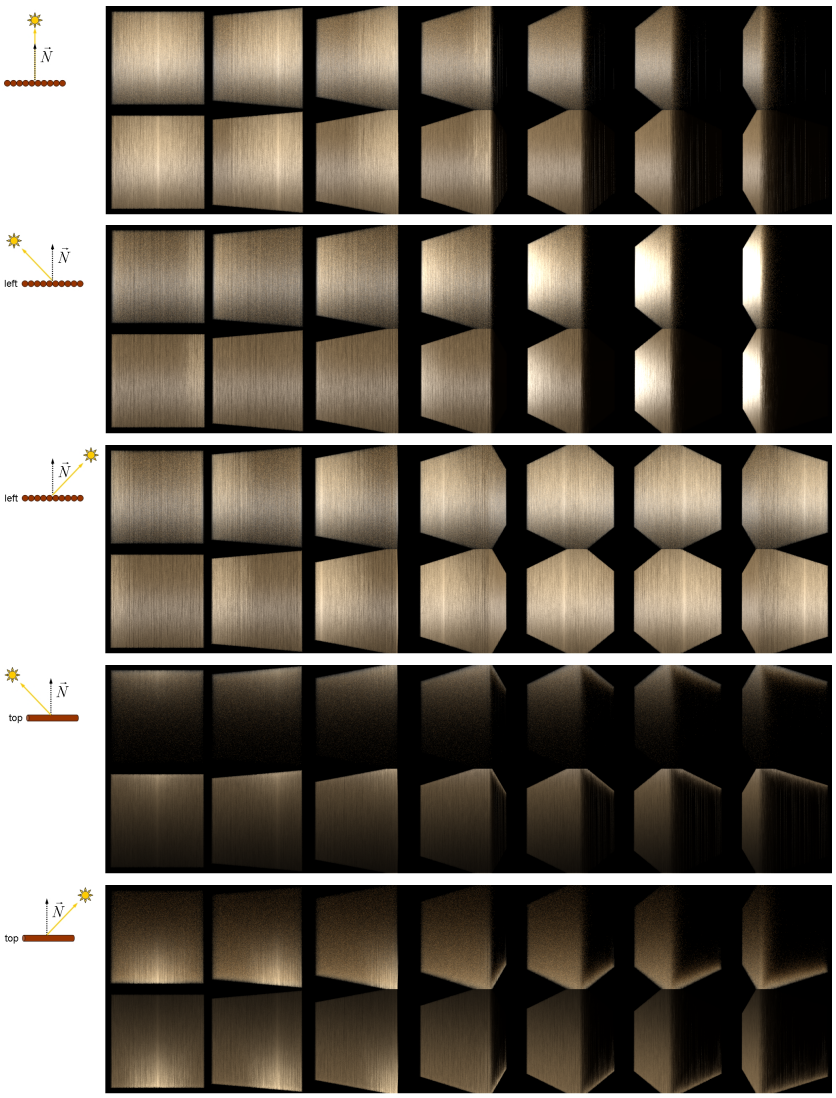

Fig. 4.34: Renderings of a cube (20 x 20 x 20 cm) consisting of 160000 vertically aligned fibers illuminated by one directional light (see the legend) and viewed from seven different perspectives. For each light setup the scene is rendered using costly path tracing (top row) and our "double scattering approximation" in conjunction with the ray shooting method (bottom row).

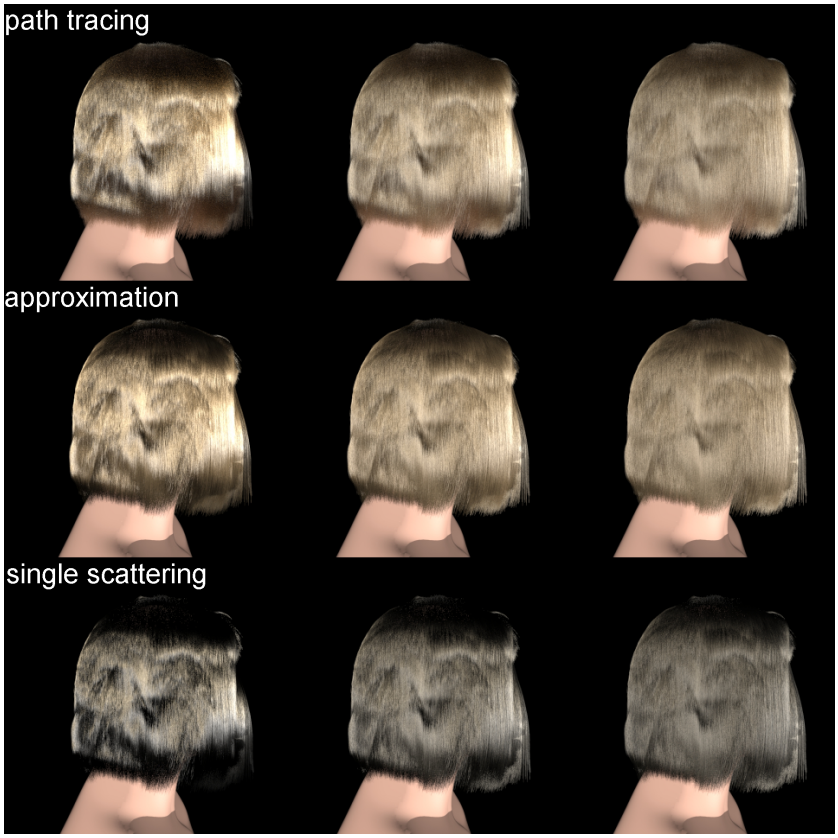

Fig. 4.35: The influence of the width of the scattering lobes on global (multiple fiber) backward scattering. A blond hairstyle is illuminated by three directional light sources. The longitudinal widths w_{R}, w_{TT}, w_{TRT} of the three strongest scattering components R,TT and TRT (see section 3.10.2 and [37]) increase from left to right: $w_{\mathrm{R}} = 4, w_{\mathrm{TT}} = 5, w_{\mathrm{TT}} = 7.5$; $w_{\mathrm{R}} = 8, w_{\mathrm{TT}} = 10, w_{\mathrm{TT}} = 15$; $w_{\mathrm{R}} = 16, w_{\mathrm{TT}} = 20, w_{\mathrm{TT}} = 30$. Note the similarity of the path traced reference solutions (top row) and the approximations (middle row).

Fig. 4.36: A blond hair style illuminated by four directional light sources. Due to **Top row:** single scattering only, opacity shadow map according to [29] using physically-based transmission coefficients. **Bottom row:**(from left to right): our approach, path tracing (reference).

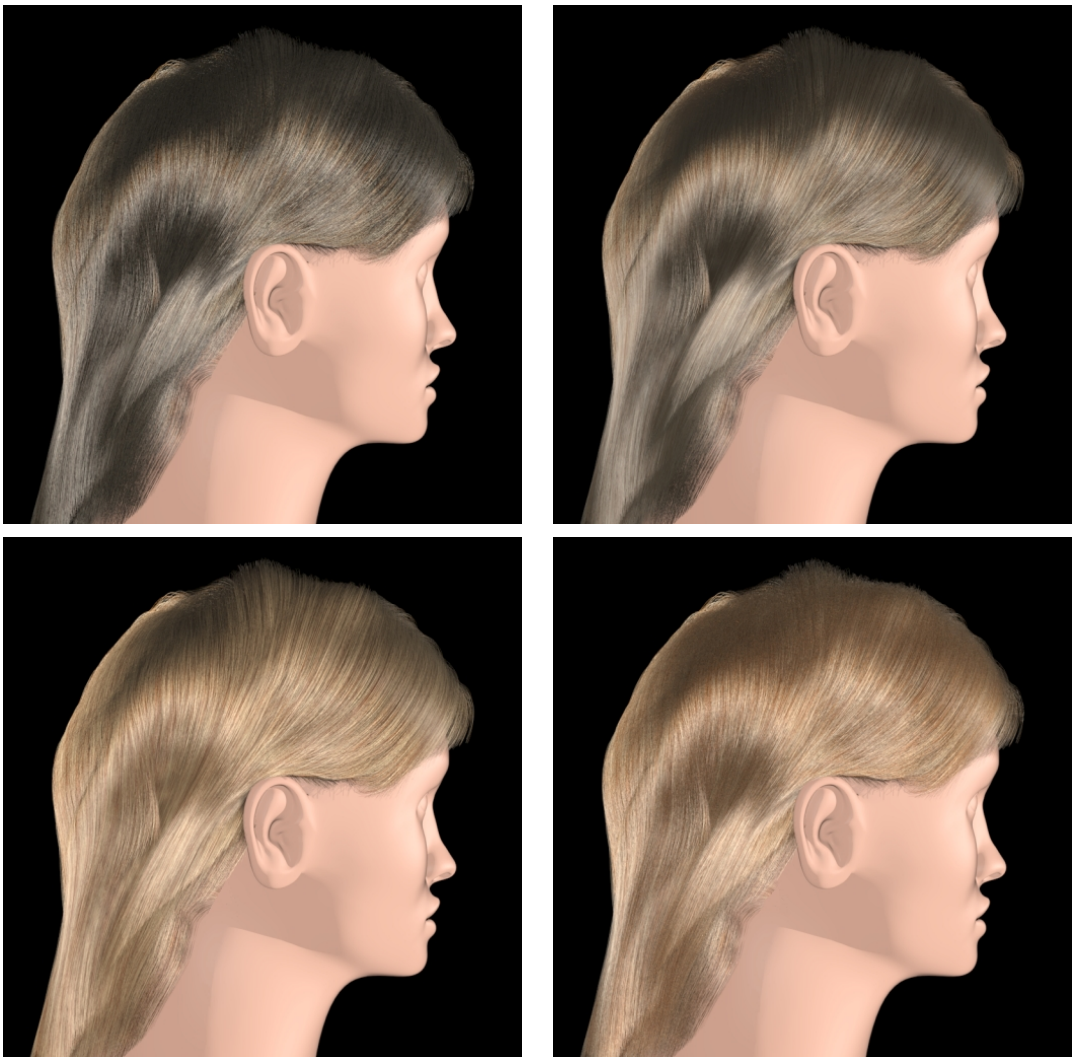

Fig. 4.37: A blond hair style with red highlights illuminated by four directional light sources. Due to inhomogeneous coloration our approximation does not perfectly match the original. **Top row**(from left to right): single scattering only, opacity shadow map according [29] using physically-based transmission coefficients. **Bottom row**(from left to right): our approach, path tracing (reference).

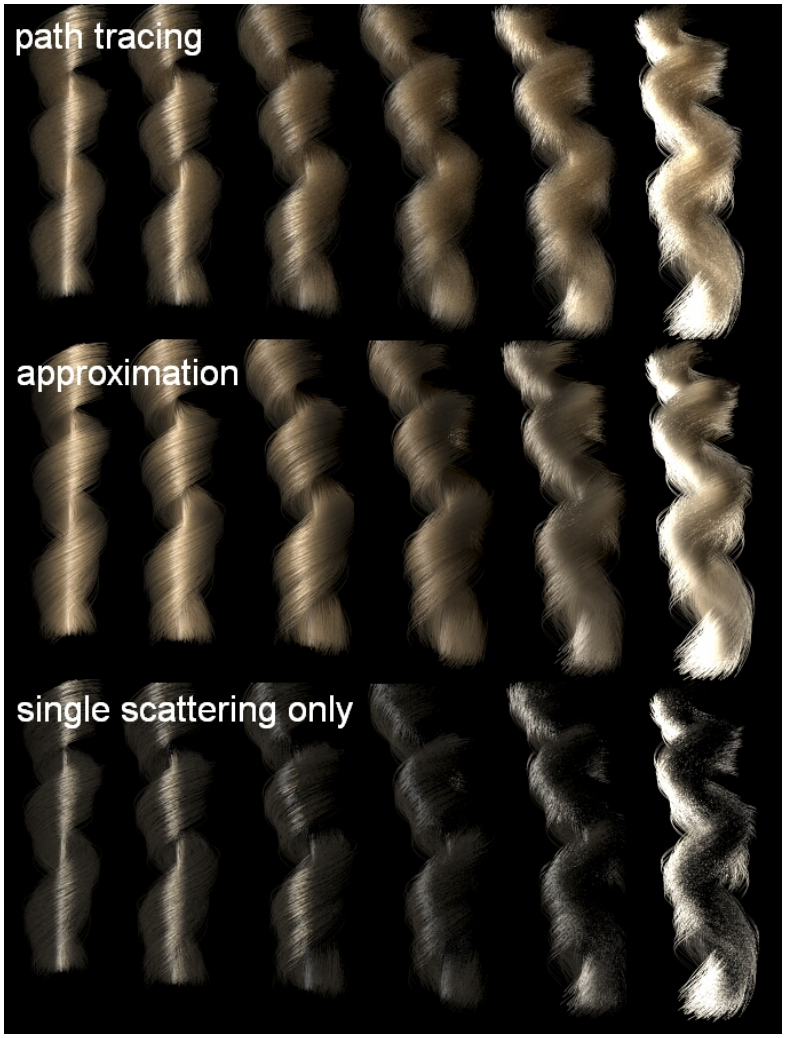

Fig. 4.38: A close-up of a small, relatively sparse strand of blond hairA close-up of a small, relatively sparse strand of blond hair (illuminated by one directional light source) viewed from different perspectives. Although this geometry clearly violates some of the assumptions of our simplified "double scattering" model, the results look still plausible.

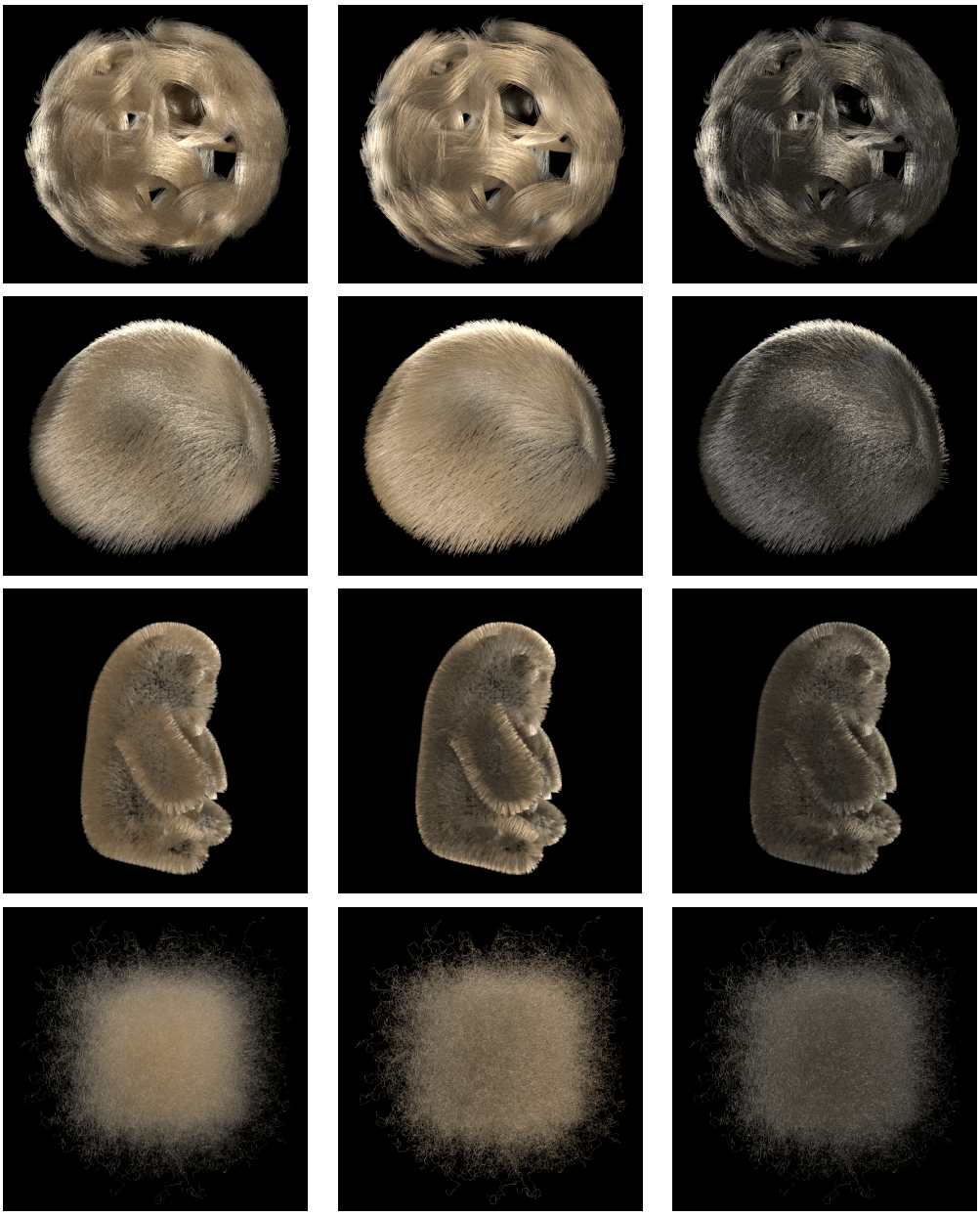

Fig. 4.39: Various renderings of complex hair geometries which clearly violate assumptions made for our "double scattering" approximation. Note that the results still look plausible without any parameter tweaking. All scenes are illuminated by four directional light sources. From top to bottom: several strands of hair arranged on a sphere (20000 fibers), short fur on a half sphere (40000 fibers), fur on the shape of a teddy model (580000 fibers), "filament soup" (10000 fibers). **Left column**: Path tracing reference, **Middle column**: our approximation using maps, **Right column**: single scattering only.

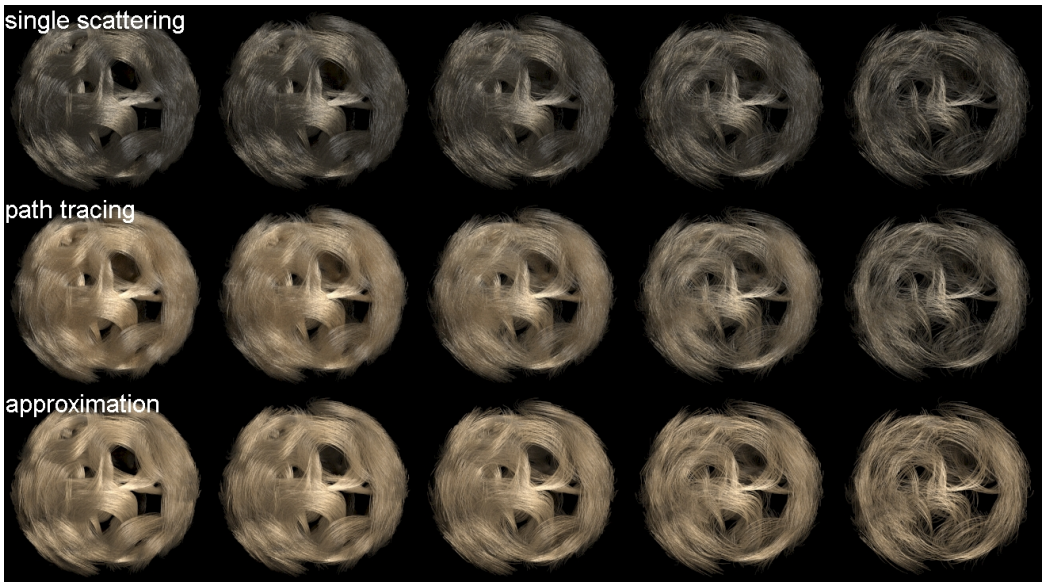

Fig. 4.40: In this case study of a blond "hair ball" illuminated by two directional front lights the bias introduced by our "double scattering" approximation is explored for various hair densities. The hair density decreases from left to right (the corresponding number of hair strands is: 25600, 13300, 5560, 3325, 1663 and 400). Comparison: **Top row:** single scattering only, **Middle row:** path tracing reference, **Bottom row:** "double scattering" approximation. Note how well the approximation matches the original rendering, if the hair is dense (leftmost image). Note also that the bias is not directly related to the actual hair density but to the distribution of indirect illumination a hair receives from surrounding fibers. For a sparse strand of hair indirect illumination plays no role and is systematically over estimated. However, only for extreme (unusual) cases noticeable bias is introduced by our approximation.

Fig. 4.41: Varying the number of ray samples used to create the illumination maps of the "double scattering" approximation. sources: 4M samples (top left), 1M samples (top right), 0.25M samples (bottom left), 0.125M samples (bottom right). For 4M and 1M samples virtually no sampling artifacts are noticeable.

Fig. 4.42: Varying the resolution (extent of a voxel) of the illumination maps of the "double scattering" approximation. sources: 0.25cm (top left), 0.5cm (top right), 1cm samples (bottom left), 2cm samples (bottom right). The bigger the extent of a voxel, the more fine detail are smoothed out.

5. TOWARDS INVERSE BCSDF RENDERING OF HUMAN HAIR

In the previous chapters a frame work for synthesis of photo-realistic hair images has been presented. In this chapter a discussion of the inverse problem will be made: Assuming that photographs of a hairstyle and the hair geometry are given, we are addressing the estimation of the BCSDF of the hair fibers. Such an image-based reconstruction can be valuable for many areas of application. For instance the ”hair color” of a real actor could be analyzed and transferred to a virtual character or the effects of cosmetic styling products (such as increased shininess) could be evaluated automatically.

The classification of a ”hair color” could also be enhanced. Since the appearance of hair strongly depends on lighting and hairstyle, substantial expert knowledge is needed to classify a hair color by hand (Fig.5.3). By using an image-based classification an even a much more subtle distinction would be possible.

In chapter 3 light scattering from fibers was discussed and a flexible physically-based BFSDF (inducing a BCSDF) for dielectric fibers was presented. It was shown that such a scattering function is a suitable basis to approximate scattering from human hair. However, accurately fitting this function to real hair would require costly fiber based measurements.

On the other hand, for many areas of application—such as the classification of a hair color—an accurate fiber based reconstruction of the BFSDF is not essential. Hence, if the main focus is not on accuracy, an image based approach roughly estimating the BCSDF can be a viable option. In order to make this problem feasible we extensively use the knowledge on the specific optical properties of human hair. Note that the ideas sketched in the following sections, as well as our ”proof-of-concept” implementation, should be seen only as a starting point for further substantial research.

5.1 Related Work

In the realm of inverse BRDF rendering several papers address the problem of recovering a Bidirectional Reflectance Distribution Function from images [36, 50]. Since a BRDF is a four dimensional function it can not be expected that few images contain enough information to reconstruct the BRDF for every pixel independently without any additional assumptions. In particular if the BRDF has narrow scattering lobes most samples will contain essentially no information that can be used to determine the shape of a lobe. Hence— to make the reconstruction problem feasible— often several assumptions, such as a spatially invariant BRDF or directional lighting, are assumed. Moreover, model-based fitting allows a rather sparse set of samples.

Although we do not want to estimate BRDFs our problem is quite similar. Based on a given set of images a bidirectional scattering function should be constructed. However, in contrast to existing methods not the overall scattering distribution, but scattering from individual fibers has to be recovered. Moreover, a hairstyle is usually a very complex, discontinuous shape. Although recently two techniques for roughly reconstructing hairstyles from images [48, 65] were presented, it cannot be expected that the reconstructed geometry closely matches the original hairstyle. One reason is that simplified scattering models were used in the reconstruction process and that single hair fibers cannot be resolved properly in the input images. However, due to the anisotropic nature of the BCSDF for human hair a proper knowledge about the hairstyle (the hair geometry the reconstruction is based on) is crucial.

5.2 Key Ideas of our Approach

In the following a first attempt for image-based BCSDF reconstruction for human hair will be outlined. Although the general approach is closely related to existing techniques in the realm of inverse rendering of Bidirectional Surface Reflection Distribution Functions, many special issues arise in the context of hair.

The basic idea of the method is to chose a viable set of image samples (representing the exitant radiance for a known perspective) and to estimate the parame-

ters of a model-based BCSDF using an analysis-by-synthesis loop. Since hundreds or even thousands of iterations have to be performed to obtain a final result each iteration step has to be carefully optimized to achieve acceptable computing times. This means also that an analysis-by-synthesis optimization can be performed only on a restricted set of well chosen samples extracted from the input images.

An image-based reconstruction of the BCSDF should provide a reasonable model-based fit of the data. Ideally such a fit should also estimate the actual optical properties of a fiber. However, since the physically-based scattering model used for fitting has many degrees of freedom and since it is based on approximations it can not be guaranteed that the real properties can be reconstructed, even if lighting and geometry are perfectly known. Moreover, it is clearly impossible to resolve scattering details on a fiber level and the highly non-linear nature of the problem complicates the search for an optimal fit. In practice, the photograph will be somewhat different even from an image rendered using adequate optical parameters.

For our implementation we assumed that:

- lighting (ideally directional lights) and observer are given,
- that the hair properties are spatially constant and that
- each region of the fiber geometry is known with a certain confidence.

The ”geometry confidence” should conveniently reflect the accuracy of the geometrical representation and is motivated by the fact that slight variations in the geometry may have a substantial impact on scattering. Moreover, it is very likely that the given geometry does not perfectly match the original on a strand level.

In the following we will sketch a method for estimating the BCSDF of human hair using the physically-based model $f_{\text{BCSDF}}^{\text{dielectric}}$ introduced in chapter 3. The process of reconstruction consists of several passes. In a first step the given images are analyzed with respect to geometry and lighting to extract reasonable samples. In order to filter out unreliable data we used some heuristics to limit the reconstruction to pixels corresponding to geometry that can reasonably be expected to be accurate, to identify regions in the original photograph which are suitable for parameter fitting. In this context regions of dense hair volumes, with a distinctive

alignment of fibers and without shadowing, are favored. Based on these criteria and the original confidence for geometry a heuristic parameter is computed which characterizes the viability of each image pixel for further considerations. Note that a dense hair volume is important to make sure that only hair (but no back ground) is visible and locally coherent fibers allow for an efficient estimation of the scattering distribution. We use the fact that for parallel fibers average backscattering from a "hair patch" due to direct illumination is very similar to backscattering from an individual fiber. However, self-shadowing effects may bias the results and have therefore to be taken into account.

In addition, a practicable approximation of global illumination effects is crucial and only possible by using a simplified approach, such as our approximation presented in section 4.10, which is based on locally coherent clusters. By averaging information of pixels of similar lighting and perspective a set of samples is computed from reliable pixels. In this context the standard deviation of the underlying pixels is analyzed to obtain an additional measure for the quality of a sample. In our implementation the averaging process is restricted to rectangular screen areas, hence neighboring pixels. However, other more flexible strategies might yield better results.

Having a set of samples, we pick out those samples which are suitable for fitting our scattering model. Recalling section 3.10.2 we will restrict ourselves to the two backward scattering highlights (R and TRT). The main reason is that only these two backscattering lobes substantially contribute to direct scattering from dense hair volumes. In contrast the TT-mode contributes only, when hair is lit from behind and if the hairstyle is sparse. Since this case is rare and would require an extremely accurate knowledge of the underlying hairstyle we neglect samples with substantial forward scattering.

Our analytical model has several parameters which have to be fitted. There are optical material properties such as absorption and index of refraction, longitudinal parameters like longitudinal widths and shifts of the scattering lobes and azimuthal features like azimuthal widths of the lobes and the eccentricity. Since it is nearly impossible to resolve fine azimuthal scattering detail of a fiber we propose a hierarchical multi-level fit to avoid undesirable fitting results. Gener-

ally, longitudinal properties causing stable, distinctive features are fitted first and azimuthal parameters are plausibly fitted in a second pass.

Summing-up our work flow includes the following steps:

Step 1: Analyze images and extract samples based on geometry and lighting. In this context heuristics are used to estimate the quality of a sample.

Step 2: Classify these samples with respect to the scattering model (e.g. positions of the highlights) and chose well distributed and reliable samples for the fit.

Step 3: Estimate initial parameter settings with a rough educated guess. For all longitudinal parameters typical values from literature [37] are used. The absorption is roughly estimated from the ratio of indirect and direct illumination based on samples which are likely to exhibit only little direct illumination and samples from the specular cone. In this context a higher ratio means less absorbtion.

Step 4: Fit longitudinal shifts of the highlights by taking into account that only the TRT-highlight is colored and the R-highlight is white.

Step 5: Estimate longitudinal widths of the highlights (colored TRT-highlight, white R-highlight), the absorption coefficients and optional scaling factors. The effective index of refraction is set to a fixed value of 1.55 (c.f. [57]). Since glints—the strong intensity peaks of the TRT component—can not be resolved properly, all TRT-scattering is averaged with respect to azimuth.

Step 6: Fit all longitudinal and material parameters at once for fine tuning. Again all TRT-scattering is averaged with respect to azimuth.

Step 7: Adjust azimuthal parameters based on the azimuthal variance of samples. If the variance is big, the hair is very likely to have an elliptic cross section. As a initial guess a circular cross section is assumed.

Step 8: Set all parameters for the TT-component based on the final results for the R- and TRT lobe. We use the ”natural relationships” proposed by Marschner et al. [37] (Table 1) to determine the shift, the width and an optional scaling

of this lobe. However, since the impact of slight modifications of the TT-components on the overall ”hair color” is rather small, we think that such a heuristic is acceptable.

It turned out that the most crucial part of our approach is a proper implementation of the fitting procedure, especially if many degrees of freedom are fitted at once. However, due to our hierarchical approach which is adapted to the analytical scattering model results are quite stable with respect to slight modifications of the initial guess. Moreover, parameter constraints help to limiting the search region to a reasonable range. Note that for light colored hair multiple fiber scattering is essential for the ”hair color” and must not be neglected. To approximate this effect we use a variant of the method introduced in section 4.10.

5.3 Discussion of Results and Future Work

Our current implementation was tested only with ”synthetic” photographs (renderings), where illumination, perspective and geometry was perfectly known. Figure 5.1 shows exemplary results obtained with this method. First a series of ”synthetic photographs” of a scene with varying lighting and fixed ”hair color” was rendered (Fig. 5.2). Then one out of these images was used as an input for a model-based fit of the BCSDF. Finally, all images were re-rendered using the reconstructed properties and compared to the originals. Note how well all images match the originals, although only a single image served as an input and even though the geometry is neither optimized to give many distinctive samples nor unrealistically dense or even. Moreover, the longitudinal properties and the absorption coefficients are relatively close to the original, in particular if the estimate is based on a bigger set of samples. Some results of the fit—including computing times—are given in Tab. 5.1. Although further investigations are needed, these preliminary results indicate that this implementation is basically able to reproduce the appearance of dark hair from images in a reasonable time-frame.

However, our existing tests cover only some aspects of the reconstruction problem. For example it would make sense to analyze the influence of noise on the reconstructed BCSDF (stability) and also how multiple fiber scattering biasses

the result. Also principal limitations of our approach have to be considered, such as:

- using a simplified BCSDF-model to approximate the actual BCSDF of hair
- using a rough approximation for multiple fiber scattering
- guessing azimuthal and TT-parameters
- neglecting local self shadowing

Finally, our implementation bases on local optimization techniques which raises a questions about the optimality of a fit.

Even though we believe that our method is a suitable basis for BCSDF reconstruction we actually did not prove that this approach can solve the reconstruction problem, if it is applied to photographs of real hair under more realistic conditions. Although the results are promising, only future research on real hair can show if the basic idea is viable. In this context various other, more practical issues, have to be studied further and a lot of technical problems have to be solved.

Also recent work on the separation of direct and indirect scattering components could substantially improve our approach, in particular for light colored hair. Nayar et al. [45] showed that local and global illumination effects can be separated if high frequency structured light is used for scene illumination. Based on such a separation the parameter fitting could be performed exclusively on the direct illumination component. Moreover, the ratio of the direct and indirect illumination could be used to roughly estimate the absorption coefficient, since light colored hair (with only little absorption) tends to exhibit relatively stronger multiple fiber scattering than dark hair.

Finally other interesting questions could be addressed, such as if it is possible to fit spatially varying ”hair colors” in parallel, e.g. by using machine learning algorithms. Moreover—since the actual scattering is closely related to the geometry of the underlying hairstyle— a combined image-based reconstruction of both, the hairstyle and the BCSDF, could improve existing techniques for image based hairstyle reconstruction [48, 65].

Tab. 5.1: Estimated values for parameters of the BCSDF presented in section 3.10.2. From left to right: original values, estimation based on the best 64 samples, best 128 samples and best 256 samples. The corresponding computing times were 31s,49s and 81s, respectively (3 GHz Pentium 4). Renderings unsing the estimated values are compared in Fig. 5.1.

parameter	original	64 samples	128 samples	256 samples
$\Delta\theta_{\mathrm{R}}$	-6.75	-7.0	-7.1	-7.4
$\Delta\theta_{\mathrm{TT}}$	3.2	3.5	3.3	3.6
$\Delta\theta_{\mathrm{TRT}}$	8.9	10.6	9.3	10.2
w_{R}^{θ}	11.3	13.2	13.6	13.2
w_{TT}^{θ}	5.5	6.3	6.5	6.2
$w_{\mathrm{TRT}}^{\theta}$	21.4	23.8	24.7	23.0
$scale_{\mathrm{R}}$	5108	3534	4317	4328
$scale_{\mathrm{TT}}$	4597	3534	4318	4328
$scale_{\mathrm{TRT}}$	4086	3534	4319	4330
$\sigma(r,g,b)$ in cm^{-1}	(145,239,353)	(112,190,299)	(151,233,337)	(139,211,298)
k_d (r,g,b)	(20.2,6.0,1.7)	(19.3,5.4,1.3)	(19.3,5.4,1.3)	(19.3,5.4,1,3)

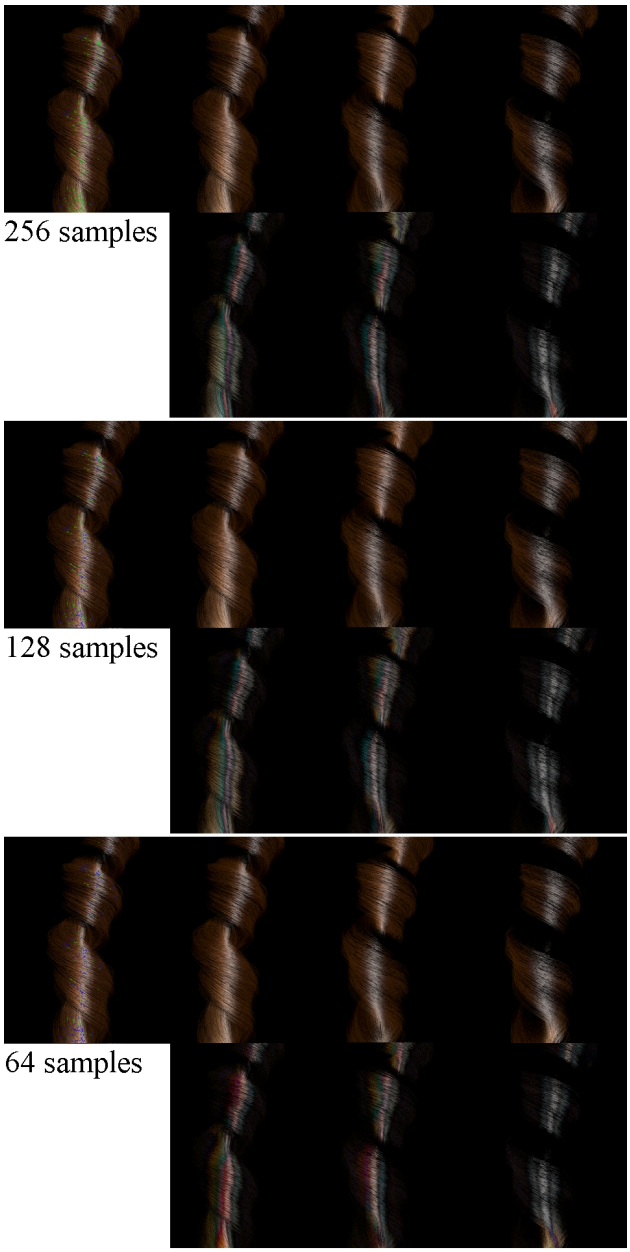

Fig. 5.1: Several tests for reconstructing the BCSDF of a ”synthetic photograph” (rendering). The leftmost image of Fig. 5.2 was used as an input and the reconstruction was performed based on 256 samples (top row), 128 samples (middle row) and 64 samples (bottom row). For each row the leftmost image shows the distribution of automatically chosen samples. Blue dots indicate potential sample candidates (after the first sample extraction step) and the green dots are the samples finally chosen for the fit. To estimate the quality of the BCSDF estimation the parameters of the fit were used to re-render the all reference images shown in Fig. 5.2. The absolute differences (for red, green and blue; multiplied by a factor of five) to the originals (Fig. 5.2) are shown right below these results for each image. The actual results of the BCSDF fit can be found in Tab. 5.1.

Fig. 5.2: Three reference renderings showing a tress consisting of about 2000 strands. The scene is illuminated by a single point light source and for hair rendering the parametric scattering model presented in section 3.10.2 was used with the parameter settings given in Tab. 5.1 (first column). The leftmost rendering served as an input image for the BCSDF reconstruction and the other images are used to verify the reconstructed hair color (see also Fig. 5.1).

Fig. 5.3: A typical chart for the classification of hair colors (`http://www.wiggoddess.com/images/cooleurocolors1.jpg`).

6. CONCLUSION AND FUTURE WORK

6.1 Conclusion

Starting with a phenomenological introduction to light scattering from fibers in chapter 2 we introduced the Bidirectional Fiber Scattering Distribution Function (BFSDF), a novel fundamental framework for light scattering from fibers (chapter 3). Similar to the role of the BSSRDF for surface scattering functions, the BFSDF can be seen as a general approach for scattering from filaments which is suitable for deriving approximations in a canonic and systematic way. Based on this theoretical foundation, approximations for many important special cases were derived allowing for efficient and accurate rendering of fiber assemblies, such as hair or fur. In this context the Bidirectional Curve Scattering Distribution Function (BCSDF), a far-field approximation of the BFSDF, was introduced in section 3.7 and physically-based analytical BFSDF/BCSDF models for human hair and other kinds of fibers were derived.

In chapter 4 we discussed the problem of fiber rendering and presented novel efficient rendering techniques accounting for all prominent effects of local and global illumination. These methods offer a wide range of application, from physically-plausible interactive rendering to extremely accurate results. In contrast to existing methods no additional ad-hoc material parameters, but only the BFSDF of a fiber is needed.

Finally, using a BCSDF model for human hair we made a first step towards image-based BFSDF reconstruction, where optical properties of a single strand are estimated from ”synthetic photographs” (renderings) a full hairstyle (chapter 5).

6.2 Outlook

In this thesis we introduced a novel fundamental framework for light scattering from fibers, the Bidirectional Fiber Scattering Distribution Function (BFSDF). However, although this framework proved to be useful for many theoretical considerations, more practical issues have to be investigated further. In particular compression techniques (similar to the BSSRDF/BSDF) and further analytical BFSDF/BCSDF models are needed to reduce memory costs. Moreover, efficient strategies for measuring light scattering from fibers have to be developed. In particular measurements of human hair are needed to validate and improve the scattering models discussed in sections 2.1.3 and 3.10.2.

Although we believe that this work covers most relevant aspects of fiber rendering we still have to investigate the potential of our techniques for real time rendering using graphics hardware. In particular the ”double scattering” approximation (section 4.10) is well suited to be implemented on current hardware. Realizing such an implementation will be one topic of our future work.

Another possible direction would be image-based BCSDF reconstruction. Although a first attempt was presented, more substantial research on this topic is needed. This includes testing on real hair strands, as well as validating the results against fiber based measurements. Moreover—since the actual scattering is closely related to the geometry of the underlying hairstyle— a combined image-based reconstruction of both, the hairstyle and the BCSDF, could be an interesting option.

7. APPENDIX

7.1 Basics of Optics

7.1.1 Law of Reflection

Light is known to behave in a very predictable manner. If a ray of light could be observed approaching and reflecting off an ideal smooth interface (surface) between two dielectric media, then the path of the light as it reflects would follow a predictable law known as the law of reflection. The relationship between incident direction ω_i and the direction of the reflected light ω_r is illustrated in Fig. 7.1 Left. The reflected ray lies in the plane defined by the surface normal and the incident ray and the angle of reflection γ_r (between surface normal and ω_r) equals the angle of incidence γ_i (between surface normal and ω_i). Note that the radiance of the reflected ray may differ from the incident radiance (see also 7.1.3).

7.1.2 Snell's Law

A ray of light approaching a smooth interface (surface) between two dielectric media splits into two parts: a reflected ray which can be computed according to the law of reflection and a refracted ray (Fig. 7.1 Left). Its direction ω_t can be computed from the incident direction ω_i and the indexes of refraction of the two media. In the following the index of refraction of the initial medium is denoted n_1 and the second refractive index n_2, respectively. Supposing the angle of incidence is given by γ_i and the angle of refraction is γ_t, the following equation holds:

$$\sin\gamma_i = \frac{n_1}{n_2}\sin\gamma_t. \tag{7.1}$$

Again, as for the law of reflection, the refracted ray lies in the plane defined by the surface normal and ω_i.

7.1.3 Fresnel Equations

If light gets reflected/refracted at an interface (surface) between two dielectric media the fraction of the intensity being reflected/transmitted can be computed from the Fresnel equations. This fraction depends on the incident direction, the indexes of refraction of the two media and the polarization of the incident light.

In the following we will use the notation introduced in section 7.1.1 and section 7.1.2 (see also Fig. 7.1 Left).

Then for light being perpendicularly polarized with respect to the surface the reflection coefficient $F_\perp$ (the ratio between reflected and incident intensity) is given by:

$$\mathrm{F}_\perp = \frac{\sin(\gamma_t - \gamma_i)}{\sin(\gamma_t + \gamma_i)} \tag{7.2}$$

For the reflection coefficient $F_\parallel$ for light being polarized in the plane defined by the surface holds:

$$\mathrm{F}_\parallel = \frac{\tan(\gamma_t - \gamma_i)}{\tan(\gamma_t + \gamma_i)} \tag{7.3}$$

The corresponding transmission coefficients $T_\perp$ and $T_\parallel$ can be computed from the reflection coefficients:

$$\begin{aligned} \mathrm{T}_\perp &= 1 - \mathrm{F}_\perp \\ \mathrm{T}_\parallel &= 1 - \mathrm{F}_\parallel. \end{aligned} \tag{7.4}$$

For rendering the actual polarization of light is commonly neglected. Instead it is commonly assumed that the light can be approximated by a mixture of parallel and perpendicularly polarized light (equal portions). With this assumption for the effective reflection and transmission coefficients (F and T) hold:

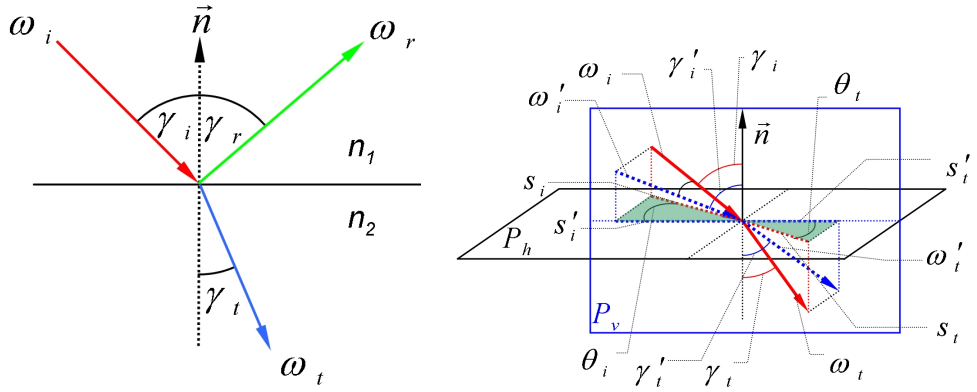

Fig. 7.1: **Left:** Reflection and refraction at an interface between two dielectric media: The law of reflection and Snell's law. **Right:** Analyzing refraction in 2D from projections onto the plane P_v: Bravais's law.

$$\mathrm{F} = \frac{\mathrm{F}_\perp + \mathrm{F}_\parallel}{2} \tag{7.5}$$

and

$$\mathrm{T} = 1 - \mathrm{F}. \tag{7.6}$$

7.2 Bravais's Law

A cylindrical fiber is formed by sweeping a cross section along an axis. Bravais has shown that the optics of a three dimensional cylindrical fiber may be reduced to the 2D analysis of the optics of its cross section. The incident direction is first projected into the cross-section plane and then reflected and refracted in two dimensions. However, to be able to still use Snells law of refraction in two dimensions, the index of refraction must be changed as a function of the angle of incidence.

In the following we will give a detailed derivation of Bravais law. It is very instructive to understand the relationships between original and projected properties — the reason why Snells law can be applied to 2D. Note that — although

the final result is correct — the proof given by [37] is not accurate. In Fig. 7.1 Right, the optical path of a ray reflected at an interface between two optical media (denoted P_h) is shown. Light from direction ω_i forming an angle of incidence γ_i with the surface normal is refracted to a direction ω_t with a corresponding angle γ_t. To reduce this problem from three two two dimensions these two directions are first projected to a vertical plane P_v perpendicular to P_h. In the following the projected directions will be denoted ω_i' and ω_t' and the corresponding projected angles γ_i' and γ_t', respectively. Moreover, θ_i is the incident inclination with respect to P_v and the inclination of the refracted ray is denoted θ_t.

Let the refractive index of the initial optical medium be n_1 and the index of the second medium n_2. With $n = n_2/n_1$ holds according to Snell's Law (see Sec. 7.1.2):

$$\sin\gamma_i = n \sin\gamma_t. \tag{7.7}$$

Then, according to Fig. 7.1 Right the following geometrical relation holds:

$$s_i = n s_t. \tag{7.8}$$

Using the definitions:

$$\begin{aligned}
l_i &= \|\omega_i\|, \\
l_i' &= \|\omega_i'\|, \\
c_i &= l_i \cos\gamma_i, \\
c_i' &= l_i' \cos\gamma_i', \\
s_i &= l_i \sin\gamma_i, \\
s_i' &= l_i' \sin\gamma_i' \\
l_t &= \|\omega_t\|, \\
l_t' &= \|\omega_t'\|, \\
c_t &= l_t \cos\gamma_t,
\end{aligned}$$

$$\begin{aligned} c'_t &= l'_t \cos\gamma'_t, \\ s_t &= t_t \sin\gamma_t, \\ s'_t &= l'_t \sin\gamma'_t \end{aligned} \tag{7.9}$$

with the theorem of Pythagoras one finds the following equations:

$$\begin{aligned} l_i^2 &= c_i^2 + s_i^2, \\ l'^2_i &= c'^2_i + s'^2_i, \\ l_t^2 &= c_t^2 + s_t^2, \\ l'^2_t &= c'^2_t + s'^2_t. \end{aligned} \tag{7.10}$$

With (7.9) and:

$$\begin{aligned} l'_i &= l_i \cos\theta_i, \\ l'_t &= l_t \cos\theta_t \end{aligned} \tag{7.11}$$

moreover holds:

$$\begin{aligned} s'_i &= l \cos\theta_i \sin\gamma'_i, \\ s'_t &= l \cos\theta_t \sin\gamma'_t. \end{aligned} \tag{7.12}$$

Assuming w.l.o.g. $l_i = l_t = 1$ and combining the results of (7.10), (7.11) and (7.12) yields:

$$\begin{aligned} \cos^2\theta_i = \cos^2\theta_i \sin^2\gamma'_i + \cos^2\gamma_i \Rightarrow |\sin\gamma'_i| = \sqrt{1 - \frac{\cos\gamma_i}{\cos\theta_i}}, \\ \cos^2\theta_t = \cos^2\theta_t \sin^2\gamma'_t + \cos^2\gamma_t \Rightarrow |\sin\gamma'_t| = \sqrt{1 - \frac{\cos\gamma_t}{\cos\theta_t}}. \end{aligned} \tag{7.13}$$

Our goal is to find a modified index of refraction n' for which Snells law holds for the projected angles:

$$\sin\gamma_i' = n' \sin\gamma_t'. \tag{7.14}$$

Using (7.10), (7.12) and (7.13) yields the following equations:

$$\begin{aligned}
\sqrt{1-\frac{\cos\gamma_i}{\cos\theta_i}} &= n'\sqrt{1-\frac{\cos\gamma_t}{\cos\theta_t}} \\
\Rightarrow 1-\frac{\cos\gamma_i}{\cos\theta_i} &= n'^2\left(1-\frac{\cos\gamma_t}{\cos\theta_t}\right) \\
\Rightarrow 1-\frac{\cos\gamma_i}{\cos\theta_i} &= n'^2\left(1-\frac{1-\sin^2\gamma_i/n^2}{\cos^2\theta_t}\right) \\
\Rightarrow 1-\frac{\cos\gamma_i}{\cos\theta_i} &= n'^2\left(1-\frac{1-\sin^2\gamma_i/n^2}{\cos^2\theta_i {n_2'}^2/n_2^2}\right) \\
\Rightarrow n' &= \frac{\sqrt{n_2^2-\sin^2\theta_i}}{\cos\theta_i}.
\end{aligned} \tag{7.15}$$

This is the final result for the modified index of refraction which is used to compute scattering from projected properties in 2D.

We now derive an expression for the inclination of the scattered light θ_t based on the relative index of refraction n'/n. From the similarity of the triangles shown in Fig. 7.1 Right (indicated by green color) and with $s_t = s_i/n$ follows:

$$s_t' = \frac{s_i'}{n}. \tag{7.16}$$

Inserting (7.12) to (7.16) one obtains:

$$\cos\theta_t \sin\gamma_t' = \frac{\cos\theta_i \sin\gamma_i'}{n}$$

$$\begin{aligned} \Rightarrow \cos\theta_t \frac{\sin\gamma_i'}{n'} &= \frac{\cos\theta_i \sin\gamma_i'}{n} \\ \Rightarrow \cos\theta_t &= \frac{n'}{n}\cos\theta_i. \end{aligned} \tag{7.17}$$

Alternatively, θ_t can be expressed without using the modified index of refraction n' by:

$$\sin\theta_t = \frac{\sin\theta_i}{n}. \tag{7.18}$$

7.3 Transformation of the BFSDF Rendering Integral

In section 3.5 the BFSDF and its corresponding rendering integral was introduced with respect to two different sets of variables:

- set one: $\alpha_i, \beta_i, \xi_i, s_i, \alpha_o, \beta_o, \xi_o, s_o$
- set two: $\varphi_i, \theta_i, h_i, s_i, \varphi_o, \theta_o, h_o, s_o$.

The second set of variables can be written in terms of the first set. According to section 3.4 the transformation between one set into the other are given by the following equations:

$$\begin{aligned} \beta &= \arccos\left(\cos\theta\sqrt{1-h^2}\right), \\ \xi &= \begin{cases} \varphi + \arcsin h & 0 \le \varphi + \arcsin h < 2\pi \\ 2\pi + \varphi + \arcsin h & \varphi + \arcsin h < 0 \\ \varphi + \arcsin h - 2\pi & \varphi + \arcsin h \ge 2\pi \end{cases}, \\ \alpha &= \begin{cases} \arccos\left(\frac{\sin\theta}{\sqrt{1-(1-h^2)\cos^2\theta}}\right), & h \le 0, \\ 2\pi - \arccos\left(\frac{\sin\theta}{\sqrt{1-(1-h^2)\cos^2\theta}}\right), & h > 0. \end{cases} \end{aligned} \tag{7.19}$$

Using the first set of variables the rendering integral thus becomes:

$$L_o(s_o,\xi_o,\alpha_o,\beta_o) = \int_{-\infty}^{+\infty}\int_0^{2\pi}\int_0^{2\pi}\int_0^{\pi/2} f_{\mathrm{BFSDF}}(\Delta s,\xi_i,\alpha_i,\beta_i,\xi_o,\alpha_o,\beta_o)\,L_i(s_i,\xi_i,\alpha_i,\beta_i) \sin\beta_i\cos\beta_i\,\mathrm{d}\beta_i\,\mathrm{d}\alpha_i\,\mathrm{d}\xi_i\,\mathrm{d}\Delta s \tag{7.20}$$

with $\Delta s = s_o - s_i$. In the following we will will show how this integral can be rewritten with respect to the second set.
According to (7.19) for the product $\sin\beta_i\cos\beta_i$ which is part of the integrand holds:

$$\sin\beta_i\cos\beta_i = \sqrt{1-\cos^2\theta_i\left(1-h_i^2\right)}\cos\theta\sqrt{1-h^2} \tag{7.21}$$

The remaining rest $f_{\mathrm{BFSDF}}(\Delta s,\xi_i,\alpha_i,\beta_i,\xi_o,\alpha_o,\beta_o)\,L_i(s_i,\xi_i,\alpha_i,\beta_i)\mathrm{d}\beta_i\,\mathrm{d}\alpha_i\,\mathrm{d}\xi_i\,\mathrm{d}\Delta s$ can be transformed by using the Jacobian J of the transformation between variable set one and two and by reparameterizing the integration:

$$L_o(s_o,h_o,\varphi_o,\theta_o) = \int_{-\infty}^{+\infty}\int_{-1}^{1}\int_0^{2\pi}\int_{-\pi/2}^{\pi/2} J f_{\mathrm{BFSDF}}(\Delta s,h_i,\varphi_i,\theta_i,h_o,\varphi_o,\theta_o) L_i(s_i,h_i,\varphi_i,\theta_i)\sqrt{1-\cos^2\theta_i\left(1-h_i^2\right)}\sqrt{1-h_i^2}\cos\theta_i \mathrm{d}\theta_i\,\mathrm{d}\varphi_i\,\mathrm{d}h_i\,\mathrm{d}\Delta s. \tag{7.22}$$

With:

$$J = \left|\frac{\partial(\xi_i,\alpha_i,\beta_i)}{\partial(h_i,\varphi_i,\theta_i)}\right| = \frac{-h\cos^2\theta}{\sqrt{1-h^2}\sqrt{\frac{h^2\cos^2\theta-\cos^2\theta+1-\sin^2\theta}{h^2\cos^2\theta-\cos^2\theta+1}}\left(h^2\cos^2\theta-\cos^2\theta+1\right)} \tag{7.23}$$

and after simplification one finally obtains the result presented in section 3.5:

$$L_o(s_o,h_o,\varphi_o,\theta_o) = \int_{-\infty}^{+\infty}\int_{-1}^{1}\int_{0}^{2\pi}\int_{-\pi/2}^{\pi/2} f_{\mathrm{BFSDF}}(\Delta s,h_i,\varphi_i,\theta_i,h_o,\varphi_o,\theta_o) \cos^2\theta_i L_i(s_i,h_i,\varphi_i,\theta_i)\,\mathrm{d}\theta_i\,\mathrm{d}\varphi_i\,\mathrm{d}h_i\,\mathrm{d}\Delta s. \quad (7.24)$$

7.4 Derivation of Marschner et al.

In this section we will show that the far-field scattering model proposed by [37] is a special BCSDF, which can be derived from the underlying BFSDF. According to section 3.9.2 this BFSDF (generating the model of [37]) is given by:

$$f_{\mathrm{BFSDF}}^{\mathrm{generatorMarschner}} = f_{\mathrm{BFSDF}}^{\mathrm{R}} + f_{\mathrm{BFSDF}}^{\mathrm{TT}} + f_{\mathrm{BFSDF}}^{\mathrm{TRT}} \quad (7.25)$$

with:

$$\begin{aligned} f_{\mathrm{BFSDF}}^{\mathrm{R}} &= \frac{a^{\mathrm{R}}(\theta_d,h_i)}{\cos^2\theta_d}\delta(h_o+h_i)g(\theta_o+\theta_i-\Delta\theta_{\mathrm{R}},w_{\mathrm{R}}^{\theta})\delta(\Delta s)\delta(\varphi_i-\lambda_{\varphi}{}^{\mathrm{R}}) \\ &= \frac{a^{\mathrm{R}}(\theta_d,h_i)}{\cos^2\theta_d}\delta(h_o+h_i)g(\theta_o+\theta_i-\Delta\theta_{\mathrm{R}},w_{\mathrm{R}}^{\theta})\delta(\Delta s) \\ &\quad \delta(\varphi_i-\varphi_o-2\arcsin h_o), \end{aligned} \quad (7.26)$$

$$\begin{aligned} f_{\mathrm{BFSDF}}^{\mathrm{TT}} &= \frac{a^{\mathrm{TT}}(\theta_d,h_i)}{\cos^2\theta_d}\delta(h_o+h_i)g(\theta_o+\theta_i-\Delta\theta_{\mathrm{TT}},w_{\mathrm{TT}}^{\theta})\delta(\Delta s)\delta(\varphi_i-\lambda_{\varphi}{}^{\mathrm{TT}}) \\ &= \frac{a^{\mathrm{TT}}(\theta_d,h_i)}{\cos^2\theta_d}\delta(h_o+h_i)g(\theta_o+\theta_i-\Delta\theta_{\mathrm{TT}},w_{\mathrm{TT}}^{\theta})\delta(\Delta s) \\ &\quad \delta(\varphi_i-\varphi_o-M[\pi+2\arcsin h_o-2\arcsin(h_o/n')]) \end{aligned} \quad (7.27)$$

and

$$f_{\mathrm{BFSDF}}^{\mathrm{TRT}} = \frac{a^{\mathrm{TRT}}(\theta_d,h_i)}{\cos^2\theta_d}\delta(h_o+h_i)g(\theta_o+\theta_i-\Delta\theta_{\mathrm{TRT}},w_{\mathrm{TRT}}^{\theta})\delta(\Delta s)\delta(\varphi_i-\lambda_{\varphi}{}^{\mathrm{TRT}})$$

$$= \frac{a^{\mathrm{TRT}}(\theta_d, h_i)}{\cos^2\theta_d}\delta(h_o+h_i)g(\theta_o+\theta_i-\Delta\theta_{\mathrm{TRT}}, w^{\theta}_{\mathrm{TRT}})\delta(\Delta s)$$
$$\delta(\varphi_i-\varphi_o-4\arcsin(h_o/n')+2\arcsin h_o). \tag{7.28}$$

Using the definition of the BCSDF (3.55) one obtains:

$$\begin{aligned}
f^{\mathrm{generatorMarschner}}_{\mathrm{BCSDF}} &= \frac{1}{2}\int_{-1}^{1}\int_{-1}^{1}\int_{-\infty}^{\infty} f^{\mathrm{generatorMarschner}}_{\mathrm{BFSDF}}\,\mathrm{d}\Delta s\,\mathrm{d}h_o\,\mathrm{d}h_i \\
&= \frac{1}{2}\int_{-1}^{1}\int_{-1}^{1}\int_{-\infty}^{\infty} f^{\mathrm{R}}_{\mathrm{BFSDF}}\mathrm{d}\Delta s\,\mathrm{d}h_i\,\mathrm{d}h_o \\
&\quad +\frac{1}{2}\int_{-1}^{1}\int_{-1}^{1}\int_{-\infty}^{\infty} f^{\mathrm{TT}}_{\mathrm{BFSDF}}\mathrm{d}\Delta s\,\mathrm{d}h_i\,\mathrm{d}h_o \\
&\quad +\frac{1}{2}\int_{-1}^{1}\int_{-1}^{1}\int_{-\infty}^{\infty} f^{\mathrm{TRT}}_{\mathrm{BFSDF}}\mathrm{d}\Delta s\,\mathrm{d}h_i\,\mathrm{d}h_o \\
&= f^{\mathrm{R}}_{\mathrm{BCSDF}} + f^{\mathrm{TT}}_{\mathrm{BCSDF}} + f^{\mathrm{TRT}}_{\mathrm{BCSDF}}
\end{aligned} \tag{7.29}$$

Hence, the BCSDF can be decomposed into three expressions, one for each scattering component. Note that to perform the integration of $f^{\mathrm{generatorMarschner}}_{\mathrm{BFSDF}}$ with respect to h_o symbolically, the following rule for integrals over δ-distributions has to be applied:

$$\int_{-1}^{1} f^G(h_o)\delta(\varphi_i-\lambda^G_{\varphi}(h_o))\mathrm{d}h_o = \sum_{i=0}^{n-1}\frac{f^G(h^i_o)}{|\frac{\mathrm{d}\lambda^G_{\varphi}}{\mathrm{d}h_o}(h^i_o)|} \tag{7.30}$$

with $G \in \{\mathrm{R}, \mathrm{TT}, \mathrm{TRT}\}$. Here the expression $f^G(h_o)$ subsumes all factors depending on h_o (except the δ-function itself) and h^i_o denotes the i-th root of the expression $\varphi_i - \lambda^G_{\varphi}(h_o)$. Note that the expression $1/(2|\frac{\mathrm{d}\lambda^G_{\varphi}}{\mathrm{d}h_o}(h^i_o)|)$ matches the ray density factor introduced by Marschner et al. In contrast to [37] we do not need any awkward motivation to add this factor. In our case it simply falls out from the BCSDF approximation.

Based on (7.30) and the decomposition of the BCSDF integral (7.29) we now derive an analytical expression for far-field scattering from a circular dielectric fiber.

7.4.1 R-component

Performing the integration of $f_{\mathrm{BFSDF}}^{\mathrm{R}}$ with respect to Δs is trivial, since there is only one factor containing Δs, namely $\delta(\Delta s)$. Hence, one obtains:

$$\int_{-\infty}^{\infty} f_{\mathrm{BFSDF}}^{\mathrm{R}} \mathrm{d}\Delta s = \frac{a^{\mathrm{R}}(\theta_d, h_i)}{\cos^2\theta_d}\delta(h_o+h_i)g(\theta_o+\theta_i-\Delta\theta_{\mathrm{R}}, w_{\mathrm{R}}^{\theta})\delta(\varphi_i-{\lambda_{\varphi}}^{\mathrm{R}}). \tag{7.31}$$

Due to the factor $\delta(h_i+h_o)$ in (7.26) a further integration with respect to h_i just means a replacement of all h_i by $-h_o$, thus:

$$\int_{-1}^{1}\int_{-\infty}^{\infty} f_{\mathrm{BFSDF}}^{\mathrm{R}} \mathrm{d}\Delta s\,\mathrm{d}h_i = \frac{a^{\mathrm{R}}(\theta_d, -h_o)}{\cos^2\theta_d} g(\theta_o+\theta_i-\Delta\theta_{\mathrm{R}}, w_{\mathrm{R}}^{\theta})\delta(\varphi_i-{\lambda_{\varphi}}^{\mathrm{R}}). \tag{7.32}$$

This expression has to be integrated with respect to h_o to finally obtain $f_{\mathrm{BCSDF}}^{\mathrm{R}}$. Hence — according to (7.30) — one has to solve for the roots of the expression $\varphi_i-\varphi_o-2\arcsin h_o$ and insert it to $\frac{\mathrm{d}\lambda_{\varphi}^{\mathrm{R}}}{\mathrm{d}h_o}(h_o)$.

For the R-component there is exactly one root h_o^1:

$$h_o^1 = -\sin\phi/2 \tag{7.33}$$

with $\phi = M[\varphi_o-\varphi_i]$.

Moreover, for the derivative of $\mathrm{d}\lambda_{\varphi}^{\mathrm{R}}$ with respect to h_o holds:

$$\frac{\mathrm{d}\lambda_{\varphi}^{\mathrm{R}}}{\mathrm{d}h_o}(h_o) = -\frac{2}{\sqrt{1-h_o^2}}. \tag{7.34}$$

Inserting h_o^1 yields:

$$\begin{aligned}\frac{\mathrm{d}\lambda_\varphi^{\mathrm{R}}}{\mathrm{d}h_o}(h_o^1) &= -\frac{2}{\sqrt{1-h_o^{1\,2}}} \\ &= \frac{2}{\cos(\phi/2)}\end{aligned} \tag{7.35}$$

Hence, applying the rule (7.30) and performing the integration with respect to h_o one finally obtains:

$$f_{\mathrm{BCSDF}}^{\mathrm{R}} = \frac{a^{\mathrm{R}}(\theta_d, \frac{\phi}{2})\cos(\frac{\phi}{2})g(\theta_o+\theta_i-\Delta\theta_{\mathrm{R}}, w_{\mathrm{R}}^{\theta})}{4\cos^2\theta_d}. \tag{7.36}$$

This result matches [37, equation 8] (for $p=0$ and inserting the ray density and attenuation factors).

7.4.2 TT-component

Again the integration of $f_{\mathrm{BFSDF}}^{\mathrm{TT}}$ with respect to Δs and h_i is trivial:

$$\begin{aligned}\int_{-1}^{1}\int_{-\infty}^{\infty} f_{\mathrm{BFSDF}}^{\mathrm{TT}}\mathrm{d}\Delta s\,\mathrm{d}h_i &= \frac{a^{\mathrm{TT}}(\theta_d,-h_o)}{\cos^2\theta_d} g(\theta_o+\theta_i-\Delta\theta_{\mathrm{TT}}, w_{\mathrm{TT}}^{\theta}) \\ &\quad \delta(\varphi_i-\varphi_o-M[\pi+2\arcsin h_o-2\arcsin(h_o/n')])\end{aligned} \tag{7.37}$$

According to (7.30) one has to solve:

$$\varphi_i-\varphi_o-M[\pi+2\arcsin h_o-2\arcsin(h_o/n')]=0. \tag{7.38}$$

The only real root is given by:

$$h_o^1 = \frac{-\cos(\phi/2)\, n\, (\sin(\phi/2)+n)^{-1}}{\sqrt{-\frac{2\sin(\phi/2)n+n^2+1}{-2\sin(\phi/2)n-n^2-1+(\cos(\phi/2))^2}}}. \tag{7.39}$$

Inserting this root to

$$\frac{\mathrm{d}\lambda_\varphi^{\mathrm{TT}}}{\mathrm{d}h_o}(h_o) = 2\frac{\sqrt{1-h_o^2}-\sqrt{n'^2-h_o^2}}{\sqrt{1-h_o^2}\sqrt{n'^2-h_o^2}} \tag{7.40}$$

yields:

$$\frac{\mathrm{d}\lambda_\varphi^{\mathrm{TT}}}{\mathrm{d}h_o}(h_o^1) = 2\frac{n\sqrt{\frac{-\cos^2(\phi/2)+1+2\sin(\phi/2)n+n^2}{2\sin(\phi/2)n+n^2+1}}-\sqrt{-\frac{\cos^2(\phi/2)n^2-n^2-1-2\sin(\phi/2)n}{2\sin(\phi/2)n+n^2+1}}}{n\sqrt{-\frac{\cos^2(\phi/2)n^2-n^2-1-2\sin(\phi/2)n}{2\sin(\phi/2)n+n^2+1}}\sqrt{\frac{-\cos^2(\phi/2)+1+2\sin(\phi/2)n+n^2}{2\sin(\phi/2)n+n^2+1}}}. \tag{7.41}$$

Putting all together, applying (7.30) and performing the integration according to (7.29) one gets the final result for the TT-lobe:

$$f_{\mathrm{BCSDF}}^{\mathrm{TT}} = \frac{a^{\mathrm{TT}}(\theta_d, h_o^1)\, g(\theta_o+\theta_i-\Delta\theta_{\mathrm{TT}}, w_{\mathrm{TT}}^\theta)}{2\left|\frac{\mathrm{d}\lambda_\varphi^{\mathrm{TT}}}{\mathrm{d}h_o}(h_o^1)\right|\cos^2\theta_d}. \tag{7.42}$$

This result again matches [37, equation 8] (for $p=1$ and inserting the ray density and attenuation factors).

Note that Marschner et al. actually do not compute the roots of (7.38). Instead, this equation is approximated by a third order polynomial (see [37, equation 10]).

7.4.3 TRT-component

Integrating $f_{\mathrm{BFSDF}}^{\mathrm{TT}}$ with respect to Δs and h_i yields:

$$\int_{-1}^{1}\int_{-\infty}^{\infty} f_{\mathrm{BFSDF}}^{\mathrm{TRT}}\,\mathrm{d}\Delta s\,\mathrm{d}h_i = \frac{a^{\mathrm{TRT}}(\theta_d,-h_o)}{\cos^2\theta_d} g(\theta_o+\theta_i-\Delta\theta_{\mathrm{TRT}},w_{\mathrm{TRT}}^{\theta}) \delta(\varphi_i-\varphi_o-4\arcsin(h_o/n')+2\arcsin h_o) \quad (7.43)$$

Also the rest of the derivation follows the same scheme as for the RR and TT component.

According to (7.30) the following expression has to be solved for the roots:

$$\varphi_i-\varphi_o-(2\arcsin h_o-4\arcsin(h_o/n')). \quad (7.44)$$

This expression has either one or three real roots which can be — at least in principle — computed fully analytically. However, according to ([37, equation 10]) it is less costly to fit (7.44) by a third order polynomial. This is achieved by approximating Snell's law with the cubic polynomial which matches the value and derivative of the exact expression at $\pm\pi/2$:

$$\gamma_t' = \frac{3c\gamma_i'}{\pi} - \frac{4c\gamma_i'^3}{\pi^3} \quad (7.45)$$

with $c = 1/sin(1/n')$, $\gamma_i' = \arcsin h_i$. Since $h_i = -h_o$, $|\gamma'_i|$ is equal to $|\gamma'_o|$. Hence, one obtains:

$$\varphi_i-\varphi_o-(2\gamma_o'-4\arcsin\gamma_t') \quad (7.46)$$

where $\gamma_o' = \arcsin h_o$. Note that (7.46) does not explicitly depend on h_o. However, determining its real roots γ'^i_o the corresponding h_o^i can be computed using the equality $h_o^i = \sin(\gamma'^i_o)$. Similar to (7.44), (7.46) exhibits either one or three roots. Hence, a case differentiation is needed for $f_{\mathrm{BCSDF}}^{\mathrm{TRT}}$:

$$f_{\text{BCSDF}}^{\text{TRT}} = \begin{cases} \dfrac{a^{\text{TRT}}(\theta_d, h_o^1)\, g(\theta_o + \theta_i - \Delta\theta_{\text{TRT}}, w_{\text{TRT}}^{\theta})}{2\left|\frac{\mathrm{d}\lambda_{\varphi}^{\text{TRT}}}{\mathrm{d}h_o}(h_o^1)\right| \cos^2\theta_d}, & |\{h_o^i\}| = 1 \\ \displaystyle\sum_{i=1}^{3} \dfrac{a^{\text{TRT}}(\theta_d, h_o^i)\, g(\theta_o + \theta_i - \Delta\theta_{\text{TRT}}, w_{\text{TRT}}^{\theta})}{2\left|\frac{\mathrm{d}\lambda_{\varphi}^{\text{TRT}}}{\mathrm{d}h_o}(h_o^i)\right| \cos^2\theta_d} & |\{h_o^i\}| = 3 \end{cases} \tag{7.47}$$

This result matches [37, equation 8] (for $p = 2$ and inserting the ray density and attenuation factors).

BIBLIOGRAPHY

[1] N. Adabala, N. Magnenat-Thalmann, and G. Fei. Real-time visualization of woven textiles. In J. C. Guerri, P. A, and C. A. Palau, editors, *Publication of EUROSIS*, pages 502–508, 2003.

[2] C. L. Adler, J. A. Lock, and B. R. Stone. Rainbow scattering by a cylinder with a nearly elliptical cross section. *Optical Society of America*, 1998.

[3] C. L. Adler, J. A. Lock, B. R. Stone, and C. J. Garcia. High-order interior caustics produced in scattering of a diagonally incident plane wave by a circular cylinder. *Optical Society of America*, 14, 1996.

[4] C. L. Adler, D. Phipps, K. W. Saunders, J. K. Nash, and J. A. Lock. Supernumerary spacing of rainbows produced by an elliptical-cross-section cylinder. *Optical Society of America*, 2001.

[5] J. Arvo and D. Kirk. Particle transport and image synthesis. In *SIGGRAPH '90: Proceedings of the 17th annual conference on Computer graphics and interactive techniques*, pages 63–66, New York, NY, USA, 1990. ACM Press.

[6] D. Baraff and A. P. Witkin. Large steps in cloth simulation. In *Proceedings of SIGGRAPH 98*, Computer Graphics Proceedings, Annual Conference Series, pages 43–54, July 1998.

[7] F. Bertails, C. Ménier, and M.-P. Cani. A practical self-shadowing algorithm for interactive hair animation. In *Graphics Interface*, pages 71–78, 2005.

[8] E. Cerezo, F. Perez-Cazorla, X. Pueyo, F. Seron, and F. Sillion. A survey on participating media rendering techniques. *the Visual Computer*, 2005.

[9] K.-J. Choi and H.-S. Ko. Advanced topics on clothing simulation and animation. ACM SIGGRAPH 2005 Courses, 2005.

[10] K. J. Dana, B. van Ginneken, S. K. Nayar, and J. J. Koenderink. Reflectance and texture of real-world surfaces. In *IEEE Conference on Computer Vision and Pattern Recognition*, pages 151–157, 1997.

[11] K. Daubert, H. Lensch, W. Heidrich, and H.-P. Seidel. Efficient cloth modeling and rendering. In *Proceedings of EGRW '01*, pages 63–70, 2001.

[12] D. B. Goldman. Fake fur rendering. In *SIGGRAPH '97: Proceedings of the 24th annual conference on Computer graphics and interactive techniques*, pages 127–134, New York, NY, USA, 1997. ACM Press.

[13] E. Groller, R. T. Rau, and W. Strasser. Modeling and visualization of knitwear. *IEEE Transaction on Visualization and Computer Graphics*, 1(4):302–310, 1995.

[14] R. Gupta. *Interactive Hair Rendering*. PhD thesis, Faculté des Sciences Economiques et Sociales Université de Genève, 2007.

[15] R. Gupta and N. M. Thalmann. Scattering-based interactive hair rendering. In *Internatinal Conference on CAD/Graphics*, pages 489–494, 2005.

[16] M. Hadwiger, A. Kratz, C. Sigg, and K. Bühler. Gpu-accelerated deep shadow maps for direct volume rendering. In *Proceedings of Eurographics/SIGGRAPH Graphics Hardware 2006*, pages 49–52, 2006.

[17] V. Havran, J. Bittner, R. Herzog, and H.-P. Seidel. Ray maps for global illumination. In *Eurographics Symposium on Rendering*, pages 43–54, 2005.

[18] H. W. Jensen. Global illumination using photon maps. In *Proceedings of EGRW '96*, pages 21–30. Springer-Verlag, 1996.

[19] H. W. Jensen. *Realistic Image Synthesis Using Photon Mapping*. A. K. Peters, Natick, MA, 2001.

[20] H. W. Jensen. *Realistic Image Synthesis Using Photon Mapping*. A. K. Peters, Natick, MA, 2001.

[21] H. W. Jensen. A practical guide to global illumination using photon mapping. SIGGRAPH Course Notes CD-ROM, July 2002.

[22] H. W. Jensen and P. H. Christensen. Efficient simulation of light transport in scenes with participating media using photon maps. In *SIGGRAPH '98: Proceedings of the 25th annual conference on Computer graphics and interactive techniques*, pages 311–320, New York, NY, USA, 1998. ACM Press/Addison-Wesley Publishing Co.

[23] H. W. Jensen, S. R. Marschner, M. Levoy, and P. Hanrahan. A practical model for subsurface light transport. In *SIGGRAPH '01: Proceedings of the 28th annual conference on Computer graphics and interactive techniques*, pages 511–518, New York, NY, USA, 2001. ACM Press.

[24] J. T. Kajiya. The rendering equation. In *SIGGRAPH '86: Proceedings of the 13th annual conference on Computer graphics and interactive techniques*, pages 143–150, New York, NY, USA, 1986. ACM Press.

[25] J. T. Kajiya and T. L. Kay. Rendering fur with three dimensional textures. In *Proceedings of the 16th annual conference on Computer graphics and interactive techniques*, pages 271–280. ACM Press, 1989.

[26] J. Kautz and M. McCool. Interactive Rendering with Arbitrary BRDFs using Separable Approximations. In *Tenth Eurographics Workshop on Rendering*, pages 281–292, 1999.

[27] T.-Y. Kim. *Modeling, Rendering and Animating Human Hair*. PhD-Thesis in computer science, University of Southern California, December 2002.

[28] T.-Y. Kim and U. Neumann. Opacity shadow maps. In *Eurographics Rendering Workshop*, pages 177–182, 2001.

[29] T.-Y. Kim and U. Neumann. Opacity shadow maps. In *Proc. of Eurographics Workshop on Rendering*, pages 177–182, 2001.

[30] M. Koster, J. Haber, and H.-P. Seidel. Real-time rendering of human hair using programmable graphics hardware. In *Proceedings of the Computer Graphics International (CGI'04)*, pages 248–256, 2004.

[31] M. Lastra, C. Urena, J. Revelles, and R. Montes. A particle-path based method for Monte Carlo density estimation. In *Eurographics Workshop on Rendering*, pages 33–40, 2002.

[32] F. Lavignotte and M. Paulin. A new approach of density estimation for global illumination. *Journal of WSCG*, 2002.

[33] X. Liu, Y. Hu, J. Zhang, X. Tong, B. Guo, and H.-Y. Shum. Synthesis and Rendering of Bidirectional Texture Functions on Arbitrary Surfaces. *IEEE Transactions on Visualization and Computer Graphics*, 10(3):278–289, 2004.

[34] T. Lokovic and E. Veach. Deep shadow maps. In *SIGGRAPH '00: Proceedings of the 27th annual conference on Computer graphics and interactive techniques*, pages 385–392, New York, NY, USA, 2000. ACM Press/Addison-Wesley Publishing Co.

[35] R. I. Mark. Particle tracing methods in photorealistic image synthesis. In *CECSG 98, 2nd Central European Seminar on Computer Graphics*, pages 105–117, 1998.

[36] S. Marschner, S. Westin, E. Lafortune, and K. Torrance. Image-based brdf measurement, 2000.

[37] S. R. Marschner, H. W. Jensen, M. Cammarano, S. Worley, and P. Hanrahan. Light scattering from human hair fibers. *ACM Transactions on Graphics*, 22(3):780–791, 2003. SIGGRAPH 2003.

[38] W. Matusik, H. Pfister, A. Ngan, P. Beardsley, R. Ziegler, and L. McMillan. Image-based 3d photography using opacity hulls. In *SIGGRAPH '02: Proceedings of the 29th annual conference on Computer graphics and interactive techniques*, pages 427–437, New York, NY, USA, 2002. ACM Press.

[39] L. Mees, K. F. Ren, G. Grehan, and G. Gouesbet. Scattering of a Gaussian beam by an infinite cylinder with arbitrary location and arbitrary orientation: numerical results. *Optical Society of America*, 1998.

[40] T. Mertens, J. Kautz, P. Bekaert, and F. V. Reeth. A self-shadow algorithm for dynamic hair using density clustering. In *Eurographics Symposium on Rendering*, 2004.

[41] T. Mertens, J. Kautz, P. Bekaert, F. V. Reeth, and T. H.-P. Seidel. Efficient rendering of local subsurface scattering. In *Proceedings of the 11th Pacific Conference on Computer Graphics and Applications 2003*, 2003.

[42] J. Meseth, G. Müller, and R. Klein. Reflectance field based real-time, high-quality rendering of bidirectional texture functions. *Computers and Graphics*, 28(1):103–112, February 2004.

[43] J. T. Moon and S. R. Marschner. Simulating multiple scattering in hair using a photon mapping approach. *ACM Trans. Graph.*, 25(3):1067–1074, 2006. SIGGRAPH 2006.

[44] C. M. Mount, D. B. Thiessen, and P. L. Marston. Scattering observations for tilted transparent fibers: evolution of airy caustics with cylinder tilt and the caustic merging transition. *Applied Optics*, 37(9):243–249, 1998.

[45] S. Nayar, G. Krishnan, M. D. Grossberg, and R. Raskar. Fast Separation of Direct and Global Components of a Scene using High Frequency Illumination. *ACM Trans. on Graphics (also Proc. of ACM SIGGRAPH)*, Jul 2006.

[46] I. Neulander and M. van de Panne. Rendering generalized cylinders with paintstrokes. In *Graphics Interface*, pages 233–242, 1998.

[47] F. E. Nicodemus, J. C. Richmond, J. J. Hsia, I. W. Ginsberg, and T. Limperis. *Geometric considerations and nomenclature for reflectance*, volume 161 of *Monograph*. National Bureau of Standards (US), 1977.

[48] S. Paris, H. Briceño, and F. Sillion. Capture of hair geometry from multiple images. *ACM Transactions on Graphics (Proceedings of the SIGGRAPH conference)*, August 2004.

[49] M. Sattler, R. Sarlette, and R. Klein. Efficient and realistic visualization of cloth. In *EGRW '03: Proceedings of the 14th Eurographics workshop on Rendering*, pages 167–177. Eurographics Association, 2003.

[50] H. Schirmacher, W. Heidrich, M. Rubick, D. Schiron, and H.-P. Seidel. Image-based BRDF reconstruction. In B. Girod, H. Niemann, and H.-P. Seidel, editors, *Proceedings of the 4th Conference on Vision, Modeling, and Visualization (VMV-99)*, pages 285–292, Erlangen, Germany, November 1999. Infix.

[51] R. Schregle. Bias compensation for photon maps. *Computer Graphics forum*, 22(4), 2003.

[52] R. Schuh and T. Wriedt. Light scattering from bent cylindrical fibers for fiber length and diameter characterization. *Particle & Particle Systems Characterization*, 20:243–249, 2003.

[53] B. W. Silverman. Density estimation for statistics and data analysis. Chapmann and Hall,NY, 1986.

[54] P.-P. Sloan, J. Hall, J. Hart, and J. Snyder. Clustered principal components for precomputed radiance transfer. In *SIGGRAPH '03: ACM SIGGRAPH 2003 Papers*, pages 382–391, New York, NY, USA, 2003. ACM Press.

[55] G. Sobottka, M. Kusak, and A. Weber. Hairstyle construction from raw surface data. In *International Conference on Computer Graphics, Imaging and Visualisation (CGIV'06)*, pages 365–371, Sydney, Australia, 2006. IEEE Computer Society.

[56] G. Sobottka and A. Weber. Geometrische und physikalische Eigenschaften von Human-Haar. Computer Graphics Technical Report CG-2003-1, Institut für Informatik II, Universität Bonn, 53117 Bonn, Germany, 2003.

[57] R. F. Stamm, M. Garcia, and J. J. Fuchs. The optical properties of human hair i.fundamental considerations and goniophotometer curves. In *J.Soc.Cosm.Chem. 28*, pages 571–600, 1977.

[58] F. Suykens. On robust monte carlo algorithms for multi-pass global illumination. Master's thesis, Universiteit Leuven, September 2002.

[59] R. F. Tobler and S. Maierhofer. Improved illumination estimation for photon maps in architectural scenes. *Journal of WSCG*, 2006.

[60] H. C. van de Hulst. *Multiple light scattering*. Academic Press, 1980.

[61] V. L. Volevich, E. A. Kopylov, A. B. Khodulev, and O. A. Karpenko. An approach to cloth synthesis and visualization. In *The 7-th International Conference on Computer Graphics and Visualization*, 1997.

[62] K. Ward, F. Bertails, T.-Y. Kim, S. R. Marschner, M.-P. Cani, and M. Lin. A survey on hair modeling: Styling, simulation, and rendering. *IEEE Transactions on Visualization and Computer Graphics*, 13(2):213–234, 2007.

[63] K. Ward, N. Galoppo, and M. C. Lin. Modeling hair influenced by water and styling products. In *Proceedings of the Computer Animation and Social Agents 2004*, 2004.

[64] K. Ward, N. Galoppo, and M. C. Lin. Modeling hair influenced by water and styling products. In *ACM SIGGRAPH Sketches and Applications 2004*, 2004.

[65] Y. Wei, E. Ofek, L. Quan, and H.-Y. Shum. Modeling hair from multiple views. In *SIGGRAPH '05: ACM SIGGRAPH 2005 Papers*, pages 816–820, New York, NY, USA, 2005. ACM Press.

[66] S. Xu, F. Lau, H. Jiang, and Y. Pan. A novel method for fast and high-quality rendering of hair. In *Proceedings of the 17th Eurographics Symposium on Rendering (EGSR '06)*, 2006.

[67] Y.-Q. Xu, Y. Chen, S. Lin, H. Zhong, E. Wu, B. Guo, and H.-Y. Shum. Photorealistic rendering of knitwear using the lumislice. In *SIGGRAPH '01: Proceedings of the 28th annual conference on Computer graphics and interactive techniques*, pages 391–398, New York, NY, USA, 2001. ACM Press/Addison-Wesley Publishing Co.

[68] C. Yuksel. Hair occlusion: Rendering hair-like objects with global illumination. Technical report, College of Architecture Texas, A&M University, 2006.

LIST OF FIGURES